From the holdings of the Department of Special Collections , Princeton University Library, Princeton, NJ

These documents are either in the public domain, or can only be used for educational and research purposes (Fair use) as per U.S. Copyright law (text below). By accessing this file, all users agree that their use falls in the public domain or within fair use as defined by the copyrightlaw. We do not charge any permission or usage fees for the publication of images of material inour collections, including those provided by Princeton University Library, via our website, catalog, or directly from staff.For more information regarding copyright, credit, and citation please review the information onthe Copyright, Credit and Citation Guidelines page of our website.
https://library.princeton.edu/special-collections/policies/copyright-credit-and-citation-guidelines. If you have any questions, including how to order higher-quality images from the collection, contact Special Collections Public Services via our Ask Us! Form. https://library.princeton.edu/special-collections/ask-us

---

Doctoral Dissertations, 2011-2026 Neuroscience

2017

Whole-brain dynamics underlying spontaneous behavior in C. elegans

Linder, Ashley

Princeton, NJ : Princeton University

---

http://arks.princeton.edu/ark:/88435/dsp01zc77ss77z

U.S. Copyright law: The copyright law of the United States (Title 17, §108, United States Code) governs the making of photocopies or other reproductions of copyrighted material. Under certain conditions specified in the law, libraries and archives are authorized to furnish a photocopy or other reproduction. One of these specified conditions is that the photocopy or reproduction is not to be used for any purpose other than private study, scholarship, or research. If a user makes a request for, or later uses, a photocopy or reproduction for purposes in excess of fair use that user may be liable for copyright infringement. This institution reserves the right to refuse to accept a copying order if, in its judgment, fulfillment of the order would involve a violation of copyright law. https://www.copyright.gov/title17/title17.pdf

WHOLE-BRAIN DYNAMICS UNDERLYING SPONTANEOUS BEHAVIOR IN *C. ELEGANS*

Ashley Nicole Linder

A DISSERTATION PRESENTED TO THE
FACULTY OF PRINCETON
UNIVERSITY IN CANDIDACY FOR THE
DEGREE OF DOCTOR OF PHILOSOPHY

RECOMMENDED FOR ACCEPTANCE
BY THE PRINCETON NEUROSCIENCE
INSTITUTE

Advisors: Andrew Leifer and Joshua Shaevitz
November 2017

© Copyright by Ashley Linder, 2017. All rights reserved.

Abstract

Understanding how the brain drives behavior requires knowing the activity of every neuron in the circuit and the behavior that is produces from it. While obtaining such data in higher level organisms is currently unfeasible, the nematode Caenorhabditis elegans provides an attractive platform for studying the neural basis of behavior. With only 302 neurons and an optically transparent body, C. elegans is particularly amenable for observing an entire neural circuit. We have developed an imaging system that allows us to record calcium activity from every neuron in the worm's brain while it is freely behaving. Additionally, we have developed a time-independent algorithm for automatically segmenting and tracking each neuron across a recording.

Using the methods we have developed for whole-brain imaging in freely behaving C. elegans, we sought to determine the size, separation, and dynamics of the circuits driving locomotion and turning. To do so, we used machine learning techniques to predict these behaviors from the neural activity, identifying the neurons involved in each of these behaviors. We find that neither behavior requires integration over previous neural activity, suggesting that they are both driven by the current magnitude of activity of their circuit components. Additionally, we find that the circuits for locomotion and turning are largely distinct, although the locomotion circuit does contain some information about turning. These results suggest that these two behaviors are driven by the magnitude of neural activity of separate circuits.

Acknowledgements

First of all, I'd like to thank my advisers, Josh Shaevitz and Andy Leifer. Without Andy, this entire project would have never gotten off the ground. I want to thank Josh for being a filthy liar, and not actually being a hands off name on the paper.

In addition to being great advisers, Andy and Josh also hired wonderful, supportive people for their labs. Thanks to Jeff and Ugne for sharing an office with me and constantly providing helpful and insightful comments. Shout out to Ben Bratton and Gordon Berman for knowing everything about everything and always being willing to help. Special thanks to Mochi for raft adventures and science support and being awesome.

I was blessed with having an amazing cohort to start the whole graduate school process with. I don't think I finished a single homework assignment without some help from Adrianna. Nathan was my rock throughout the first year, from homework struggles to social interactions. And Leenoy has been there for all the venting and celebrating, from not being able to record from a stupid crayfish to actually getting publishable results.

On the non-academic side of things, I want to thank all the great people I've met and befriended here over the years. In particular, the people who have put up with living with me, Laura, Berliner, Gerry, Chow, Nick, Dave, Abhi, Wes, and Becca – thanks for generating nice spaces to come home to when science was totally sucking. Thanks to all the other friends who made things here not as awful – Felicity, Rose, Genna, Garebear, Akil, other Dave, and Sagar. Also, thanks to the Ivy, Rick, Angelina, Mills, Kyle, Brad, and Vicki for helping make a Dbar family. And Aric gets a special mention for being a wonderful, supportive boyfriend who put up with an amazing amount of hogwash but still stayed with me.

Obviously none of this would have been possible without the people who provided the genetic material to make me – so thanks to my parents for doing that, and also for the unwavering support and love, even when they had no idea what I was doing. I also want to thank my grandma, because there's nothing like a 92 year old woman with a broken hip saying she wants to see her youngest grandchild get a PhD before she dies to motivate you to finish this shit.

Most importantly, I want to thank the one being that I hope will one day read this – my dog, Mimosa, who was very frequently the only reason I got of bed, and is my primary motivation to become a functional human being so I can give her the life she deserves.

Contents

Abstract.....i
Acknowledgements.....ii
List of Tables.....vi
List of Figures.....vii

1 Introduction

1.1 Neural dynamics underlying behavior.....1
1.2 *C. elegans* as a model system.....3
1.3 *C. elegans* toolkit.....4
1.4 *C elegans* motor circuits.....5
1.5 Thesis outline.....7

2 Whole-brain calcium imaging with cellular resolution in freely behaving Caenorhabditis elegans.....8

2.1 Abstract.....8
2.2 Introduction.....9
2.3 Results.....11
2.3.1 Volumetric imaging in a freely moving worm.....11
2.3.2 Whole-brain neural dynamics with cellular resolution during locomotion.....15
2.3.3 Observed GCaMP fluorescence cannot be explained by motion alone.....19
2.3.4 Specific neurons correlate with each of the three observed behaviors.....23
2.3.5 Comparison of neural positions.....25
2.4 Discussion.....27
2.5 Materials and Methods.....30
2.5.1 Strains.....30
2.6 Appendix.....32
2.6.1 Microscopy.....32
2.6.2 Image acquisition.....33
2.6.3 Volumetric imaging and 3D tracking.....34
2.6.4 Free behaving whole-brain imaging experiments.....35

2.6.5 Immobilized calcium imaging experiments....36
2.6.6 Extracting neural signals....36
2.6.7 Comparing motion artifact in nuclear vs cytoplasmic expressing worms....39
2.6.8 Calculating portion of apparent neural activity that can be attributed to signal and noise....40
2.6.9 Analyzing behavior....41
2.6.10 Criteria for correlating behavior with neural signals....43
2.6.11 Behavioral control experiments....44
2.6.12 Neural identification testing....45
3 Automatically tracking neurons in a moving and deforming brain....64
3.1 Abstract....64
3.2 Introduction....65
3.3 Results....68
3.3.1 Overview of neuron tracking analysis....68
3.3.2 Recording of whole-brain calcium activity and body posture in moving animal....70
3.3.3 Centerline detection and gross brain alignment....71
3.3.4 Segmentation....74
3.3.5 Neuron registration vector construction....74
3.3.6 Clustering registration vectors....79
3.3.7 Correcting errors in tracking and segmentation....80
3.3.8 Comparison with manually annotated data....82
3.4 Discussion....85
3.5 Materials and Methods....87
3.5.1 Strains....87
3.5.2 Imaging *C. elegans*....87
3.5.3 Thin plate spline transformations....88
3.5.4 Clustering....89
3.5.5 Algorithm implementation....91
4 Whole brain dynamics underlying behavior....94
4.1 Introduction....94

4.2 Results.....96
4.2.1 Moving worms have more activity and dynamics than immobilized worms..96
4.2.2 Neural activity can predict forward and backward locomotion.....101
4.2.3 Predicting turns from neural activity.....107
4.2.4 Comparing locomotion and turning.....109
4.3 Discussion.....112
4.4 Materials and Methods.....114
4.4.1 Strains.....114
4.4.2 Calcium imaging in immobilized worms.....114
4.4.3 Calcium imaging in freely moving worms.....115
4.4.4 Extraction and processing of neural signals.....115
4.4.5 Principal components analysis of immobilized and freely moving worms...116
4.4.6 Measures of activity in immobilized and freely moving worms.....116
4.4.7 Quantitatively describing locomotion as a continuous variable.....117
4.4.8 Predicting continuous behavior with lasso.....117
4.4.9 Predicting turns using support vector machines.....118
4.4.10 Comparing weights.....119
5 Conclusion.....120
5.1 Adding whole-brain imaging with cellular resolution to the *C. elegans* toolkit.....120
5.2 Neural dynamics underlying behavior in *C. elegans*.....121
6 Bibliography.....123

List of Tables

2.1 Summary of behavioral control experiments.....47
2.2 Average worm speed observed in this study compared to the literature.....48
2.3 Number of neurons observed in Strain AML14 when imaged under varying condition.....50
2.4 Summary of statistical analysis comparing signals from ratiometric to non-ratiometric imaging approaches.....57
2.5 Summary of evidence in literature implicating neurons in forward, reverse, and turning behavior.....57
2.6 Properties and parameters of the three cameras used.....62
2.7 Orientation of the worms that were imaged.....62
3.1 Breakdown of computation time and scalings for Neuron Registration Vector Encoding Pipeline.....91

List of Figures

2.1 Simultaneous imaging of whole-brain calcium activity and behavior, simplified schematic.....12

2.2 Simultaneous recording of four video streams showing behavior and neural activity.....14

2.3 Worm behavior recorded during imaging.....16

2.4 Recordings from two of four individuals shown containing neural activity from 56 and 77 neurons, respectively.....18

2.5 Correlations between calcium activity of neurons from two worms.....19

2.6 Transients observed from 63 neurons in freely moving GFP control worm.....20

2.7 Comparison between GCaMP6s individuals and GFP control worm.....21

2.8 All neurons whose activity correlated with either forward, turning, or reverse behavior above a significance threshold for worm 1.....24

2.9 Position of recorded neurons from worm 1 plotted in 3D and compared with an atlas.....25

2.10 Behavioral control experiments comparing GCaMP strain to wild type and comparing animal behavior on an open-air agar plate and during whole brain imaging.....46

2.11 Number of neurons observed for immobilized worms under varying exposure times.....49

2.12 Neural activity from four individual worms recorded during behavior.....51

2.13 Example traces recorded during behavior.....52

2.14 Calcium dynamics recorded at 200 Hz.....53

2.15 Correlations between calcium activity of neurons from all four individual worms.....54
2.16 Motion artifacts in control worms for different imaging approaches.....55
2.17 Statistical analysis reveals the portion of GCaMP recordings that is unlikely to be attributed to motion or noise, for ratiometric and non-ratiometric approaches.....56
2.18 All neurons whose activity correlated with either forward, turning, or reverse behavior above a significance threshold for all individuals.....58
2.19 Positions of recorded neurons for each worm plotted in 3D and compared to an atlas.....59
2.20 Neurons cannot easily be identified across worms based on position information alone.....60
2.21 Schematic of the optical elements used.....61
2.22 Distribution across neurons of the accuracy of the tracker as compared to human.....63
3.1 Schematic of analysis pipeline to segment and track neurons through time and extract their neural activity in a deforming brain.....69
3.2 Input to pipeline.....70
3.3 Centerline is used for straightening to segment neurons.....72
3.4 Schematic of Neuron Registration Vector Encoding.....77
3.5 Example of consensus voting to correct a misidentified neuron.....82
3.6 Comparison of the automated Neuron Registration Vector Encoding algorithm with manual human annotation.....84
3.7 Calcium activity traces extracted using Neuron Registration Vector Encoding.....85

4.1 Brain-wide activity of an immobilized worm.....98

4.2 Brain-wide activity of a freely behaving worm.....99

4.3 Activity in freely moving vs. immobilized worms.....100

4.4 Postural dynamics of the worm.....101

4.5 Distinguishing forward and backward locomotion in posture space.....102

4.6 Mean squared error of $d\theta/dt$ from varying parameter values in the validation set....105

4.7 Predicting forward and backward locomotion from neural activity.....106

4.8 F_1 score of binary classification of turns from varying parameters.....108

4.9 Predicting turns from neural activity.....109

4.10 Comparing eights of turning and locomotion.....110

4.11 Predicting behaviors with different neuron subsets.....111

Chapter 1

Introduction

1. 1 Neural dynamics underlying behavior

One of the fundamental questions in neuroscience is how the coordinated activity of a collection of neurons produces some output, such as movement and complex motor sequences. A first step in addressing this question is developing a quantitative description of the relationship between an organism's neural activity and the behavior it produces. To this end, many technologies and assays have been developed to record neural activity while an organism is behaving.

Paired recordings of neural activity and behavior have already provided tremendous insight into the computations the brain uses to drive behavior. Calcium imaging of the PPC in head fixed rodents performing a decision task in virtual reality has shown that the trajectory of neural circuit activity can predict the choice that the rodent makes in correct trials[1]. In zebrafish, the network dynamics recorded using whole brain imaging while the animal fictively interacted with a virtual environment were decomposed into four types of neuronal response properties[2]. These studies illustrate two reoccurring themes in systems neuroscience: 1)

behavior is encoded in the neural dynamics and 2) the meaningful information about behavior in these dynamics can be represented in a low dimensional space.

Neural dynamics encompass both the magnitude and timing of a neurons activity. In the visual system, the precise timing of neurons to stimuli is necessary to represent the slower time scales of visual world[3]. Accumulation of evidence tasks have shown that individual neuron responses are temporally heterogeneous, with the decision variable encoded in the linear combination of these responses, indicating that the behavioral decision arises from the integration of the neural activity over time[4]. In the leach, behavioral decisions can predicted from the activity of the neural population occurring 300 msec before the actual behavior[5]. These studies indicate that the timing of neural activity is important, and that the computations that drive behavior may be occurring at multiple time scales.

A common restraint in investigating how neural activity drives behavior, present in these studies, is that technical limitations require that the behavior must be over short time intervals, or focus on a specific trained behavior repeated over many trials. As a result, it is unclear if these dynamics exclusively drive these behaviors, or if they are also present in behaviors occurring in a different context. It has been shown that some neural networks mediate multiple behaviors[6], suggesting that understanding how the individual motor components that comprise a behavioral sequence are enacted is important for understanding how neural activity drives behavior.

These studies demonstrate a compromise that experimenters must make between recording richer, complex behavior or recording from a larger percentage of the nervous system. Head fixed rodents can perform intricate and complex behavioral tasks, but the size of their nervous system necessitates that only a small portion can be recorded from at a given time. Whole-brain imaging is possible in the zebrafish, but the animal is paralyzed, greatly limiting the

behavioral repertoire. To understand how neural circuits are generating and coordinating behaviors, and the time scales at which they do so, it is necessary to record from the entire brain of the animal while it is engages in multiple action sequences. While this is currently unfeasible in most model organisms, the nematode C. elegans provides a platform in which this can be achieved.

1.2 *C. elegans* as a model system

The simplicity and accessibility of the *C. elegans* nervous system make it an ideal candidate for observing a complete neural circuit. Early work on *C. elegans* produced the complete connectome of the worm, detailing the roughly 7500 synapses occurring between the 302 neurons, which are stereotyped across worms[7]. Of these 302 neurons, ~125 are located in and around the ventral nerve ring in the animal's head, forming the worm's 'brain' and controlling the processing of sensory information coming from the anterior portion of the worm. Due to their optically transparent body and tractable genetics, enabling the expression of genetically encoded calcium indicators, it is possible to image this entire population of neurons in the anesthetized worm[8]. Because *C. elegans* lack the voltage gated sodium channels that drive the canonical action potential, the nervous system uses slow, graded potential for signaling[9]. This allows for a slower acquisition rate when recording the neural activity.

In addition to having a compact, accessible nervous system, *C. elegans* also exhibit complex behavior that can be objectively quantified. Despite having a simple nervous system, *C. elegans* exhibits chemotaxis[10], non-associative learning[11], associative learning of food and environmental stimuli (odor, temperature, etc.)[12], and stereotyped motor sequences such as the escape response. Previous work has shown that the body shape of the worm can be

described as a combination of four principle postures, such that behavior can be described as a trajectory in four-dimensional space[13].

1.3 *C. elegans* toolkit

The unique advantages of *C. elegans* as a model system have led to a wide variety of tools developed to interrogate their nervous system. The highly stereotyped genetics and anatomy across worms has allowed researchers to remove individual neurons from the circuit, either through laser ablations[14] or genetic mutations[15]. While these studies have been valuable in identifying the key components in the circuits underlying various behaviors, there are crucial features of neural activity that these experiments cannot capture. Laser ablation studies show the necessity of specific neurons, but fail to capture temporal information of when a neuron is necessary. Additionally, because these studies have focused on individual classes of neurons, there is no information on how the different neurons interact to generate behavior, whether the respective timing or degree of activity is important, or if and how the system is robust to such variation. Such questions can only be addressed with the development of tools allowing for the simultaneous recording and manipulation of neural activity while the animal is behaving.

While their small size makes electrophysiological recordings of neural activity difficult, the optically transparent body of *C. elegans* allows for both optogenetic recordings and manipulations in an intact animal. *C. elegans* was the first organism in which light activated proteins were used to manipulate the animal's behavior[16]. These early experiments have been greatly expanded upon, using computer vision and real time feedback to track a moving animal to deliver spatially and temporally precise stimulation or inhibition to targeted neurons[17]. This

has also been combined with calcium imaging, so that it is possible to record the activity in one neuron while manipulating the activity in another, while the worm is moving[18].

In addition to targeting individual neurons in the *C. elegans* nervous system, tools and techniques have been developed for large scale recordings. Microfluidic devices have been developed to immobilize a worm while still allowing for the delivery of chemical or odor stimuli[19]. This has been used in conjunction with widefield temporal focusing microscopy and lightfield microscopy to record from the ~100 neurons in the head ganglia of immobilized worms[8]. While these preparations have provided insight into the basal network activity and responses to sensory stimuli, they do not allow for concurrent measurements of neural activity and the behavior it produces.

1.3 *C. elegans* motor circuits

Because of the connectome and the myriad of tools developed to probe and record neural activity in *C. elegans,* many of the neurons have known behavioral functions. Mechanosensory neurons in the anterior (AVM, ALM) and posterior (PVM, PLM) synapse onto interneurons AVA and AVB respectively[7], [20]. AVA innervates the VA DA motorneurons, which control backward movement, while AVB innervates the motorneurons controlling forward movement. While laser ablations of AVA or AVB cause deficits in backward and forward locomotion respectively, worms can still initiated reversals when AVA has been ablated[7], [20]. This, in conjunction with genetic studies[21], [22], suggests that there are other neurons involved in generating and maintaining worm locomotion.

In addition to forward and backward locomotion, the *C. elegans* behavioral repertoire also includes turns. Turns are tightly coupled with reversals, although occasionally occur in

isolation[23]. Animals lacking AVA have normal turns, suggesting that this reversal circuit is distinct from the turning circuit. Ablation studies have identified neurons that are involved in various aspects of turning; SMD regulates turn amplitude, while RIV regulates the turn direction[23]. These ablations had no effect on reversals, further suggesting a separation of these two circuits.

While knowing the key components of the circuit is essential for understanding how it drives behavior, it is still missing crucial features. Laser ablations studies show necessity of specific neurons, but fail to capture temporal information of *when* a neuron's activity is necessary. Additionally, other neurons may be involved in these behaviors, but may have been overlooked. And while the locomotion and turning circuits appear to be largely distinct, it is unclear if there is some overlap or information shared between them necessary for choosing which behavior to enact.

Calcium imaging and optogenetic manipulations have provided some insight into the questions that ablations fail to address. AVA shows increased calcium activity when the worm reverses, and optogenetic stimulation causes an increase in reversal behavior, confirming its role in backward locomotion[24], [25]. Additionally, the interneurons RIM and AIB exhibit similar responses, suggesting the activity driving backward locomotion is dispersed throughout the network[24], [25]. Whole brain calcium imaging in restrained worms shows that many neurons participate in coordinated dynamic activity, suggesting that the population state may be encoding behavior[24]. However, as the worm is not actually behaving, it remains unclear if these states are actually driving behavior, or at what time scale they might be doing so.

1.4 Thesis Outline

The beginning of this work details advances made in expanding the *C. elegans* toolkit. Chapter 2 describes a system that allows us to measure the calcium dynamics of every neuron in the worm's brain while it is freely moving. Chapter 3 presents a fully automated method for segmenting and tracking the neurons in freely moving *C. elegans*. In Chapter 4, I use these methods to interrogate how the circuits distributed across the worm brain are generating behavior in freely moving worms, and the time scales at which they do so.

Chapter 2

Whole-brain calcium imaging with cellular resolution in freely behaving *Caenorhabditis elegans*

This work was originally published as ref [70].

Jeffrey P. Nguyen, Frederick B. Shipley, Ashley N. Linder, George S. Plummer, Mochi Liu, Sagar U. Setru, Joshua W. Shaevitz, and Andrew M. Leifer. Whole-brain calcium imaging with cellular resolution in freely behaving *Caenorhabditis elegans* PNAS 2016 113 (8) E1074-E1081

2.1 Abstract

The ability to acquire large-scale recordings of neuronal activity in awake and unrestrained animals is needed to provide new insights into how populations of neurons generate animal behavior. We present an instrument capable of recording intracellular calcium transients from the majority of neurons in the head of a freely behaving *Caenorhabditis elegans* with cellular resolution while simultaneously recording the animal's position, posture, and locomotion. This instrument provides whole-brain imaging with cellular resolution in an unrestrained and behaving animal. We use spinning-disk confocal microscopy to capture 3D

volumetric fluorescent images of neurons expressing the calcium indicator GCaMP6s at 6 head-volumes/s. A suite of three cameras monitor neuronal fluorescence and the animal's position and orientation. Custom software tracks the 3D position of the animal's head in real time and two feedback loops adjust a motorized stage and objective to keep the animal's head within the field of view as the animal roams freely. We observe calcium transients from up to 77 neurons for over 4 min and correlate this activity with the animal's behavior. We characterize noise in the system due to animal motion and show that, across worms, multiple neurons show significant correlations with modes of behavior corresponding to forward, backward, and turning locomotion.

2.2 Introduction

How do patterns of neural activity generate an animal's behavior? To answer this question, it is important to develop new methods for recording from large populations of neurons in animals as they move and behave freely. The collective activity of many individual neurons appears to be critical for generating behaviors including arm reach in primates[26], song production in zebrafinch[27], the choice between swimming or crawling in leech [5], and decision-making in mice during navigation[1]. New methods for recording from larger populations of neurons in unrestrained animals are needed to better understand neural coding of these behaviors and neural control of behavior more generally.

Calcium imaging has emerged as a promising technique for recording dynamics from populations of neurons. Calcium-sensitive proteins are used to visualize changes in intracellular calcium levels in neurons in vivo which serve as a proxy for neural activity[28] . To resolve the often weak fluorescent signal of an individual neuron in a dense forest of other labeled cells

requires a high magnification objective with a large numerical aperture that, consequently, can image only a small field of view. Calcium imaging has traditionally been performed on animals that are stationary from anesthetization or immobilization to avoid imaging artifacts induced by animal motion. As a result, calcium imaging studies have historically focused on small brain regions in immobile animals that exhibit little or no behavior[29].

No previous neurophysiological study has attained whole-brain imaging with cellular resolution in a freely behaving unrestrained animal. Previous whole-brain cellular resolution calcium imaging studies of populations of neurons that involve behavior investigate either fictive locomotion[2], [5], or behaviors that can be performed in restrained animals, such as eye movements[30] or navigation of a virtual environment[31]. One exception has been the development of fluorescence endoscopy, which allows recording from rodents during unrestrained behavior, although imaging is restricted to even smaller subbrain regions[32].

Investigating neural activity in small transparent organisms allows one to move beyond studying subbrain regions to record dynamics from entire brains with cellular resolution. Whole-brain imaging was performed first in larval zebrafish using two-photon microscopy[2]. More recently, whole-brain imaging was performed in *Caenorhabditis elegans* using two-photon[8] and light-field microscopy[33]. Animals in these studies were immobilized, anesthetized, or both and thus exhibited no gross behavior.

C. elegans' compact nervous system of only 302 neurons and small size of only 1 mm make it ideally suited for the development of new whole-brain imaging techniques for studying behavior. There is a long and rich history of studying and quantifying the behavior of freely moving *C. elegans* dating back to the mid-1970s[34]. Many of these works involved quantifying animal body posture as the worm moved, for example as in ref. 15. To facilitate higher-

throughput recordings of behavior, a number of tracking microscopes[35]–[37] o[36]r multiworm imagers were developed[38], [39] along with sophisticated behavioral analysis software and analytic[37]al tools[13], [40]. Motivated in part to understand these behaviors, calcium imaging systems were also developed that could probe neural activity in at first partially immobilized[41] and then freely moving animals, beginning with ref. 24 and then developing rapidly[18], [25], [36], [37], [42]–[44]. One limitation of these freely moving calcium imaging systems is that they are limited to imaging only a very small subset of[39] neurons and lack the ability to distinguish neurons that lie atop one another in the axial direction of the microscope. Despite this limitation, these studies, combined with laser-ablation experiments, have identified a number of neurons that correlate or affect changes in particular behaviors including the AVB neuron pair and VB-type motor neurons for forward locomotion; the AVA, AIB, and AVE neuron pairs and VA-type motor neurons for backward locomotion; and the RIV, RIB, and SMD neurons and the DD-type motor neurons for turning behaviors[18], [23], [36], [37], [42], [43], [45] . To move beyond these largely single-cell studies, we sought to record simultaneously from the entire brain of *C. elegans* with cellular resolution and record its behavior as it moved about unrestrained.

2.2 Results

2.2.1 Volumetric Imaging in a Freely Moving Worm

We generated transgenic animals that express both a genetically encoded calcium indicator, GCaMP6s, and a calcium-insensitive fluorescent protein RFP, in the nucleus of each neuron (strain AML14; *Materials and Methods*). The transgenic worms exhibited normal

behavior compared with WT as measured by the animal's velocity, turn rate, pause rate, and run length (*SI Appendix*, Fig. S1 and Table S1).

To record fluorescent images of all neurons in the worm's head while simultaneously recording the animal's behavior, we developed a custom dual-objective 3D tracking system. A spinning disk confocal microscope records images of the head of a worm through a 40x objective using both 488- and 561-nm excitation laser light while a second imaging path records the worm's position and behavior through a 10x objective (Fig. 1). In contrast to previous dual-objective worm trackers[37], this system operates in three dimensions. Custom real-time software uses fluorescence imaging to identify the location of the worm's brain in three dimensions and adjusts a motorized stage and piezoelectric objective mount to follow the brain as it moves and to scan through its brain volume as it crawls.

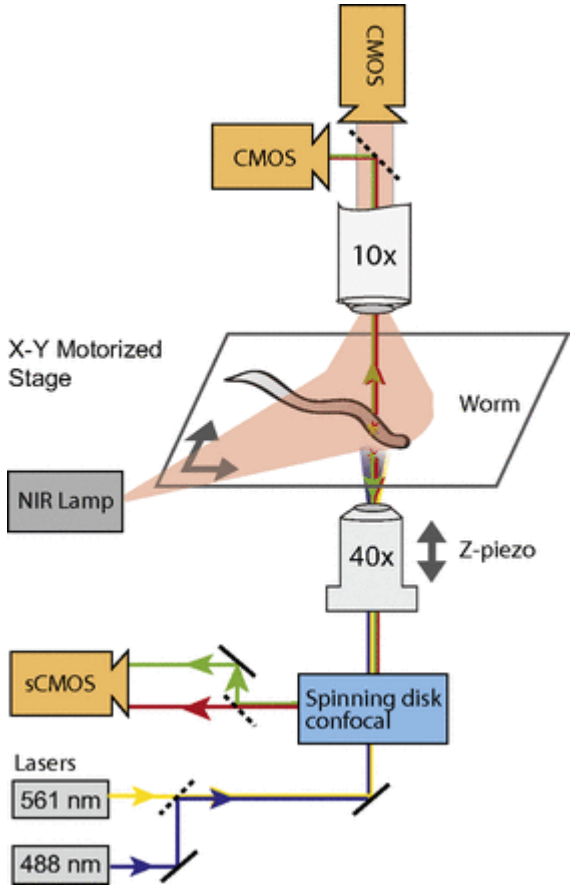


Figure 2.1: Simultaneous imaging of whole-brain calcium activity and behavior, simplified schematic. A worm crawls freely on a motorized stage under near-infrared (NIR) dark-field illumination. A spinning disk confocal microscope acquires volumetric fluorescent images of the worm's brain by scanning a 40× objective along the imaging axis (z) to acquire 6 brain volumes/s. A low-magnification 10× objective images the animal's posture and behavior. Custom 3D real-time tracking software feeds back on the fluorescence images and adjusts the xy motorized stage and z-piezo stage accordingly to keep the worm's head centered in the high magnification objective's field of view

To acquire 3D image stacks of the worm's head, a piezoelectric stage translates the 40× objective up and down along the imaging axis such that the focal plane passes through the animal's head six times per second. The confocal spinning disk rejects out-of plane light and provides optical sectioning. A high-speed, high-sensitivity Scientific CMOS (sCMOS) camera records fluorescent images at 200 fps, thereby capturing 6 head volumes/s, each consisting of ~33 *z*-slices, 1.5–1.6 μm apart, depending on the size of the individual animal's head. Each *z*-stack spans a volume that is sized to the head of the individual worm but is usually 150×150μm in length and width and 48–51 μm in depth. This field is sufficiently large to image all neuronal cell bodies in the head of the animal, including those located from the tip of the nose, through the nerve ring, to the ventral nerve cord immediately posterior of the pharyngeal terminal bulb. To capture both the calcium dynamics and information about the location of cell bodies, red- and green-channel fluorescent images are recorded side-by-side on the sCMOS sensor simultaneously (Fig. 2 *C–F*).

An animal's head moves dramatically during crawling, which poses challenges for volumetric imaging. Worms crawl with a center of mass velocity of up to 0.25 mm/s and in 1 s the head can swing side-to-side by as much as 70 μm, corresponding to nearly two head diameters. To keep the worm's head centered in the field of view of the high magnification objective, we used a second, low-magnification microscope located on top of the worm to track its movements in real time and to adjust a motorized stage to compensate for the animal's motion. A high-speed CMOS camera records large depth-of-field fluorescence images of the neurons in the worm's head through a 10× objective at 67 fps (Fig. 2*B*). Custom software based on the MindControl codebase[17], written in C, finds the *x-y* position of the animal's head from the low-magnification fluorescent images and adjusts the velocity of the motorized stage so as to

keep the head of the worm centered. This *x-y*feedback loop updates at 67 Hz and keeps the worm within the field of view for the duration of our recordings, even when the worm touches itself or crosses over itself. During recordings, the tracker regularly accommodated worm velocities in excess of 0.15 mm/s and turn rates of more than 3 turns/min without losing the animal (*SI Appendix*, Fig. S1 and Table S1).

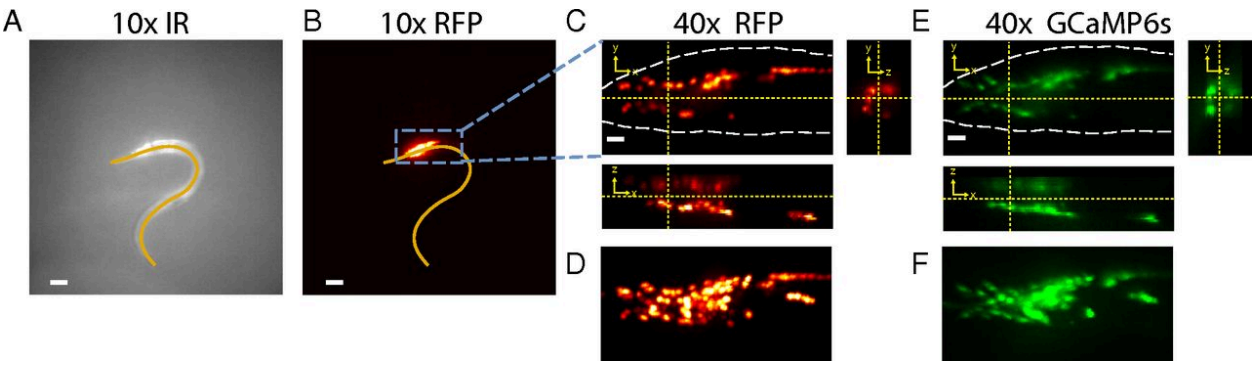


Figure 2.2: Simultaneous recording of four video streams showing behavior and neural activity. (A) The worm's posture and behavior are recorded via infrared (IR) darkfield imaging through the 10× objective at 42 fps. (B) Fluorescence from neurons in the worm's head is tracked in real time to keep the worm centered in the field of view, via the 10× objective at 67 fps. (Scale bar, 100 μm.) Orange line indicates the worm's centerline. (C–F) Fluorescence images of neuronal nuclei are simultaneously recorded through the 40× objective at 200 fps as the objective scans through the worm's head along the axial imaging axis, z. A 3D volume is reconstructed from a z-stack of acquired images. (Scale bars, 10 μm.) (C and E) Individual xy, xz, and zy slices are shown for (C) RFP and (E) GCaMP6s. White dashed line indicates approximate outline of the worm's head. (D and F) Maximum intensity projection of the same volume is shown for (D) RFP and (F) GCaMP6s

The worm also moves its head along the imaging axis (*z*) as it crawls. This movement occurs when the worm raises its head off of the agarose pad or when the worm crawls over agarose of varying thickness. To keep the worm's head in the center of the *z*-scanning range, we

analyze fluorescent images from the high magnification objective in real time to find the center of the worm's head in each *z*-stack. We then adjust the piezo scan range to compensate for any head motion. This *z* feedback loop is part of the same LabView code that records high magnification fluorescence. The *z* feedback updates at 3 Hz and keeps the worm within the scan range. The feedback loop compensated for changes in the worm's head position of as large as 8 μm in *z*, or 20% of its head diameter, in the course of 333 ms.

To study neural coding of behavior, it is critically important to record the animal's full body posture. A third camera in our system records the worm's posture and behavior at 42 fps through the 10× objective using near-infrared (NIR) dark-field illumination. Images from this camera are analyzed off-line to define the body shape over time. Images from the four simultaneously recorded video feeds are visible in Fig. 2 and Movies S1 and S2.

2.2.2 Whole-Brain Neural Dynamics with Cellular Resolution During Locomotion

As a proof of principle, we recorded the neural activity and behavior of four individual worms (strain AML14) crawling freely on agarose pads for up to 5 min. We quantified their behavior by calculating the worm's center-of-mass velocity and body centerline at each time point. The center-of-mass velocity was used to define the worm velocity relative to the body orientation such that positive velocity corresponds to forward locomotion and negative velocity to backward locomotion (Fig. 3). Body centerline information was used to automatically classify animal behavior via an eigenworm analysis (21) (*SI Appendix*, *Methods*) into four behavioral modes: forward crawling, backward crawling, pausing, and turning. Note that on average worms exhibited slightly slower locomotion and had higher turning rates when in the imaging arena than on an open agar plate (*SI Appendix*, Fig. S1 and Tables S1 and S2).

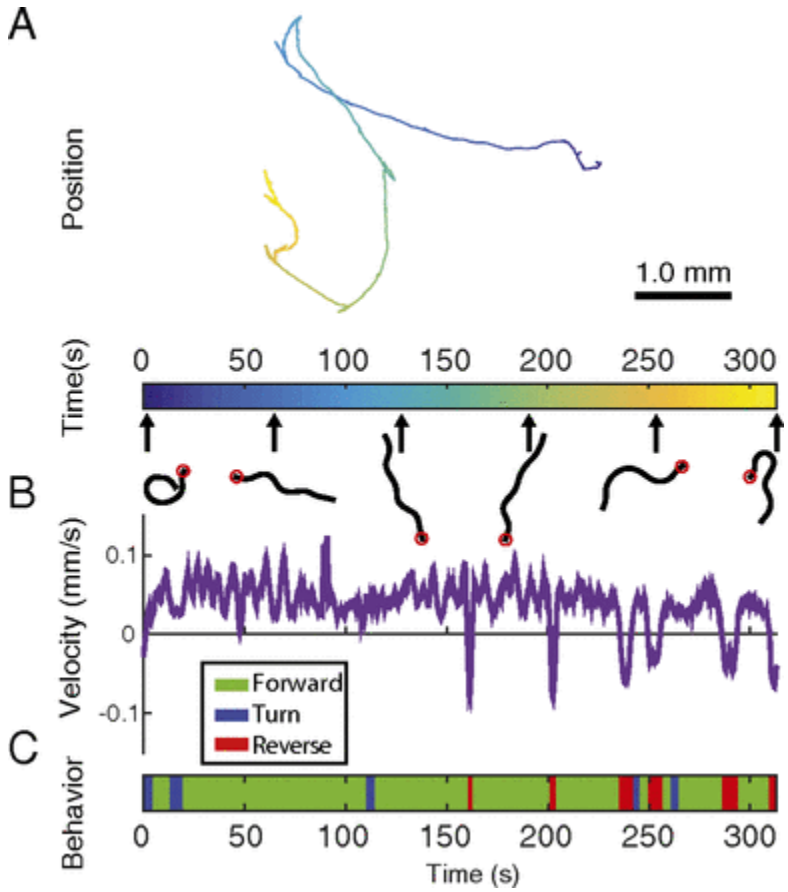


Figure 2.3: The worm's behavior is recorded during imaging. Data from worm 1 is shown. The worm's (A) center-of-mass trajectory, body shape, and (B) velocity in the anterior direction are shown. (C) An ethogram describing the behavior is generated automatically from the worm's posture and behavior (SI Appendix, Methods).

As the worm crawled we recorded the location of each neuron in the worm's head. Only fluorescence from the calcium insensitive RFP was used to identify the location of each cell. Nuclear regions were identified through a human-supervised semiautomated process. 77, 68, 57, and 56 neuronal nuclei were observed in the four moving worms, respectively, accounting for slightly less than half of the 181 neurons we would expect to be in our field of view based on electron microscopy data[7] (caltech.wormbase.org/virtualworm/). The number of neurons we observe in our moving worms is comparable to the 83±1583±15 (mean ± SD) neurons identified

in a recent whole-brain imaging study of immobilized and anesthetized worms[8]. A number of factors likely account for the discrepancy between the mean of 64.5 neurons per worm that we observe and the 181 neurons expected from electron microscopy. Constraints associated with imaging freely moving animals accounts for some of the discrepancy. When worms of the same strain are immobilized and imaged under more favorable conditions, such as longer exposure times, shorter recordings, and thus less photobleaching, up to 90 neurons are observed (*SI Appendix*, Fig. S2 and Table S3). Most of the discrepancy however, is likely due to the expression pattern of the pan-neuronal promotor and the mosaic inheritance of the extrachromsomal array through development.

To extract calcium dynamics, we measured the fluorescence intensity of GCaMP6s, which was coexpressed with RFP in the nuclei of each neuron. The GCaMP6s fluorescence was measured in a segmented volume defined by the fluorescence from the RFP channel. The segmented region was identified by searching within a sphere with radius 2 μm centered around the centroid of the neuron's nucleus. The ratio of the fluorescent intensities of GCaMP6s to RFP provided a robust signal of the relative intracellular calcium in the neuron.

This nuclear-localized ratiometric approach allowed us to record calcium dynamics even as the worm turned, reversed, touched itself, or reoriented (Fig. 4, *SI Appendix*, Fig. S3, and Movies S3 and S4). The most active neurons exhibited calcium transients with a $\Delta R/R_0$ of nearly 200% (*SI Appendix*, Fig. S4), where $R=F_g/F_r$ is the ratio of the intensity of the GCaMP6s fluorescence, F_g, to the intensity of the RFP fluorescence, F_r; and R_0 is the neuron-specific ratiometric fluorescence baseline (*SI Appendix, Methods*).

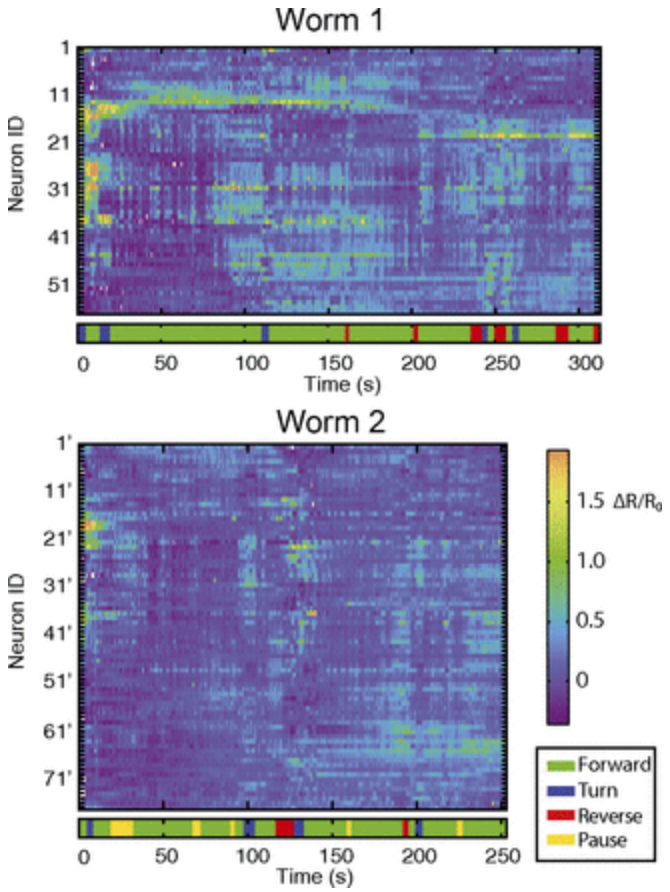


Figure 2.4: Recordings from two of four individuals are shown containing neural activity from 56 and 77 neurons, respectively. Additional recordings are shown in SI Appendix, Fig. S3. The ratio of GCaMP6s fluorescence to RFP fluorescence for each neuron is plotted. The ratio of fluorescent intensities, R, is represented as the fractional change in ΔR/R0, where the baseline R0 is defined for each neuron as the lower 20th percentile value. Neurons are sorted via a hierarchical clustering algorithm. Corresponding correlations are shown in Fig. 5. Behavioral ethograms are shown. Neural data from worm 1 corresponds to the same recording as in Fig. 3. Note, neural ID numbers do not indicate correspondence across worms. Occasional white gaps in the data represent instances when the neuron is obscured or transiently leaves the field of view (SI Appendix, Methods).

The fluorescence intensity of each neuron was sampled six times in a second (*SI Appendix, Methods*), similar to the 4–6 Hz used in previous whole-brain imaging experiments on immobilized and anesthetized worms[8]. This rate is sufficient to capture a vast majority of the calcium dynamics probed with GCaMP6s (*SI Appendix*, Fig. S5).

The correlations of calcium transients between neurons were also calculated. The resulting block structure is suggestive of functionally connected neural units (Fig. 5 and *SI Appendix*, Fig. S6). In the future, these functional units may serve as a starting point for investigating interactions between microcircuits and whole-brain dynamics.

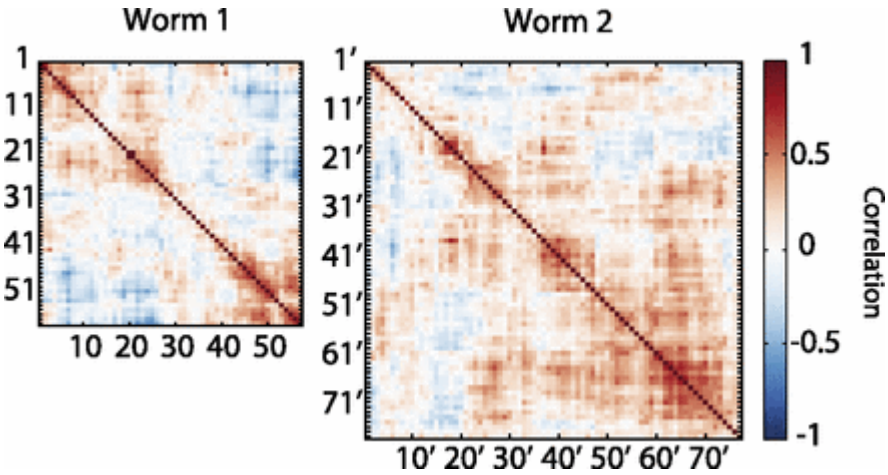


Figure 2.5: Correlations between calcium activity of neurons from two worms are shown. Data correspond to neural activity shown in Fig. 4. Correlation values are hierarchically clustered using a Euclidean distance metric so that neurons with similar activity are organized together. Additional worms are shown in SI Appendix, Fig. S6.

2.2.3 Observed GCaMP Fluorescence Cannot Be Explained by Motion Alone

Artifacts created by the animal's motion pose particular concern because they could be misinterpreted as calcium signals. For example, as the worm moves, individual neurons might compress or expand thereby changing the density of fluorescent protein, which could potentially create the appearance of a calcium transient. Additional artifacts could arise from motion blur, or from spatial inhomogeneities in illumination. We used a GFP control worm to directly measure changes in our apparent calcium signal due to motion and other artifacts. A transgenic worm was made to express calcium insensitive GFP in place of the calcium sensitive GCaMP (strain AML18; *Materials and Methods*). RFP expression remained the same and both fluorophores

were targeted to neuronal nuclei. We recorded from this GFP control worm as it crawled freely and subjected the recordings to the same analysis pipeline used for GCaMP worms. Any apparent change in fluorescence ratio *R* in this GFP control worm should be due to artifacts from motion or from other measurement noise in the system because neither the GFP nor RFP has calcium-dependent fluorescence. Extracted fluorescence signals from the GFP control worm showed that noise remains present in our system and motion artifact is likely a source (Fig. 6). Nonetheless, the GFP control worm exhibited a lower mean $\Delta R/R_0$ amplitude and a lower variance compared with the calcium-sensitive GCaMP (Fig. 7*A*). Note that this population of neurons likely includes many silent as well as active neurons. The mean and SD for GCaMP

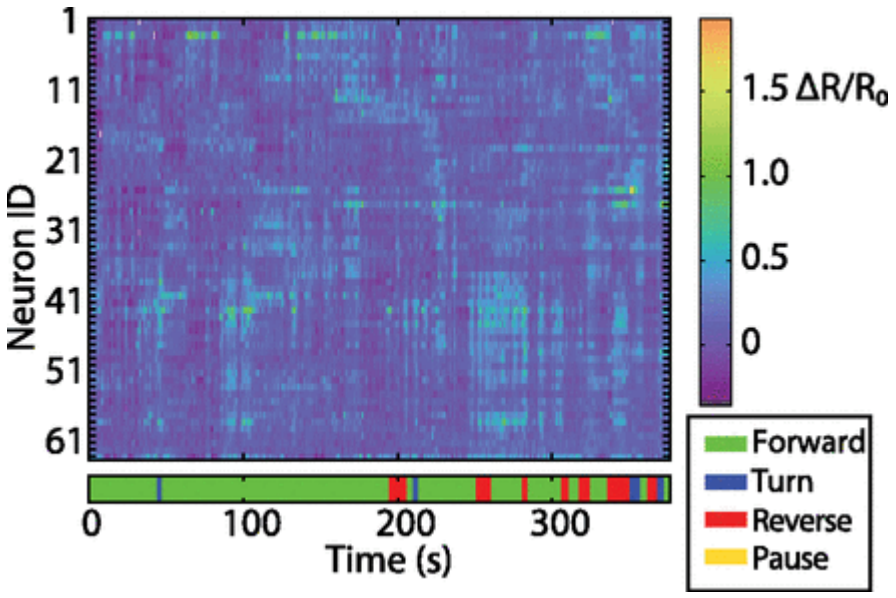


Figure 2.6: Transients observed from 63 neurons in a freely moving GFP control worm. Fractional change from baseline, ΔR/R0, of the ratio between green- and red-channel fluorescence of 63 neurons in a control worm expressing GFP and RFP in the nuclei is shown. Neural activity was extracted using the same analysis pipeline as for GCaMP worms. Color map is identical to Fig. 4.

was $\langle \Delta R/R0 \rangle_{GCaMP}$= 0.2, σ_{GCaMP}=0.26, whereas for GFP, it was $\langle \Delta R/R0 \rangle_{GFP}$=0.14, σ_{GFP}=0.15. This discrepancy suggests that the GCaMP recordings contain neural activity that is unlikely to be attributed purely to motion or noise.

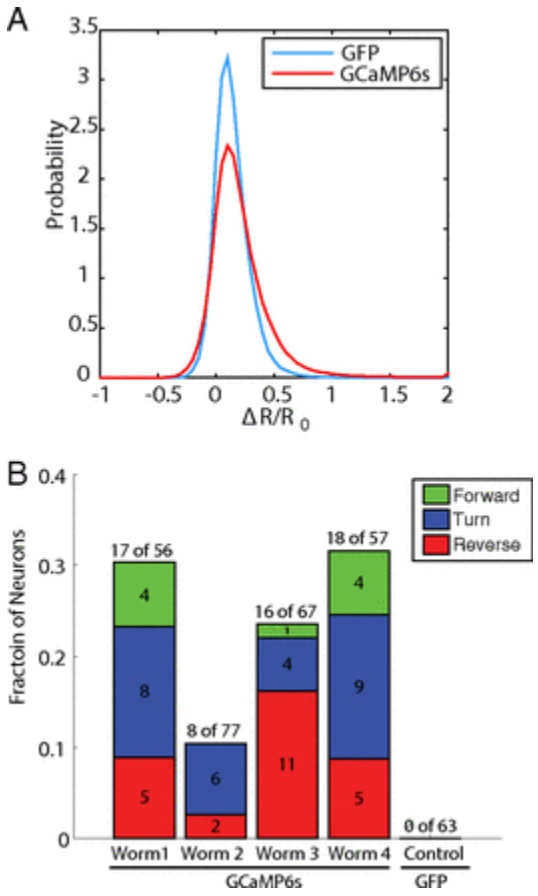


Figure 2.7: Comparison between GCaM6s individuals and GFP control worm. (A) The distribution of fractional change of ratios of fluorescent intensity values, ΔR/R0, of all neurons recorded during free behavior is shown for the four GCaMP6s worms (red) and a control GFP worm (blue). Note, this population of neurons likely includes silent as well as active neurons. GCaMP6s had larger mean and SD in its time-varying fluctuations of ratios of fluorescent intensity ⟨ΔR/R0⟩GCaMP =0.2, σGCaMP=0.26 than that of the GFP control worm ⟨ΔR/R0⟩GFP=0.14, σGFP=.15. This is consistent with GCaMP6s' role as a calcium indicator and suggests that the time varying fluorescence we observe is not merely due to motion artifact. (B) Fraction of observed neurons whose activity correlated with forward (green), turning (blue), or reverse behavior (red) above a significance threshold is shown for the four GCaMP6s individuals and the GFP control worm. Numerals refer to the number of neurons that correlated with each behavior. Number of neurons that correlate with any of the three behaviors out of total neurons observed is shown above each bar.

The nuclear-localized ratiometric imaging approach used here was selected to minimize artifact from motion and to maximize signal. Initially, we also explored alternate imaging approaches, including recording from worms expressing GCaMP in the cytoplasm and RFP in the nucleus, using either ratiometric or nonratiometric imaging. To evaluate the susceptibility of these various approaches to motion artifact, we compared the power spectra of two GFP control worms: a "nuclear" strain, AML18, which expressed both GFP and RFP in the nucleus, and a "cytoplasmic" strain AML10, which expressed GFP in the cytoplasm and RFP in the nucleus. These strains were compared for both ratiometric and nonratiometric imaging. Any apparent neural activity observed in either control worm should be due to artifact from motion or from other noise in the system. We expect that artifact due to animal motion would be most prominent at the frequency of the worm's sinusoidal body oscillations. Therefore, we compared the power spectra of the observed fluorescent transients of the two control worms to the power spectra of the animal's postural oscillations and sought the imaging approach that gave fluorescent transients with the lowest power at the frequencies of animal motion. A clear peak corresponding to animal motion was visible in the control worms for each imaging approach except for the nuclear-localized ratiometric approach (*SI Appendix*, Fig. S7). The absence of this peak suggests that a nuclear-localized ratiometric approach is less susceptible to artifact from animal motion.

We furthered explored the choice of ratiometric vs. nonratiometric imaging for our nuclear GCaMP recordings by calculating the percentage of our GCaMP recordings that can confidently be attributed to signal generally and not noise for both ratiometric and nonratiometric approaches (*SI Appendix*, Fig. S8 and Table S4). The all-nuclear-localized ratiometric imaging approach was found to have a higher portion of apparent neural activity that could be attributed to signal than a nonratiometric approach.

We speculate that a nuclear localized ratiometric approach performs most favorably because when GCaMP and RFP are both expressed in the same spatial patterns, such as in the nuclei, they are both affected similarly by many sources of noise, including motion. In these cases the calcium-insensitive RFP acts as a built-in neuron-specific control and taking the ratio of the GCaMP and RFP fluorescence intensities mitigates any noise common to both signals. Motion artifact should affect neighboring neurons similarly. We were therefore reassured to observe in our GCaMP recordings neighboring neurons that show qualitatively different temporal dynamics (see, for example, neurons 32″ and 7″ in *SI Appendix*, Fig. S4). This observation further suggests that GCaMP recordings are capturing calcium dynamics and that observed changes in fluorescent intensity cannot merely be explained by motion artifact.

2.2.4 Specific Neurons Correlate with Each of the Three Observed Behaviors

We next calculated the correlation between the dynamics of individual neurons and changes in locomotory behaviors. The roughly ∼70 neurons we observed in each worm displayed a varying degree of correlation with the behaviors we measured. To reveal neurons with significant behavioral correlations that are also unlikely to arise from motion artifact, we applied two statistical thresholds, one related to the strength of the correlation and another related to the change in fluorescent intensity. The thresholds were selected based on intrinsic properties of noise observed in the neural signals and were calibrated to the motion artifacts observed in our GFP control recordings. Briefly, we calculated the Pearson's correlation coefficient r between each neural trace and three individual behaviors: forward, backward, and turning. To be considered significant, we required that each neuron's correlation r be statistically larger than 0 as determined by bootstrapping (*SI Appendix, Methods*) and further that r always be

greater than r=0.25. To be considered significant, we also required that the change of the signal's intensity during the behavior exceed a threshold based on the intensities observed in the GFP control worm, which arise solely due to noise, including motion artifact (*SI Appendix, Methods*). Always at least 8 neurons and as many as 18 neurons in a worm passed our criteria for significance and correlated with either of three behaviors, forward, backward, and turning, with an average coefficient of r=0.36r=0.36 (Figs. 7*B* and 8 and *SI Appendix*, Fig. S9).

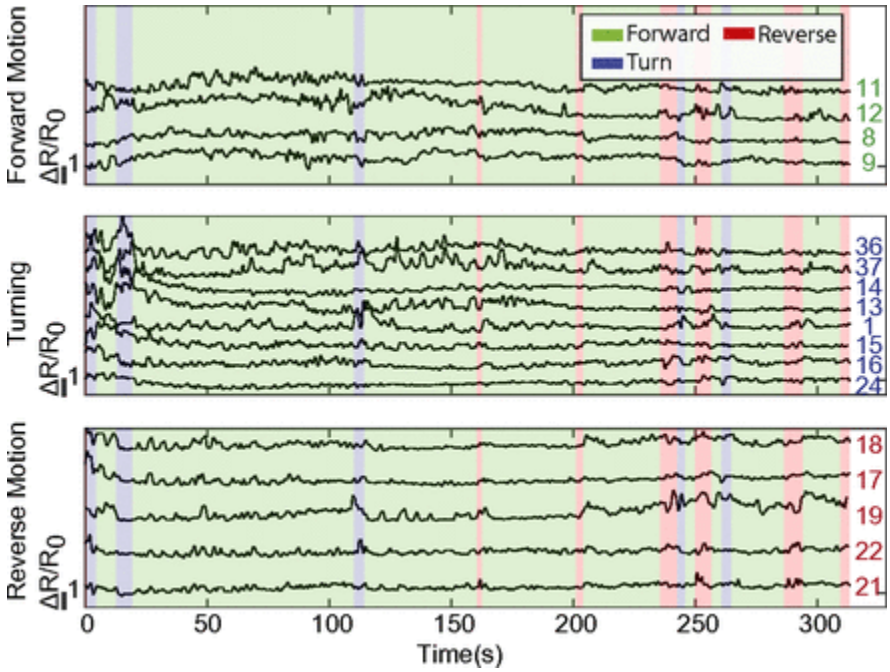


Figure 2.8: All neurons whose activity correlated with either forward, turning, or reverse behavior above a significance threshold are shown for worm 1. The significance threshold was calibrated to the noise observed in the GFP control recordings. Vertical scale bar indicates ΔR/R0 of 1 (100%). Each neuron's ID number is indicated. Note neuron numbers do not indicate correspondence across worms. Additional individuals are shown in SI Appendix, Fig. S9.

We repeated the same analysis on the GFP control worm recordings and were reassured to find that of 63 neurons not a single one had fluorescence intensity dynamics that met the threshold criteria for significance in its correlation with behavior (Fig. 7*B*).

2.2.5 Comparison of Neural Position

We sought to investigate the spatial location of those neurons that had calcium transients that correlated with behavior (Fig. 9). Plotting the 3D neuronal positions of those neurons that passed our significance threshold, we occasionally see a correspondence in location between the behavior-specific neurons across worms. For example reversal neurons 17 and 18 in worm 1 are in strikingly similar position to reversal neuron 7″ and 8″ in worm 3 (*SI Appendix*, Fig. S10), suggesting that these may be the same neuron across worms.

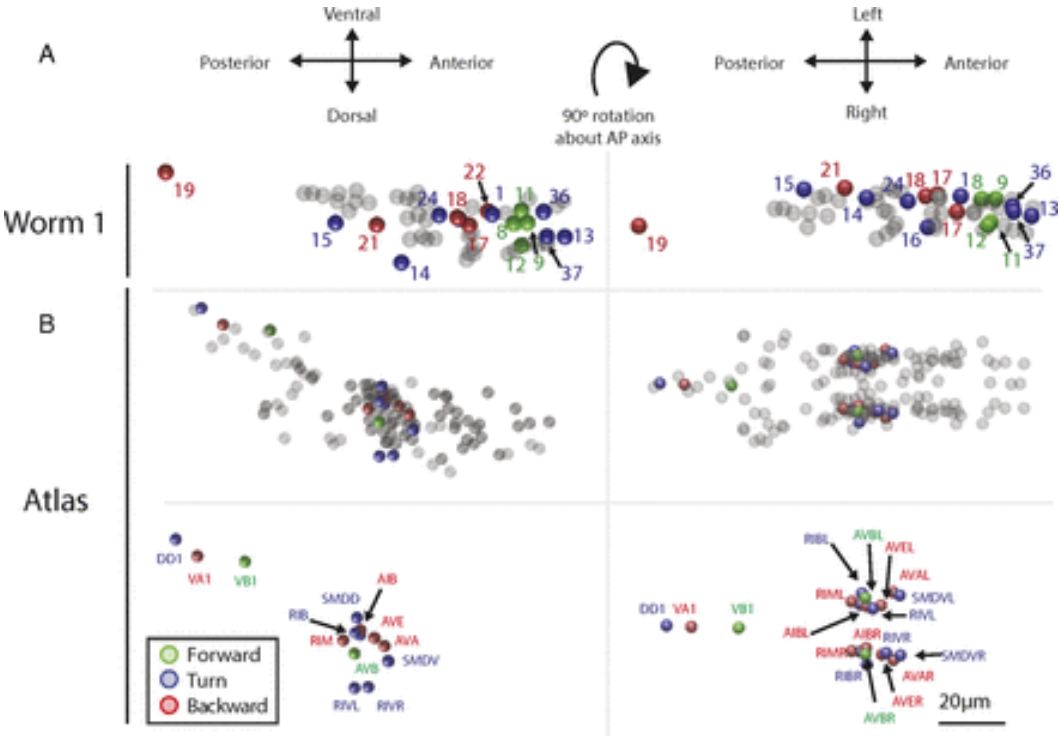


Figure 2.9: The position of recorded neurons for worm 1 is plotted in 3D and compared with an atlas. (Left) Dorsal-ventral plane view of the animal. (Right) Left-right plane view of the animal. (A) Neurons whose activity correspond to forward, turning, or reverse are colored and labeled with a neuron ID corresponding to Fig. 4. Remaining neurons are shaded gray. Additional worms are shown in SI Appendix, Fig. S10. (B) The position of all known neurons are plotted using reference data culled from the WormBase Virtual Worm Project. Neurons that have previously been reported in the literature as implicated in a behavior are colored accordingly (SI Appendix, Table S5) and labeled with their neuron name. Colored neurons are shown both in and out of context of all other neurons for clarity.

To compare recordings across worms or to compare with the literature, it would be informative to know the identity of each neuron in our recordings, e.g., which neuron is AVA, AVB, etc. We wondered whether neuron position information alone would be sufficient to systematically match neurons across worms or to assign an identity to each neuron with respect to the known neuroanotomical atlas from electron microscopy data[7]. We designed an experiment that measured the accuracy with which neurons in one worm could be matched to neurons in another based on position information alone. An integrated transgenic line was generated that expressed RFP in the nuclei of all neurons and expressed GFP in a genetically defined subset of neurons of which 11 could be unambiguously determined by eye (strain AML5; *Materials and Methods*). Two adults of similar age were immobilized and imaged. We tested various 3D alignment, registration, or nonlinear warping algorithms that relied only on neural position information to match neurons between the two animals. Candidate algorithms were given position information of all neurons observed in the head (127 neurons for worm A and 128 neurons for worm B). Matchings were validated by inspecting whether the subset of 11 unambiguous GFP labeled-neurons, whose identities are known, were matched correctly. Simply aligning the two worms and matching nearest neighbors resulted in correctly matching 3 of the 11 known GFP neurons (*SI Appendix*, Fig. S11). Of seven algorithms from the literature that were tested (*SI Appendix, Methods*), a nonrigid point set registration algorithm (34) was found to perform best but still only correctly matched 6 of the 11 known GFP-labeled neurons (*SI Appendix*, Fig. S11).

Our neural identity validation experiments suggest that position information alone is insufficient to correctly assign neural identities across worms. Therefore, we do not know the true identities of the neurons we observe (*Discussion*). As in previous whole-brain imaging

studies[8], [33], we instead turn to evidence from the literature to reveal likely candidate neural identities to assign to our neurons based on a combination of observed neural activity, previously reported neural function and neuroanotomical position. We found reports in the literature of nonsensory neurons implicated in the three locomotory behaviors of interest (*SI Appendix*, Table S5). We plotted these candidate neurons' position in three dimensions (Fig. 9 and *SI Appendix*, Fig. S10) using data culled from the WormBase Virtual Worm Project (caltech.wormbase.org/virtualworm/), which in turn is based on electron microscopy data from ref. 7. Comparing this atlas to data from our three worms provides plausible candidate neural identities for those neurons we observed who had activity correlated with forward, turning, and reversing. For example, the position and activity of neurons 17 and 18 in worm 1 is consistent with these neurons being AIBL or AVEL.

2.3 Discussion

The imaging system presented here allows for whole-brain recording of calcium activity with cellular resolution in a freely moving *C. elegans*. We used this system to investigate dynamics of neurons in the worm whose activity correlates with forward, backward, and turning modes of locomotion. We observed a number of neurons in each worm whose activity correlated with behavior. Some of these neurons compare favorably with results from the literature, whereas others appear to have previously unidentified roles in locomotory behavior. This study is the first example, to our knowledge, of recorded calcium dynamics from nonsensory neurons in the head that correlate with turning. We also characterize noise in the system due to motion or other artifacts and show that the calcium activity of the neurons who are most correlated with behavior are unlikely to be explained by motion artifact. We believe this work represents a

significant advance toward studying how population dynamics of a brain-sized neural network generates behavior.

Of nearly 80 recorded neurons, at least 8 and as many as 18 neurons in each worm were observed to have neural signals that correlate with behavior and exceed our noise threshold based on an analysis of the GFP control worm. Aggregate, 23% of neurons were found to correlate significantly with behavior in our GCaMP worms, whereas none were found in our GFP control. We suspect that there may be other additional neurons that have activity that also correlate with behavior but that their signals are too weak to unambiguously rule out contributions from noise, even using a ratiometric approach. Revealing the weakest of neural signals is a challenge that will need to be addressed in future work.

The system currently records intracellular calcium levels from within neuronal nuclei. Recording from the nuclei is advantageous because the spatially distinct nuclei allow each cell to be distinguished from its neighbors. Moreover, compared with a cytoplasmic approach, the all-nuclear approach is less susceptible to artifacts from animal motion. Nuclear recordings were successfully used previously in two whole-brain imaging studies of anesthetized and immobilized *C. elegans*, and those works argue that nuclear calcium levels capture the calcium dynamics of the rest of the neuron[8], [33]. Recordings from the cell body are the most prevalent in the literature and have previously been used to study activity of a number of neurons relating to locomotory behavior[18], [36], [37], [42]–[44]. Because *C. elegans* nuclei are thought to be porous to calcium and because the nuclei take up a large portion of the cell body, nuclear recordings used here likely capture calcium transients observed in the cell body. There are, however, known neurons where calcium signals in the processes are different from those in the cell body and, by extension, the nuclei[46]–[49]. It remains to be seen whether independent

calcium dynamics in the processes are unique to these few specific neurons or are a more general phenomenon. For example, a recent investigation of three *C. elegans* interneurons found that calcium activity peaked more quickly in the process than the cell body but was otherwise similar[25].

Although it is tempting to try to explore neural dynamics in the processes by expressing a calcium indicator in the cytoplasm of all neurons, pan-neuronal cytoplasmic expression of a fluorophore is impractical for segmenting individual processes. Currently single-cell recordings remain the most viable method for probing neural dynamics in the processes. Future work is needed to solve the problem of segmenting densely labeled neuronal processes in freely moving animals.

This system successfully identifies and tracks neurons through time within a given worm. One of the advantages of working in *C. elegans* is that its neural anatomy and connectivity has been mapped[7]. Unfortunately, when all neurons are uniformly labeled there is currently no systematic and reliable way of relating identified neurons across worms or to the known atlas. This challenge has plagued all previous pan-neuronal imaging studies in adult *C. elegans*[8], [33] and remains unresolved here. Conventional wisdom in the field suggests that the worm's neuroanatomy is highly stereotyped across adults, and this conventional wisdom is supported by a comparison of neurons in the tail of three worms[50]. The neural position validation experiments presented here, however, have led us to conclude that worm-to-worm variability in neuronal position in the head is large enough to pose a formidable challenge for neuron identification. Future work is needed to solve this neural identity challenge. One potential approach would be to develop worms that have multicolored fiducial references that can be used for 3D warping and registration.

The approach here records images of the entire worm's body and posture as the animal crawls. We use the body posture to define four behaviors via an eigenworm analysis[13]. Future work could use the video recordings of the animal's entire body to correlate neural activity with a variety of other behaviors that are also captured by our instrument. For example, full-body recordings have been used to enumerate many more *C. elegans* behaviors[40] and to study such physiologically relevant behaviors as deep ventral bends[45], foraging head oscillations[51], coiling[34], pumping[52], defecating[53], and egg-laying[54], all of which exist in our datasets. Recent work in flies has shown the value of capturing images of full body posture for analyzing behavior[55]. An analysis similar to that work, but which also combines population neural activity, could be performed in *C. elegans* using the methods presented here in the future.

The current system uses a spinning disk confocal imaging modality. Our system is fully modular, and the 3D tracking microscopy and off-line image analysis are well suited to take advantage of other imaging modalities such as light-field or two-photon microscopy, as well as advances in genetically encoded calcium indicators[56] and voltage indicators [57]–[59].

2. 4 Materials and Methods

2.4.1 Strains.

We cultivated transgenic worms on nematode growth medium (NGM) plates with OP50 bacteria. OP50 plates were made by seeding 6-cm NGM plates with 250 µL of a suspension of OP50 bacteria in lysogeny broth. All worms used in this study were young adult hermaphrodites. Worms were cultivated and handled in the dark or under red-light illumination to minimize potential photobleaching from ambient light.

Strain AML14 (wtfEx4[P*rab-3*::NLS::GCaMP6s, P*rab-3*::NLS::tagRFP]) was generated by coinjecting into an N2 background a P*rab-3*::NLS::tagRFP plasmid (gift of O. Hobert, Columbia University, New York) (48) with a derivative of that plasmid where NLS::tagRFP was replaced with a GCaMP6s sequence flanked by nuclear localization sequences described in (11). Strain AML18 (wtfIs3[P*rab-3*::NLS::GFP, P*rab-3*::NLS::tagRFP]) was generated by coinjecting into an N2 background a P*rab-3*::NLS::RFP plasmid (gift of O. Hobert) (48) with a derivative of that plasmid where RFP was replaced with a GFP sequence and then integrated via UV irradiation. Strain AML10 (otIs45[P*unc-119*::GFP]; otIs355[P*rab-3::NLS::tagRFP*]) was generated by crossing a male of strain QW1155 (otIs355[P*rab-3*::NLS::tagRFP]) (gift of M. Alkema, University of Massachusetts Worcester, Worcester, MA) with a hermaphrodite of strain OH441 (otIs45[P*unc-119*::GFP]) (gift of C. Murphy, Princeton University, Princeton). Strain AML5 (otIs355[P*rab-3*::NLS::tagRFP]; KyIs51[P*odr-2b*::GFP]) was generated by crossing a male from strain QW1155 (otIs355[P*rab-3*::NLS::tagRFP]) (gift of M. Alkema), with a hermaphrodite of strain CX3300 (KyIs51[P*odr-2b*::GFP]) (gift of C. Bargmann, Rockefeller University, New York). Strain N2 bristol was used for WT.

Strain AML14 was used for all calcium imaging experiments. Individual animals of extrachromasomal strain AML14 were selected for bright and uniform expression on a fluorescent dissection scope before use.

2.5 Appendix

2.5.1 Microscopy

The microscope is built on the base of a Nikon Eclipse TE2000S inverted microscope. A schematic with details of optical elements is shown in Supplementary Figure S12. Illumination is delivered from below the sample. Dark-field illumination is provided by a halogen lamp filtered with a near-infrared longpass filter (Omega Optical #3RD710LP) and directed by light guides so as to land obliquely on the sample from below. GCaMP6s and RFP in the sample are excited by 561nm and 488nm light from two diode-pumped solid state lasers (Coherent Sapphire 561 LP and 488 LP, each with 200-mW maximum power). Light from the two lasers are combined using a dichroic mirror (Semrock FF518-Di01-25x36) and then coupled into an optical fiber so as to illuminate the sample through a spinning disk confocal unit (Yokogawa CSU-X1) and 40x objective (Nikon CFI Super Fluor, 1.3 NA). Power at the sample for the GCaMP6s experiments was measured to be 43 mW / mm2 and 13 mW / mm2 for 561 nm and 488 nm light respectively. For GFP control worm experiments, the blue laser intensity was adjusted such that the raw GFP fluorescence intensity matched that observed in a GCaMP6s worm.

Fluorescent images of GCaMP6s and RFP are recorded using a 40x objective via the spinning disk on a ‘Scientific’ CMOS (sCMOS) camera (Hamamatsu Orca Flash v 4.0). Four dichroic mirrors ensure that only emitted light of the appropriate frequency enter the camera. The first dichroic mirror 1 (Edmund Optics, 650nm SP Dichroic) rejects stray near-infrared light that comes from the dark-field illumination source. The second dichroic (Semrock Di01-T405/488/568/647-13x15x0.5), located in the spinning disk unit, allows the emitted green and red light to pass, but rejects the excitation laser light. The third and fourth dichroics (Semrock FF555-SDi03-25x36), splits the emitted light into red and green channels and then recombines

them so that they are imaged side-by-side on the camera. Additional emission filters (Semrock FF01-520/32 and FF01-609/54) provide further light rejection.

Fluorescent images are also recorded at low magnification and high depth-of-field through the 10x objective above the sample (Nikon Plan Apo 10x 0.45 NA) to facilitate real-time xy tracking. In that imaging path, fluorescent light passes from the objective, through a longpass filter (Semrock LP02-568RU-25) to reject excitation light, and then is reflected by a dichroic mirror (Nikon 660nm LP) and imaged onto a CMOS camera (Basler acA2000-340km). To record animal behavior, darkfield near-infrared light is imaged through the same 10x objective. The near-infrared light passes through the dichroic to form an image on a second CMOS camera (Basler acA2000-340km-NIR).

2.5.2 Image Acquisition

Three cameras were used to simultaneously acquire high- and low-magnification fluorescence and behavior images. Their properties are listed in Supplementary Table S6. To synchronize the recorded video streams during post-processing, a bright white flash was generated from a consumer camera flash (Bower SFD328) that was simultaneously visible on all three cameras.

Raw uncompressed high-magnification fluorescent images were recorded via custom Labview software to a high bandwidth solid state drive (OCZ Revodrive 350, 1TB), so as to handle the large datastream of 288 MB/s (200fps of 1200x600 pixel 16 bit-depth images). Low magnification fluorescence and behavior images were stored by custom software written in the programming language C using JPEG lossy compression on standard hard drives[17].

2.5.3 Volumetric imaging and 3D tracking

The 40x objective is mounted on a piezoelectric stage (Mad City Labs Nano-F200S) that allows it to translate along z under computer control. To acquire volumetric fluorescent images, the objective is driven with a 3 Hz, 4 V peak-to-peak triangle wave from a function generator (Hewlett-Packard HP33120A) so that the objective passes through the sample five times per second.

A triangle wave was chosen instead of a sawtooth because the objective was able to accurately follow the 3 Hz triangle wave in contrast to the sawtooth. As a result of using the triangle wave, neurons above or below the center of the brain along the optical axis (z) are sampled irregularly in time, although always twice in a 333 ms interval. Neurons at the extreme top and bottom of the brain experience the most uneven sampling. A typical C. elegans brain extends 33 µm in z whereas the scan range extends up to 51 µm in z. Active feedback keeps the worm's brain centered in the middle of the scan range. We estimate that neurons located on the extreme top and bottom of the worm are sampled with a duty cycle that alternates between 59 ms and 274 ms periods. The vast majority of the neurons, however, are in the center of the objective's scan range where sampling is most uniform at every 167 ms.

The animal crawls in the imaging arena atop an x-y motorized stage with linear position encoders (Ludl BioPrecision2). Active feedback tracks the fluorescence of the worm's brain and adjusts the stage to keep it in the field of view. As the worm crawls, a modified version of the MindControl software[17] (source code available at http://git.io/colbert) monitors the low-mag fluorescent video stream, locates the worm's head in xy by finding the centroid of the cluster of fluorescent neurons comprising the worm's brain, and then adjusts the velocity of the motorized stage to compensate for the worm's motion. This xy feedback loop updates at 67 Hz.

To track the animal's motion in z, custom Labview software implements a second feedback loop that monitors the high-magnification fluorescent images and adjusts the objective's z-position. After each pass of the objective (6 Hz), the software estimates the center of the worm's head in z by finding the image plane that has pixel values with the highest standard deviation. The software monitors the z-piezo's position through a DAQ board (National Instruments PCI-6251) and adjusts 3 the z-piezo's DC offset after each stack to compensate for any head motion by sending an offset voltage via the DAQ that is added to the piezo's driver by an analog circuit.

2.5.4 Free behaving whole-brain imaging experiments

The imaging arena consists of a 100 mm diameter petri dish, turned upside with an NGM pad where agarose has been used instead of agar. Worms crawl on agarose. A 50 x 45 mm wide cover slip covers the worm and rests on 127 µm plastic spacers that prevents the cover slip from applying pressure on the worm and impeding its motion. Mineral oil was used to fill the area between the agarose pad and the cover slip to improve optical quality of low-magnification behavior images. Note the mineral oil has no effect on the high-magnification fluorescence imaging. In the imaging arena, the worm's mean speed was slower and the worm reversed more often than on an open-air agar plate. Other metrics of behavior in the whole-brain imaging arena were within one standard deviation of what was observed on an open-air agar pad, see Supplementary Figure S1 and Supplementary Table S1. Young adults were picked, washed in M9 buffer, and were placed on the imaging arena and allowed to acclimate for five minutes before imaging. Half of the worms were imaged right side facing the high-magnification

objective, and half of the worms were imaged with their left side facing the high-magnification objective (Supplementary Table S7). Worms crawled freely in the arena during imaging.

2.5.5 Immobilized calcium imaging experiments

In immobilized calcium imaging experiments, a GCaMP worm (strain AML14) was immobilized on an agarose pad using polystyrene beads[60]. Unless otherwise noted, basal neural activity was recorded as in the freely-moving experiments. For example, for power spectra experiments shown in Supplementary Figure S5, only a single image plane was recorded and that image plane was recorded at a much faster 200 fps. For neuron counting experiments shown in Supplementary Figure S2, exposure time and z-scan rate were varied accordingly.

2.5.6 Extracting neural signals

Neural signals were extracted from the raw fluorescent images using a multi-step analysis pipeline that involving segmentation, registration and tracking using a human-supervised but largely-automated approach. The pipeline relied heavily on a variety of techniques from image processing and computer vision, as described below.

Cell bodies were located automatically by inspecting the nuclear-localized RFP fluorescence images. First, high magnification RFP videos were separated into a time-series of brain volumes. Using the centerline found in the low magnification behavior video, each slice in the volume is transformed into the curvilinear coordinate system of the worm centerline. This “straightens” the worm, mitigates the effects of motion and rotation and reduces deformations due to worm curvature. Image stabilization is also performed on the straightened worm to further reduce the effect of motion on relative neuron position. Straightening and image stabilization

result in a time-series of brain volumes that appear as if they came from an immobilized worm. Automated segmentation is then performed on the straightened worm to find the centroids of each neuron in each volume.

Next the correspondence of neural labels are tracked through time. A non-rigid point set registration algorithm[61] was used to match the identities of a set of neurons at one time point to a set at a different time point using only the RFP neural centroid positions. For any two time points, a number of factors could prevent some neurons from perfectly matching. For example, neurons occasionally become dim, are occluded or move with animal motion even after "straightening." On rare occasion neurons may even leave the field of view. As a result we found that tracking neurons by comparing only consecutive volumes through time resulted in an unacceptable accumulation of errors. Instead we perform multiple comparisons for neurons at any given time point. 175 volumes from different randomly selected time points in the recording are designated as reference time-volumes. For each time-volume in the recording, we use the non-rigid point set registration algorithm to compare the locations of the neurons in that volume to all 175 reference volumes. A statistical analysis is then used to assign a track identity to the neuron based on the results of all 175 comparisons. This approach was found to be more robust to transient errors than the sequential approach.

Because the straightening process itself can introduce positional artifacts, neuron positions and putative track identities are then further refined in the raw unstraightened image volumes using a three-dimensional spatial interpolation with human-supervision. For each time-volume, an interpolant is created between it and the previous time-volume using the putative neuron identities that were found with the straightened worms. The interpolant is then used to estimate the position of its corresponding neuron in the new volume via a 3D thin-plate spline

spatial interpolation based on the neuron's relative position to other tracked neurons in the most-similar previous volume. The position is refined by searching for local maxima in RFP intensities within a user-defined radius of the initial estimate (up to 10 μm). Each assignment is supervised by a human to ensure predicted positions match the correct neuron. The process is repeated until no more neurons can be consistently detected. In a typical analysis run, 5% of neuron-frame annotations are corrected by hand while the remaining annotations from the automated algorithm are approved by the human as-is. Certain areas, such as where neurons are most densely concentrated or portions of the nerve cord are more challenging for the automated tracker and so many of the hand annotations are concentrated there. The distribution across neurons of the accuracy of the tracker is shown in Supplementary Figure S13. Additionally, imaging planes recorded from the side of the worm furthest from the objective are slightly dimmer and nosier than those recorded nearest to the objective. As a result, the automated algorithms perform slightly worse at segmenting and tracking neurons on the far side compared to the near side.

To extract fluorescence intensity of neurons given their positions, the region of each neuronal nuclei is found by searching within a volume defined by a 2μm diameter sphere centered on the neuron's position. A threshold and area filter are then used to detect the pixels of interest within this sphere corresponding to the neuron's nucleus. The average RFP and GCaMP6s intensity was calculated over these pixels to give the fluorescence intensity of the neuron at that time point. Photobleaching effects were removed independently for each neuron and each fluorophore by subtracting the exponential component of the fluorescence intensity over time. The GCaMP6 and RFP intensities are then used to define the ratio R. The neuron activity is expressed as the fractional change of this ratio, $(R - R0)/R0$, written as $\Delta R/R0$, where

R0 is defined as the lower 20th percentile fluorescent intensity value for a given neuron. On rare occasion, a combination of worm motion and tracking 6 latency caused neurons to briefly leave the field of view. These data were omitted from the analysis and appear as white gaps in plots of neural traces. Neurons were sorted by hierarchical clustering of the correlation matrices (Figure 5 and Supplementary Figure S6) using a Euclidean distance metric.

2.5.7 Comparing motion artifact in nuclear vs cytoplasmic expressing worms

To determine the imaging approach that is least susceptible to motion artifact we imaged two control worms during free locomotion that either expressed nuclear localized GFP and RFP in all neurons (strain AML18), or expressed cytoplasmic GFP and nuclear RFP in all neurons (strain AML10) and compared ratiometric and non-ratiometric approaches (Supplementary Figure S7). For each of the four conditions, we extracted apparent activity from each neuron, either as a change in the ratio from baseline, $\Delta R/R0$, for the ratiometric approach, or as a change in fluorescence from baseline, $\Delta F/F0$, for the non-ratiometric approach. Within each condition, the power spectrum for each neuron was calculated and averaged together. To quantify the animal's motion, centerlines of the worm were used to measure a relative angle between head orientation and overall body orientation. Specifically, the angle used was defined as the difference between the vector from the tip of the worm to the tail, and the vector from the tip of the worm to a point along the worm's centerline 10% posterior from the tip of the head. The power spectrum of these angles indicates the frequency of the head oscillations. Because both GFP and RFP are insensitive to calcium, any feature in the power spectra of apparent neural activity can be attributed to motion or noise. Comparing the power spectra of the apparent neural

activity to the power spectra of animal motion provides insights into how much artifact in the apparent neural activity can be attributed to animal motion.

2.5.8 Calculating portion of apparent neural activity that can be attributed to signal and not noise

To estimate the portion of neuron-time points in our GCaMP recordings that could be attributed to signal and not noise, including noise from motion artifact, we compared recordings from GCaMP worms (strain AML14) to those of a corresponding nuclear localized GFP control worm (strain 7 AML18) as in Supplementary Figure S8 and Supplementary Table S4. The GCaMP "experimental" recordings, are assumed to contain both signals and noise while the GFP "control" recordings are assumed to contain only noise. A neuron-time-point is said to arise from signal if the likelihood that it arose from the "experimental" recoding of GCaMP and not the GFP "control" recordings is greater than 95%. By performing a statistical analysis of the distributions of ΔR/R0's observed in the experimental GCaMP worms and the control GFP worm, respectively, we can calculate the fraction of our observations per time that are in fact signal and not noise. The analysis is as follows:

Let γ be a neuron-time-point. Here γ will be a ΔR/R0 value, but later for non-ratiometric calcium imaging it will be allowed take values of ΔF/F0. The probability that γ arose from the experimental GCaMP distribution f (γ) is, related to the probability density functions of GCaMP and GFP, ρGCaMP and ρGFP (shown in Figure 7), by the equation

$$Prob(GCaMP|\gamma) = \frac{\rho GCaMP(\gamma)}{\rho GCaMP(\gamma)+\rho GFP(\gamma)} \equiv f(\gamma) \qquad (1)$$

The value of γ required to exceed 95% likelihood, $\gamma*$, is given by,

$$\gamma* = \text{argmin}\gamma\ [f(\gamma) > 0.95] \quad (2)$$

The fraction of neuron-time-points in our recordings that exceed this likelihood threshold, <Nsignal> is given by

$$< N_{signal} > = \int_{\gamma*}^{\infty} \rho GCaMP(\gamma) d\gamma \quad (3)$$

To compare a ratiometric to non-ratiometric approach, <Nsignal> was also calculated for the same GFP and GCaMP recordings when analyzed in a non-ratiometric way. In this context γ took on values of ΔF/F0, but the analysis was otherwise the same.

To extract calcium dynamics from GFP and GCaMP recordings non-ratiometrically, the process was the same as in ratiometric recordings except the step where the green-channel fluorescence for each neuron was divided by the RFP fluorescence intensity was omitted.

2.5.9 Analyzing behavior

Position, velocity and postural information were recorded during imaging sessions. The location of the motorized stage was recorded at 20 Hz which, when combined with the imaging, provides the worm's position and velocity within the arena.

The worm's centerline also provided important behavioral information. The centerline of the worm was found in each low-magnification behavior image at 42 fps using a semi-automated approach that relied on an active-contour model[62]. The tip of the head and tail was first found manually in every fifth image. This was interpolated through time and served to fix the first and

last point of the centerline in each frame. Images were preprocessed with a gaussian blur and then active contours of 100 points were used to find the centerline of the worm in each frame. As in the classic active contour model, an elastic contour iteratively relaxes into a minimum energy state determined by an image energy defined by the pixel intensities of the image. In this case the lowest energy corresponds to resting along the centerline.

The active-contour model in [62] was modified to accommodate situations when the worm touched itself or crossed over its body. A repulsive force between the first and last third of the contour was used when the head and tail of the worm were in close proximity to prevent the two ends of the contour from merging. Instances where the worm crossed itself were detected automatically and the repulsive force was turned off to permit the crossing. The contour of the first frame was initialized manually; each subsequent frame was initialized with the final contour of the previous frame. On rare occasions the algorithm settled into a local energy minima that failed to match the centerline. In those instances, a human adjusted the model's parameters until the global minima corresponding to the centerline was found.

The speed of the worm was measured by combining stage position information and the worm's center of mass in the low magnification behavior image. Change in centerline curvature determined whether the worms moved forward or backwards. To find velocity, we fit the centerline curvature of the worm to a sine wave and scored the velocity as negative when the wave propagated towards the head as opposed to the tail.

The worm center-of-mass velocities were classified into forward, backward, and non-moving states using k-means clustering. The non-moving states were further separated into turning and paused states by analyzing the worms posture using "eigenworms"[13]. The magnitude of the projection of the worm's posture onto the third eigenworm is larger during the

deep bends in the worms shape that often occur during turns. We clustered the magnitude of this value into two groups to separate pausing and turning states. Pausing bouts shorter than 0.75 seconds were excluded from the ethogram.

2.5.10 Criteria for correlating behavior with neural signals

Neurons were considered significantly correlated with a behavior if both the Pearson correlation coefficients, r, and the increase in neural activity were above a threshold. For correlations between activity and behaviors, 10,000 bootstrap samples of paired $\Delta R/R0$ values and behaviors were drawn from random time points and confidence bounds for r were calculated. Neurons were significant if r was greater than 0.25 and the 95% confidence interval did not overlap with 0.

Increase in neural activity for a given class of behavior (e.g. turning) was measured as the difference between the average signal when the animal performed that class of behavior and the average signal during all other times. A threshold of this intensity change was derived from the recordings from the GFP control worm shown in Figure 6. The GFP control worm has calcium insensitive GFP in place of GCaMP and thus all observed signals are artifactual. The threshold was based on the distribution of intensity changes observed during behaviors in the control. We set our significance threshold for changes in intensity to be 5-fold greater than the standard-deviation of the changes observed in the control, $5\sigma_{control}$, because fluorescence changes of this size were not observed in the GFP control worm but were still common in the GCaMP6s worm. The same intensity threshold was used for all neurons in all worms.

2.5.11 Behavioral Control Experiments

For behavioral control experiments shown in Supplementary Figure S1 and Supplementary Table S1, Wild Type (N2) and GCaMP (AML14) animal behavior was measured on an open-air NGM agar plate and compared to the behavior of the four recorded GCaMP animals in our whole-brain imaging apparatus during recording. In open-air agar plate experiments, approximately 20 young adult worms were washed in M9 and placed on a 10 cm NGM plate (off-food) where their movements were recorded for 30 minutes at 14 frames per second. Three sessions were used for each strain. Worms were tracked in parallel and analyzed by a modified version of the parallel worm tracker[38]. Trajectories for each worm were recorded until the animal collided with another animal or became obscured. To guarantee that each analyzed worm trajectory came from a unique worm, all trajectories that commenced after the end of the first trajectory were omitted. In this context, the following behavioral definitions were used: Speed was calculated from the motion of the centroid of the animal and Gaussian smoothed over a time window of 0.5 s. Pauses were defined as worm speed below 0.01 mm/s for more than 0.5 s. Reversals were identified by the tracker as described in [38]. A run was defined as sustained movement greater than 0.01 mm/s that is uninterrupted by pauses or reversals. To compare the behavior of the GCaMP worms during whole brain imaging, center of mass trajectories of the GCaMP recordings were analyzed and subjected to the same analysis pipeline as the multi-worm experiment. Note that in order to accommodate the multi-worm tracking, the behavioral definitions used in the context of this comparison are different than those used throughout the rest of the paper.

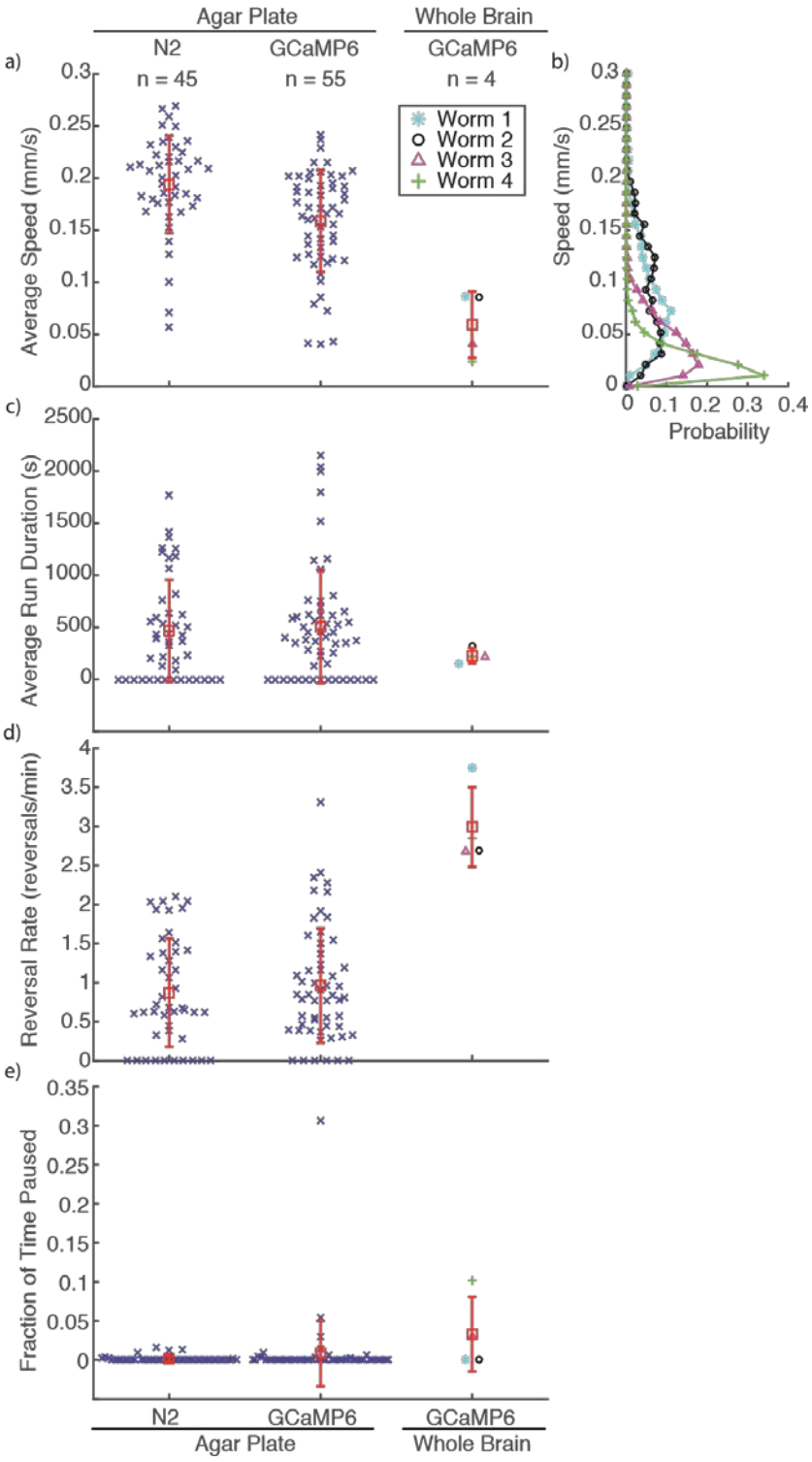
2.5.12 Neural Identification Testing

Worms were made to express nuclear localized RFP in all neurons and GFP in the cell body of a small subset of neurons driven by the odr-2b promotor[63]. GFP expression was sparse enough such that 11 neurons could be unambiguously identified across worms by eye. Two similarly aged adult worms were immobilized using the bead method[60] and imaged on a spinning disk confocal microscope via a 60x 1.4 NA objective using 300ms exposures and a z step size of 0.25 μm. The 11 locations of neurons were identified in each worm by hand.

Various 3D registration and non-linear warping algorithms were tested for their suitability to correctly identify the same neurons across two worms. Seven algorithms were selected for comparison from those implemented and tested in [61] including 'EM_TPS" [64], "EM_GRBF"[65], "TPS_L2"[61], "GRBF_L2"[61] , "TPS_KC"[66], "GRBF_KC"[66], and a simple rigid transform. Sample code from [61] was used, although parameters were optimized for our C. elegans neural dataset. Each algorithm was given only information about the position of the neurons. The algorithm was validated by observing how many of the 11 GFP labeled neurons were correctly matched across the two worms.

3.5 Supplemental Figures

Figure 2.10 (following page): Behavioral control experiments comparing GCaMP strain (AML14) to Wild Type (N2) and comparing animal behavior on an open-air agar plate and during whole-brain imaging. Behavior metrics compared are a) mean speed c) average run duration d) reversal rate and e) fraction of time paused. Each worm recorded on an open-air agar plate is marked with a blue 'x'. Worms recorded in the whole brain imager are shown as follows: Worm 1 is denoted by a blue asterisk, Worm 2 by a black circle, Worm 3 by a purple triangle and Worm 4 by a green cross, corresponding to the same worms shown in Figure 4. Red square and error bars represent mean ± standard deviation across worms. Each point denotes the average value for a unique worm during one recording, except for panel b) which shows probability distribution of each worm exhibiting a given speed during its recording.


Agar Plate
Whole Brain
N2
GCaMP6
GCaMP6
n = 45
n = 55
n = 4
a)
b)
c)
d)
e)
Worm 1
Worm 2
Worm 3
Worm 4
Average Speed (mm/s)
Speed (mm/s)
Probability
Average Run Duration (s)
Reversal Rate (reversals/min)
Fraction of Time Paused
N2
GCaMP6
GCaMP6
Agar Plate
Whole Brain

Arena Type	Open-air agar plate		Whole-brian imager
Strain	Wild Type (N2)	GCaMP6s (AML14)	GCaMP6s (AML14)
Speed (mm/s)	0.19 ± .05	0.16 ± 0.05	0.06 ± 0.03
Run Duration (s)	467 ± 489	507 ± 544	227 ± 72
Reversal Rate (reversals / min)	0.87 ± 0.69	0.96 ± 0.73	2.99 ± 0.51
Fractional Time Paused	0.001 ± 0.004	0.008 ± 0.042	0.033 ± 0.048
Number of Worms	45	55	4
Trajectory Duration (min)	5.9 ± 5.5	7.6 ± 6.7	3.6 ± 1.8

Table 2.1: Summary of behavioral control experiments shown in Supplementary Figure S1 comparing behavior of GCaMP strain (AML14) to Wild Type (N2) and comparing behavior of GCaMP strain in and out of the whole-brain imaging chamber. All values are mean ± standard deviation and are averaged per worm.

Strain	Substrate	Average Speed (mm/s)	Reference
GCaMP6	Whole-Brain	0.06 ± 0.03*	This study
GCaMP6	NGM Agar Plate	0.16 ± 0.05*	This study
N2	NGM Agar Plate	0.19 ± 0.05*	This study
N2	NGM Agar Plate	0.174	[12]
N2	NGM Agar Plate	0.219 ± 0.29*	[7]
N2	NGM Agar Plate	0.016	[13]
N2	NGM Agar Plate	0.165	[14]
N2	NGM Agar Plate	0.25	[15]
N2	NGM Agar Plate	0.12	[16]
N2	NGM Agar Plate	0.18	[17]
N2	NGM Agar Plate	0.232	[18]

Table 2.2 | Average worm speed observed in this study compared to the literature. N2 refers to wild-type N2 Bristol strain. GCaMP6 refers to strain AML14. All speeds are for worms off food. Table adapted from [7]. *mean ± standard deviation.

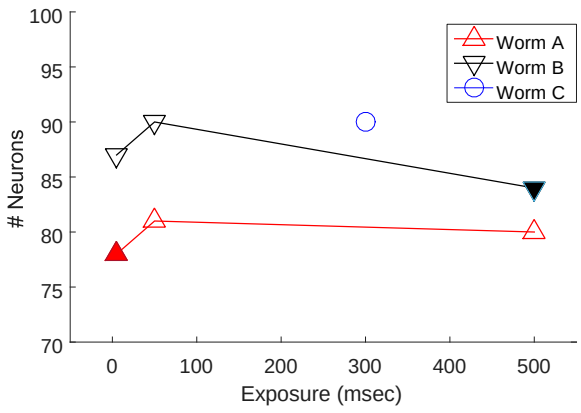


Figure 2.11: Number of neurons observed for immobilized worms under varying exposure times. Immobilized worms (strain AML14) expressing nuclear localized GCaMP6s and RFP were imaged. Neurons were segmented based on RFP fluorescence using the same analysis pipeline as for freely moving worms. The number of observed neurons are shown. Worms A and B are imaged on the whole brain imaging apparatus with the same settings as in freely moving experiments, except that the exposure and z-piezo scan rate was varied accordingly. Filled in marker indicates the last recording for each worm, and thus shows the worm when it is most affected by photobleaching. Worm C was imaged on a commercial spinning disk confocal microscope with smaller *z*-step size (0.25 μm) and a higher NA objectives (60x 1.4 NA). Data presented here is also shown in Supplementary Table S3

Worm	Exposure Time (ms)				Prep	Imaging System
	5	50	300	500		
Worm 1	56				Freely Moving	Whole Brain Imager
Worm 2	77					
Worm 3	68					
Worm 4	57					
Worm A	87	90		84*	Immobilized	
Worm B	78*	81		80		
Worm C			90			Commercial Spinning Disk

Table 2.3: Number of neurons observed in Strain AML14 when imaged under varying conditions. Neurons were segmented based on RFP fluorescence using the same analysis pipeline. Worms 1-4 correspond to recordings in Figure 4 and Supplementary Figure S3. Worms A-C correspond to immobilized recordings shown in Supplementary Figure S2. Starred values indicate the last recording for each worm, and thus shows the worm when it is most affected by photobleaching. Worm C was imaged on a commercial spinning disk confocal microscope with smaller *z*-step size (0.25 μm) and a higher NA objectives (60x 1.4 NA).

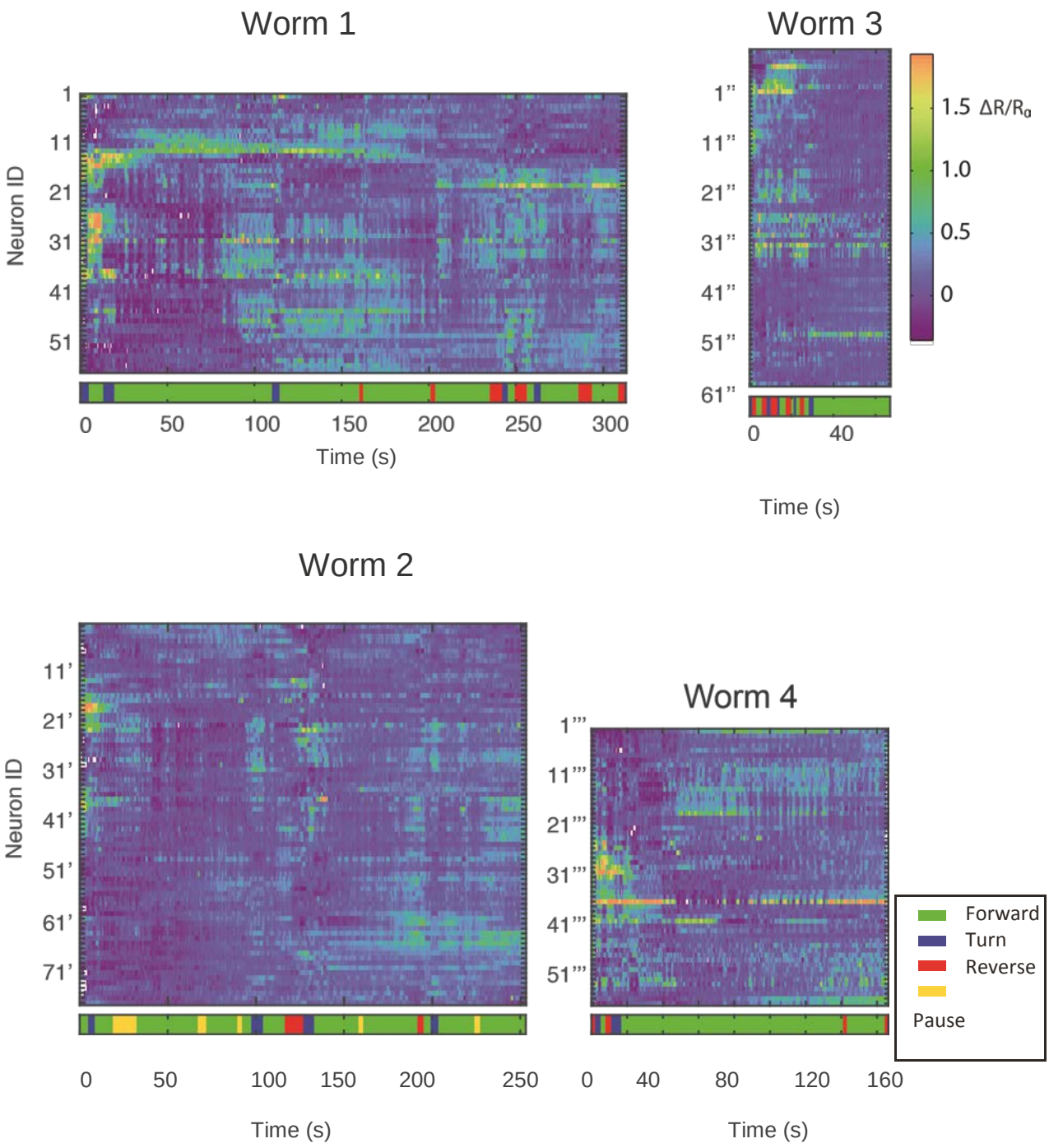


Figure 2.12: Neural activity from four individuals (Worms 1 through 4) with 56, 77, 68, and 57 neurons, respectively, were recorded during behavior. The ratio of GCaMP6s fluorescence to RFP fluorescence for each neuron is plotted. The ratio of fluorescent intensities, R, is represented as the fractional change in $\Delta R/R_0$ where the baseline R_0 is defined for each neuron as the lower 20th percentile value. Neurons are sorted via a hierarchical clustering algorithm. Corresponding correlations are shown in Supplementary Figure S6. Behavioral ethograms are shown. Panels

form Worms 1 and 2 are the same as in Figure 4. Note, neural ID numbers do not indicate correspondence across worms. Occasional white gaps in the data represent instances when the neuron is obscured or transiently leaves the field of view (see Methods in Supplementary Information).

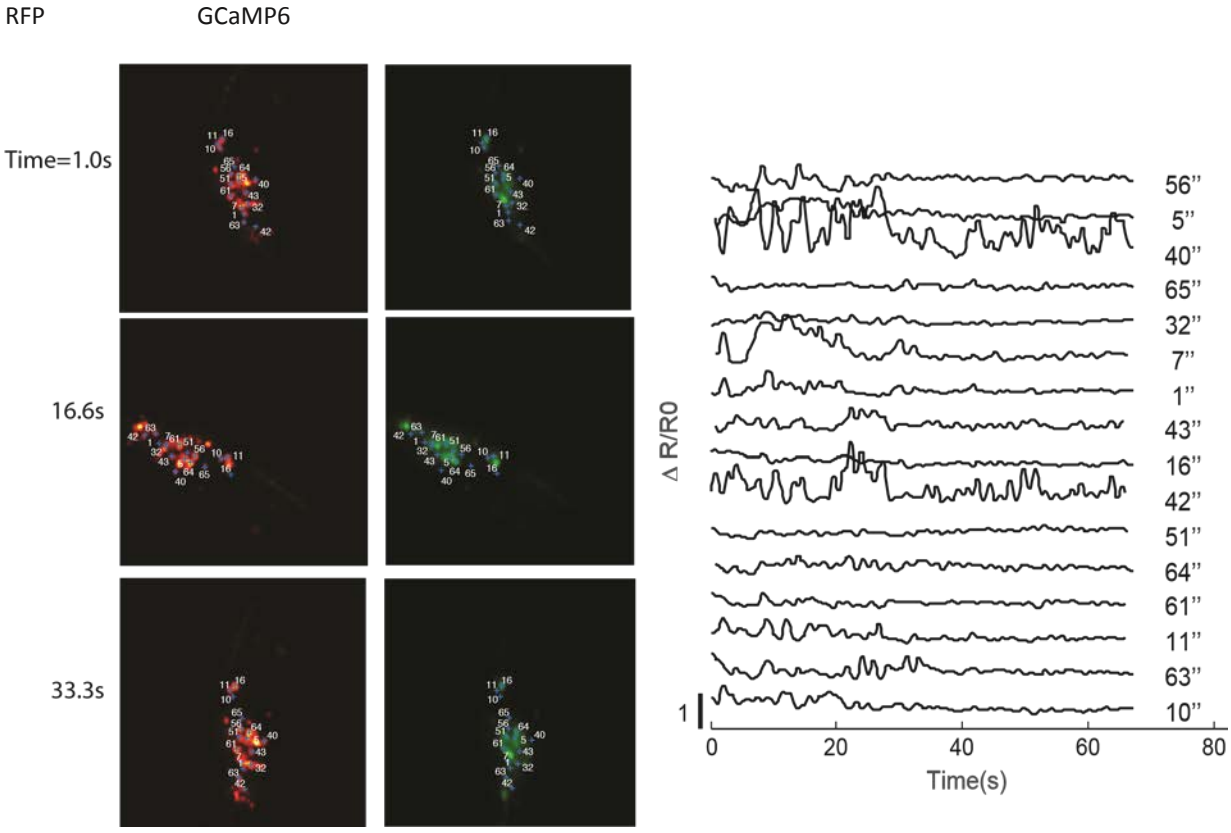


Figure 2.13: Example traces recorded during behavior. Calcium transients from 16 neurons randomly selected from a single horizontal slice of the worm are shown. Each neuron’s position is indicated in simultaneously recorded RFP and GCaMP6s fluorescent images selected at three arbitrary time points. Data is from Worm 3 and corresponds to the recording shown in Supplementary Figure S3.

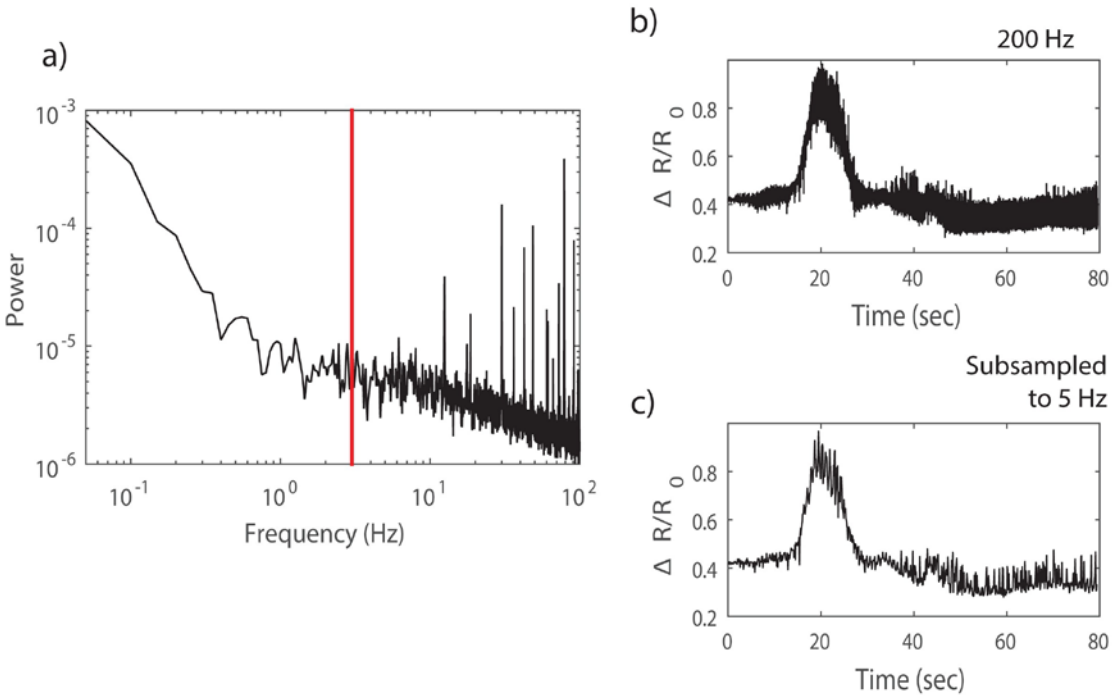


Figure 2.14: To asses the effects of sampling rate, calcium dynamics were recorded at 200 Hz from 33 neurons in a single plane of an immobilized and awake worm (strain AML14). a) Averaged power spectra of GCaMP6s fluorescent intensity from the 33 neurons are shown. Red line indicates the Nyquist frequency of the whole brain imaging system (3 Hz, half the sampling rate). Greater than 99% of the power is located below the Nyquist limit. b) Calcium trace from a single neuron is shown recorded at 200 Hz c) The same trace is subsampled in software to 5 Hz which is even lower than the 6 Hz rate used in freely moving experiments.

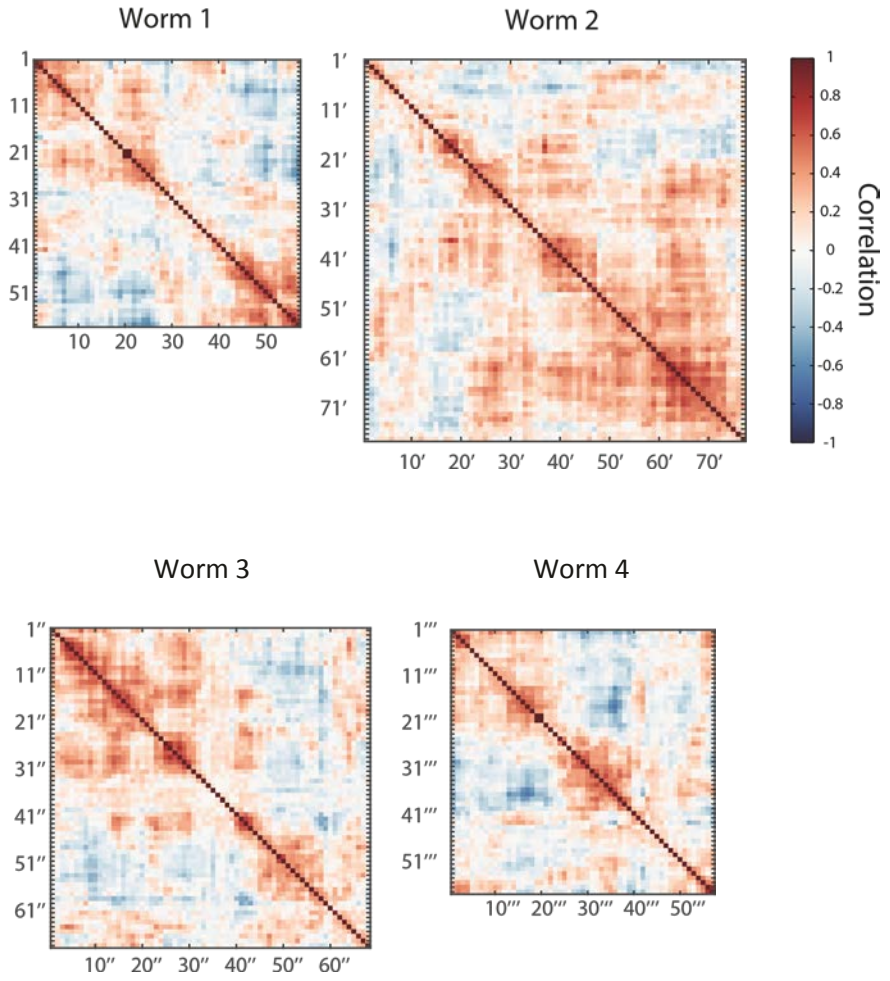


Figure 2.15 Correlations between calcium activity of neurons from all four individual worms are shown. Data corresponds to neural activity shown in Figure 3. Correlation values are hierarchically clustered using a Euclidean distance metric so that neurons with similar activity are organized together. Panels showing Worm 1 and Worm 2 are identical to Figure 5.

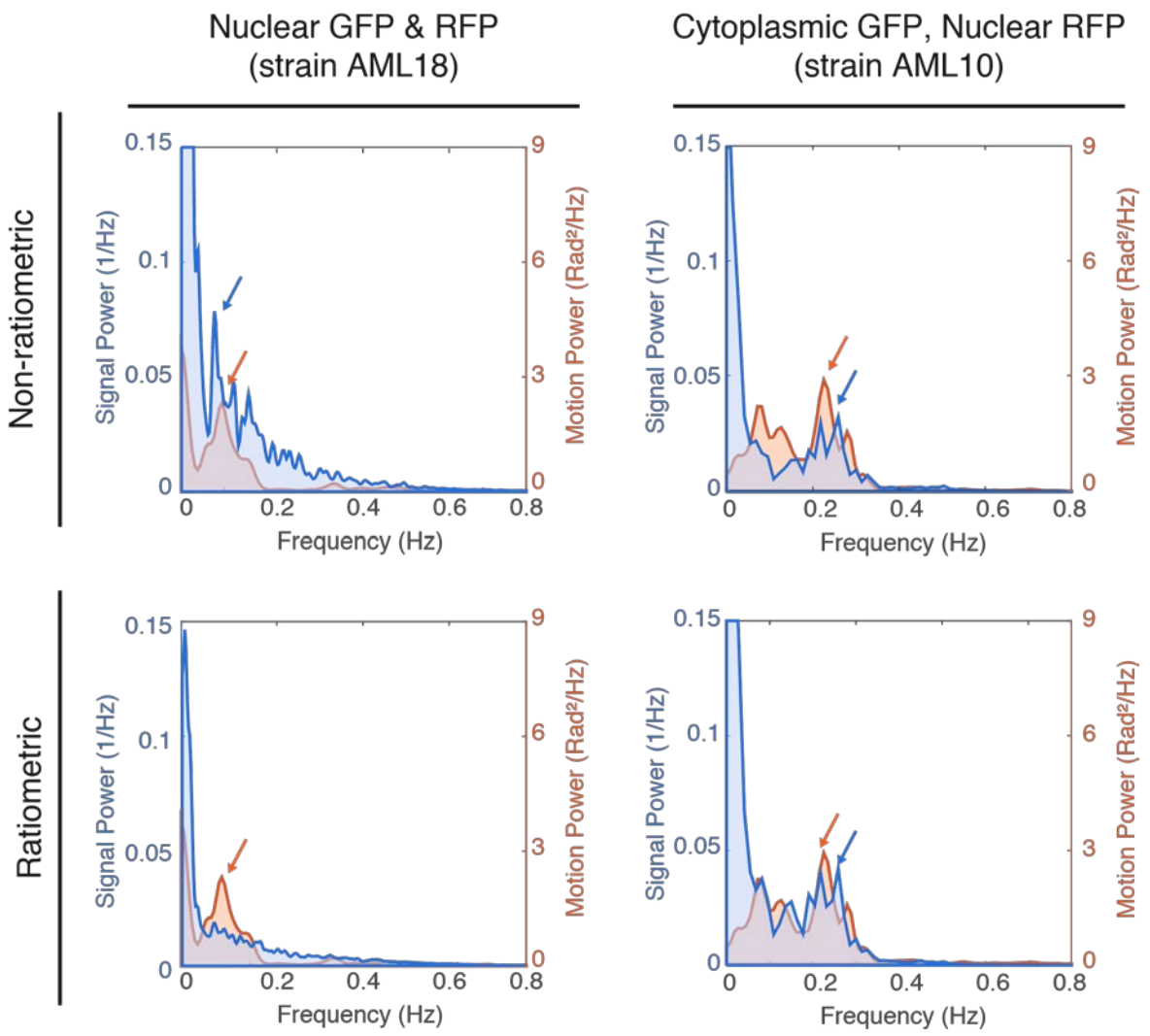


Figure 2.16 Motion artifacts in control worms are shown for different imaging approaches. Two different GFP control strains were compared each under two conditions. Strain AML18 (left column) expresses both GFP and RFP in the nucleus. Strain AML10 (right column) expresses GFP in the cytoplasm and RFP in the nucleus. A worm from each strain was imaged during free locomotion and apparent neural activity was extracted using both a ratiometric (bottom row) and a non-ratiometric approach (top row). The power spectra of apparent neural activity for each case is shown in blue. Because neither GFP nor RFP are calcium sensitive, any apparent activity can be attributed to motion artifact or other noise in the system. The power spectra of the animal's motion is plotted in orange (see methods in Supplementary Text). Arrows indicate peaks in the respective power spectra, presumably caused by animal motion. In every case except for the all-nuclear localized worm measured with ratiometry (bottom left), a peak in the signal power can be observed at the same frequency as the peak in the motion power spectrum. Unless otherwise noted, nuclear localized ratiometric imaging (bottom left) is used throughout the rest of the manuscript.

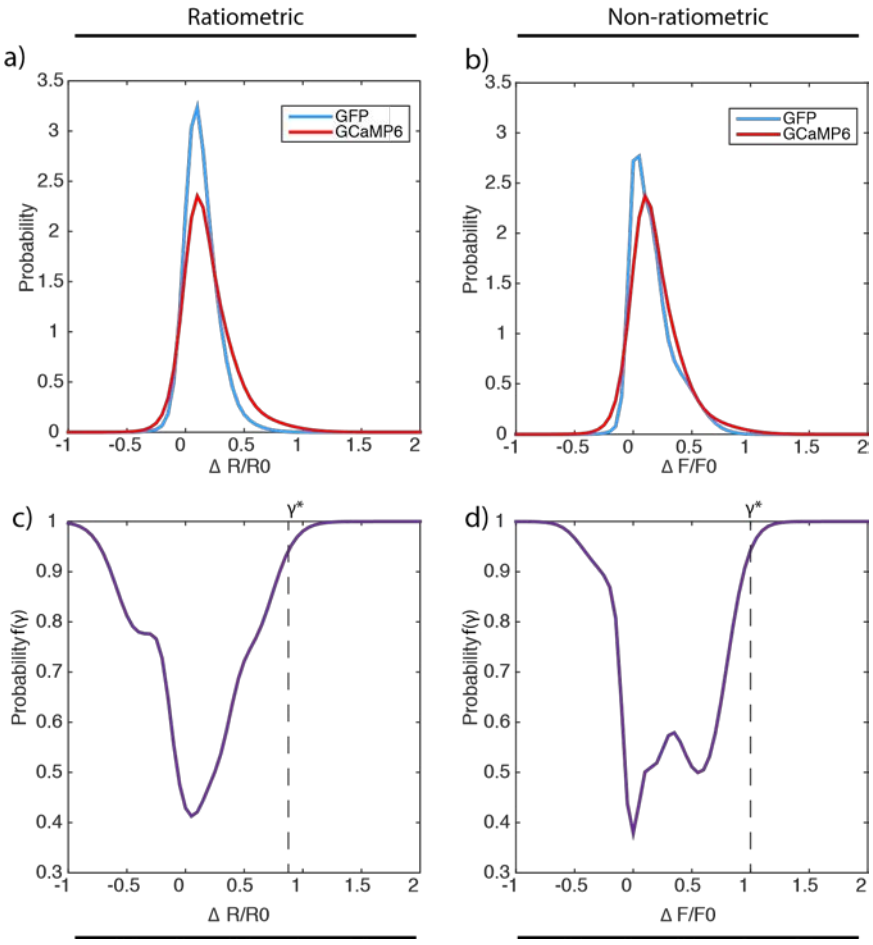


Figure 2.17: A statistical analysis reveals the portion of GCaMP recordings that is unlikely to be attributed to motion or noise, for ratiometric and non-ratiometric approaches. GCaMP recordings (strains AML14) are assumed to contain signal and noise, while GFP control recordings (strain AML18) are assumed to contain only noise. Both strains are all nuclear localized. Note, this population of neurons likely includes silent as well as active neurons. The same GCaMP and GFP recordings are analyzed ratiometrically (left column) as in the rest of the manuscript, and nonratiometrically (right column). a,b) Probability density functions are shown of the distribution of a)$\Delta R/R_0$ or b) $\Delta F/F_0$ values for calcium imaging GCaMP recordings (red) and GFP control recordings (blue). c,d) Probability $f(\gamma)$ that a given neuron-time-value, γ, arose from a GCaMP recording is shown (purple). c) $\Delta R/R_0$ or d) $\Delta F/F_0$ value, γ^*, above which there is 95% likelihood that the value arose from the GCaMP distribution is shown as a dashed line. Subpanel a) is the same as in Figure 7. Integral under the GCaMP probability density function from γ^* to infinity provides an estimate of the fraction of neural-time-point recordings that can be attributed to signal with greater than 95% likelihood, $<N_{signal}i>$, as in Supplementary Table S4.

	Ratiometric ($\Delta R/R_0$)	Non-ratiometric ($\Delta F/F_0$)
$\langle N_{signal} \rangle$	1.6%	0.6%
$\gamma*$	0.85	1.00

Table 2.4 Summary of statistical analysis comparing signals from ratiometric to non-ratiometric imaging approaches for nuclear localized GCaMP and control GFP recordings (strains AML14 and AML18). $\langle N_{signal} \rangle$ is an estimate of the fraction of neural-time-points within GCaMP recordings that can be attributed to signal with greater than 95% likelihood. γ^* is the $\Delta R/R_0$ value or $\Delta F/F_0$ value, respectively, above which the neuron-time-point observation is greater than 95% likely to have arisen from signal, as in Supplementary Figure S8. See methods in Supplementary Information for details. Note, the population of neurons likely includes silent as well as active neurons.

Neuron type	Behavior	No. in FOV	Evidence	Reference
AVB	Forward	2	Calcium Imaging	[43]
VB-type	Forward	1	Calcium Imaging	[42,43]
	Total in FOV	3		
AVA	Reverse	2	Calcium imaging	[18,25,36,41, 42,43]
AVE	Reverse	2	Calcium imaging	[43]
AIB	Reverse	2	Calcium imaging	[25,42]
VA-type	Reverse	1	Calcium imaging	[18,43]
RIM	Reverse	2	Calcium Imaging	[25,42]
	Total in FOV	9		
DD-type	Turning	1	Laser ablation	[23]
RIB	Turning	2	Laser ablation	[45]
SMD	Turning	4	Laser ablation	[45]
RIV	Turning	2	Laser ablation	[45]
	Total in FOV	9		

Table 2.5: Summary of evidence in literature implicating neurons in forward, reverse and turning behavior. The neuron type is listed, as well as the behavior and the number of neurons whose location should be within our imaging field of view (FOV). For example, there are many VA motor neurons, but only one lies within our field of view. For forward and reverse behavior only evidence from calcium imaging studies are shown. For turning behavior the only calcium imaging studies that exist in the literature study only sensory neurons and only in specific sensory contexts[44], [67], so laser ablation studies are included instead. Note, previous evidence suggested that RIM can also exhibit activity correlated with forward motion in some contexts[42] but that during spontaneous behavior its activity correlates with reversals[25].

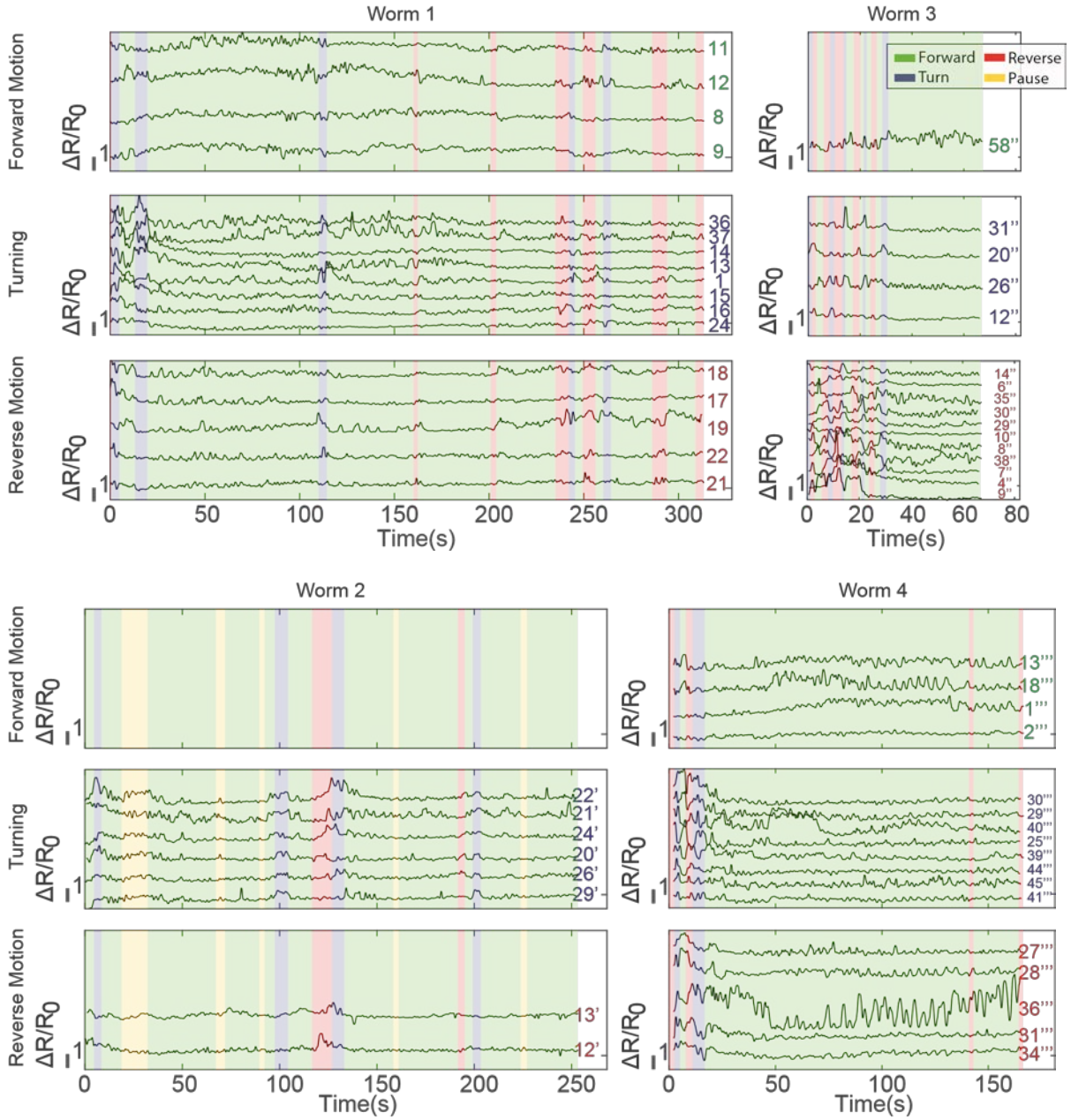


Figure 2.18: All neurons whose activity correlated with either forward, turning or reverse behavior above a significance threshold are shown for all individuals. The significance threshold was calibrated to the noise observed in the GFP control recordings. Vertical scale bar indicates $\Delta R/R_0$ of 1 (100%). Each neuron's ID number is indicated. Note numbers do not indicate correspondence across worms. Panel showing Worm 1 is identical to Figure 8.

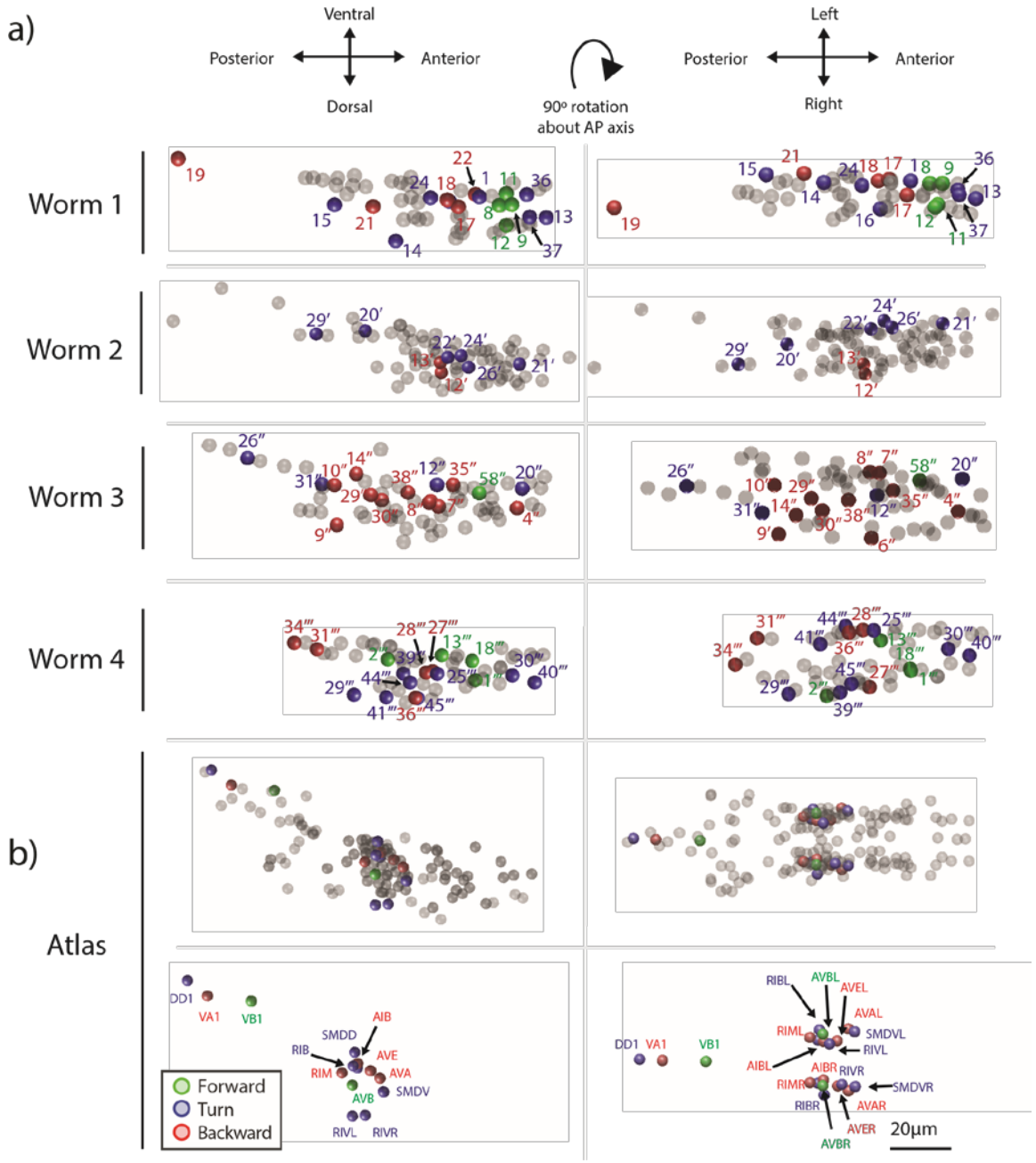


Figure 2.19: The position of recorded neurons for each worm is plotted in 3D and compared to an atlas. The left column shows a dorsal-ventral plane view of the animal, while the right column shows left-right plane view of the animal. a) Neurons whose activity correspond to forward, turning or reverse are colored and labeled with a neuron ID corresponding to Supplementary Figure S3. Remaining neurons are shaded gray. Panel showing Worm 1 is the same as in Figure 9. b) The position of all known neurons are plotted using reference data culled from the WormBase Virtual Worm Project. Neurons that have previously been reported in the literature as implicated in a behavior are colored accordingly (see Supplementary Table S5) and labeled with their neuron name. Colored neurons are shown both in and out of context of all other neurons for clarity.

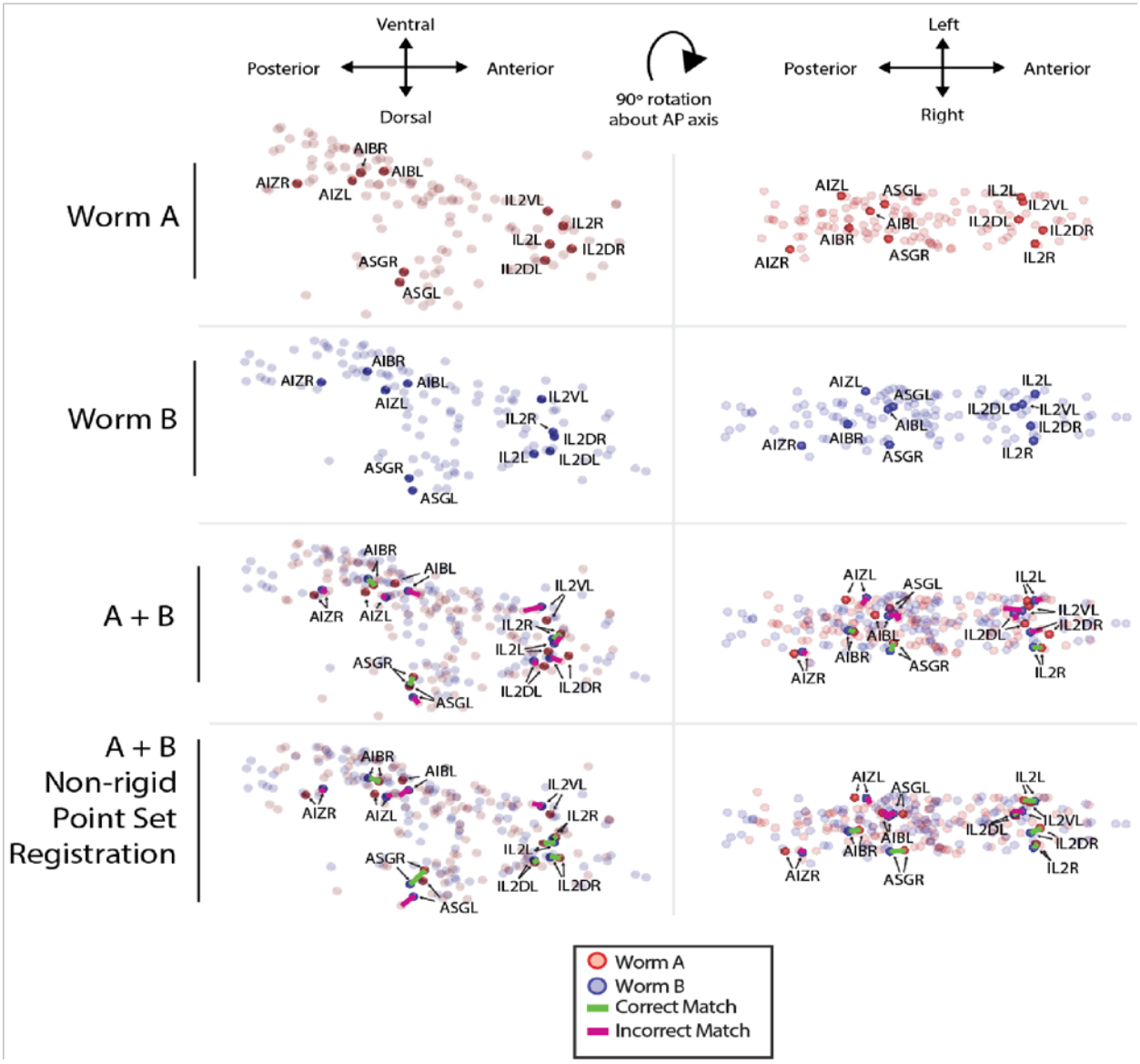


Figure 2.20: Neurons cannot easily be identified across worms based on position information alone. The position of neurons from two similar aged integrated transgenic worms, “A” (red spheres) and “B” (blue spheres), are shown. The left column shows a dorsal-ventral plane view of the animal, while the right column shows left-right plane view of the animal. Both worms were made to express RFP in all neurons, and GFP in a subset of 11 neurons whose identities can be assigned unambiguously by eye (darker spheres, labeled with neuron name). The results of a rigid scaling, rotation and alignment are shown, where closest neurons across worms were paired (“A + B”). Correct matches of the known GFP-labeled neurons are shown in green, while incorrect matches are shown in pink. Only 3 of the 11 pairs of GFP neurons were correctly matched. Seven non-linear warping algorithms were also tested, and the result of the best performing algorithm, a non-rigid point set registration algorithm [4], is shown (“A + B Non-rigid point-set registration”). That algorithm was able to correctly identify 6 of 11 GFP-labeled neurons.

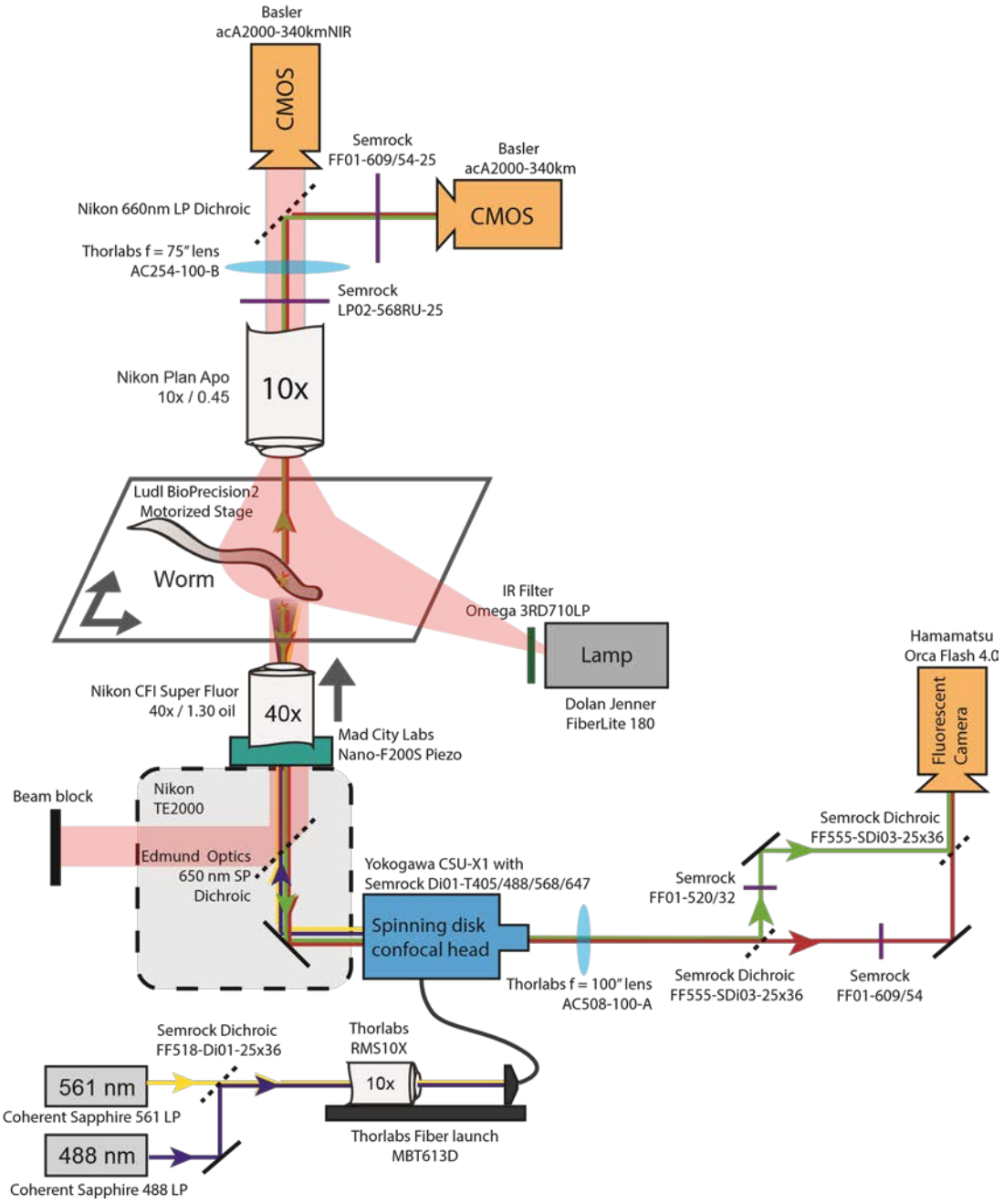


Figure 2.21: A schematic of the optical elements used.

Camera Use	40x Fluorescence	10x Fluorescence	10x Behavior
Brand	Hamamatsu	Basler	
Model	Orca Flash 4.0	acA2000-340km	acA2000-340km-NIR
Sensor	sCMOS	CMOS	
Interface	Camera Link		
Frame Grabber	BitFlow Karbon PCIe x16 10-tap	Active Silicon Firebird PCIe GEN II 8x	
Active Pixels	1200 x 600	1024 x 768	1088 x 1088
Bit Depth	16	10	
Image Scale	3100 px/mm	620 px/mm	620 px/mm
Exposure (ms)	5	2.5	4
Frame Rate (fps)	200	67	42

Table 2.6 Properties and parameters for the three cameras used.

Worm	Orientation
Worm 1	Right
Worm 2	Left
Worm 3	Right
Worm 4	Left

Table 2.7 Orientation of the worms that were imaged. On 2D substrates worms naturally crawl in the dorsal-ventral plane. Right indicates that the worm's right side faced the 40x objective during imaging.

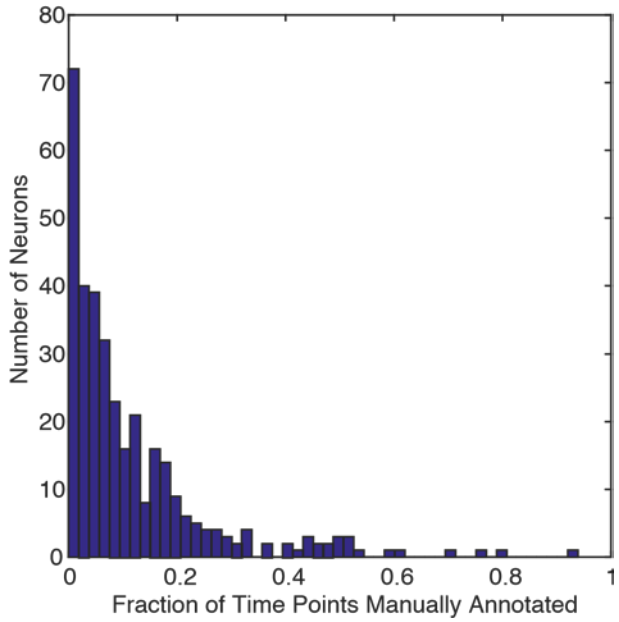


Figure 2.22: Distribution across neurons of the accuracy of the tracker as compared to human for all worms including Worms 1,2,3,4 and the GFP Control worm. All automatically annotated neurons are checked by a human at each time point. Where the automated neural identity tracking algorithm fails the human manually corrects the annotation.

Chapter 3

Automatically tracking neurons in a moving and deforming brain

This chapter was originally published as [78].

Jeffrey P. Nguyen, Ashley N. Linder, George S. Plummer, Joshua W. Shaevitz,and Andrew M. Leifer. Automatically tracking neurons in a moving and deforming brain. PLoS Comput Biol 13(5): e1005517

3.1 Abstract

Advances in optical neuroimaging techniques now allow neural activity to be recorded with cellular resolution in awake and behaving animals. Brain motion in these recordings pose a unique challenge. The location of individual neurons must be tracked in 3D over time to accurately extract single neuron activity traces. Recordings from small invertebrates like *C. elegans* are especially challenging because they undergo very large brain motion and deformation during animal movement. Here we present an automated computer vision pipeline to reliably track populations of neurons with single neuron resolution in the brain of a freely moving *C. elegans* undergoing large motion and deformation. 3D volumetric fluorescent images

of the animal's brain are straightened, aligned and registered, and the locations of neurons in the images are found via segmentation. Each neuron is then assigned an identity using a new time-independent machine-learning approach we call Neuron Registration Vector Encoding. In this approach, non-rigid point-set registration is used to match each segmented neuron in each volume with a set of reference volumes taken from throughout the recording. The way each neuron matches with the references defines a feature vector which is clustered to assign an identity to each neuron in each volume. Finally, thin-plate spline interpolation is used to correct errors in segmentation and check consistency of assigned identities. The Neuron Registration Vector Encoding approach proposed here is uniquely well suited for tracking neurons in brains undergoing large deformations. When applied to whole-brain calcium imaging recordings in freely moving *C. elegans*, this analysis pipeline located 156 neurons for the duration of an 8 minute recording and consistently found more neurons more quickly than manual or semiautomated approaches.

3.2 Introduction

Optical neural imaging has ushered in a new frontier in neuroscience that seeks to understand how neural activity generates animal behavior by recording from large populations of neurons at cellular resolution in awake and behaving animals. Population recordings have now been used to elucidate mechanisms behind zebra finch song production[68], spatial encoding in mice[69], and limb movement in primates[26]. When applied to small transparent organisms, like *Caenorhabditis elegans*[24], *Drosophila*, and zebrafish[33], nearly every neuron in the brain can be recorded, permitting the study of whole brain neural dynamics at cellular resolution.

Methods for segmenting and tracking neurons have struggled to keep up as new imaging technologies now record from more neurons over longer times in environments with greater motion. Accounting for brain motion in particular has become a major challenge, especially in recordings of unrestrained animals. Brains in motion undergo translations and deformations in 3D that make robust tracking of individual neurons very difficult. The problem is compounded in invertebrates like *C. elegans* where the head of the animal is flexible and deforms greatly. If left unaccounted for, brain motion not only prevents tracking of neurons, but it can also introduce artifacts that mask the true neural signal. In this work we propose an automated approach to segment and track neurons in the presence of dramatic brain motion and deformation. Our approach is optimized for calcium imaging in unrestrained *C. elegans*.

Neural activity can be imaged optically with the use of genetically encoded calcium sensitive fluorescent indicators, such as GCaMP6s used in this work[28]. Historically calcium imaging was often conducted in head-fixed or anesthetized animals to avoid challenges involved with imaging moving samples[1], [2], [24]. Recently, however, whole-brain imaging was demonstrated in freely behaving *C. elegans*[70], [71]. *C. elegans* are a small transparent nematode, approximately 1mm in length, with a compact nervous system of only 302 neurons. About half of the neurons are located in the animal's head, which we refer to as its brain.

Analyzing fluorescent images of moving and deforming brains requires algorithms to detect neurons across time and extract fluorescent signals in 3D. Automated methods exist for segmenting and tracking fluorescently labeled cells during *C. elegans* embryogenesis[72], and semi-automated methods are even able to track specific cells during embryo motion[73], but to our knowledge these methods are not suitable for tracking neurons in adults. Generally, several strategies exist for tracking neurons in volumetric recordings. One approach is to find

correspondences between neuron positions in consecutive time points, for example, by applying a distance minimization, and then stitching these correspondences for each time step are less than the distance between neighboring neurons, and that the neurons remain identifiable at all times. If these requirements break down, even for only a few time points, errors can quickly accumulate. Other common methods, like independent component analysis (ICA)[74] are also exquisitely sensitive to motion and as a result they have not been successfully applied to recordings with large brain deformations.

Large inter-volume motion arises when the recorded image volume acquisition rate is too low compared to animal motion. Unfortunately, large inter-volume brain motion is likely to be a prominent feature of whole-brain recordings of moving brains for the foreseeable future. In all modern imaging approaches there is a fundamental tradeoff between the following attributes: acquisition rate (temporal resolution), spatial resolution, signal to noise, and the spatial extent of the recording. As recordings seek to capture larger brain regions at single cell resolution, they necessarily compromise on temporal resolution. For example, whole brain imaging in freely moving *C. elegans* has only been demonstrated at slow acquisition rates because of the requirements to scan the entire brain volume and expose each slice for sufficiently long time. At these rates, a significant amount of motion is present between image planes within a single brain volume. Similarly, large brain motions also remain between sequential volumes. Neurons can move the entire width of the worm's head between sequential volumes when recording at 6 brain-volumes per second, as in [70]. In addition to motion, the brain also bends and deforms as it moves. Such changes to the brain's conformation greatly alter the pattern of neuron positions making constellations of neurons difficult to compare across time.

To track neurons in the presence of this motion, previous work that measured neural activity in freely moving *C. elegans* utilized semi-automated methods that required human proof reading or manual annotation to validate each and every neuron-time point[70], [71]. This level of manual annotation becomes impractical as the length of recordings and the number of neurons increases. For example, 10 minutes of recorded neural activity from[70] [70], had over 360,000 neuron time points and required over 200 person-hours of proofreading and manual annotation. Here, we introduce a new time-independent algorithm that uses machine learning to automatically segment and track all neurons in the head of a freely moving animal without the need for manual annotation or proofreading. We call this technique Neuron Registration Vector Encoding, and we use it to extract neural signals in unrestrained *C. elegans* expressing the calcium indicator GCaMP6s and the fluorescent label RFP.

3.3 Results

3.3.1 Overview of neuron tracking analysis

We introduce a method to track over 100 neurons in the brain of a freely moving *C. elegans*. The analysis pipeline is made of five modules and an overview is shown in Fig 1. The first three modules, “Centerline Detection,” “Straightening” and “Segmentation,” collectively assemble the individually recorded planes into a sequence of 3D volumes and identify each neuron’s location in each volume. The next two modules, “Registration Vector Construction” and “Clustering,” form the core of the method and represent a significant advance over previous approaches. Collectively, these two modules are called “Neuron Registration Vector Encoding.” The “Registration Vector Construction” module leverages information from across the entire recording in a time-independent way to generate feature vectors that characterize every neuron at

every time point in relation to a repertoire of brain confirmations. The “Clustering” module then clusters these feature vectors to assign a consistent identity to each neuron across the entire recording. A final module corrects for errors that can arise from segmentation or assignment. The implementation and results of this approach are described below.

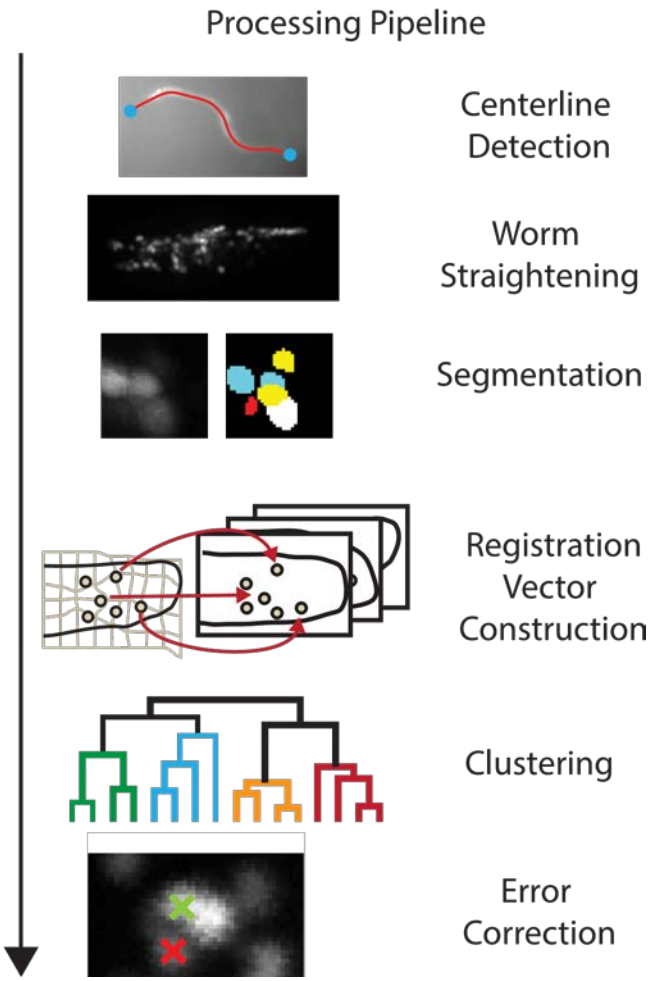


Figure 3.1 Schematic of analysis pipeline to segment and track neurons through time and extract their neural activity in a deforming brain. Neurons are labeled with calcium insensitive red fluorescent proteins, RFP, and calcium sensitive green fluorescent proteins, GCaMP. Videos of the animal’s behavior and volumetric fluorescent images of the animal’s brain serve as input to the pipeline. The algorithm detects all neurons in the head and produces tracks of the neural activity across time as the animal moves.

3.3.2 Recording of whole-brain calcium activity and body posture in moving animal

Worms expressing the calcium indicator GCaMP6s and a calcium-insensitive fluorescent protein RFP in the nuclei of all neurons were imaged during unrestrained behavior in a custom 3D tracking microscope, as described in [70]. Only signals close to the cell nuclei are measured. Two recordings are presented in this work: a new 8 minute recording of an animal of strain AML32 and a previously reported 4 minute recording of strain AML14 first described in [70]. The signal of interest in both recordings is the green fluorescence intensity from GCaMP6s in each neuron. Red fluorescence from the RFP protein serves as a reference for locating and

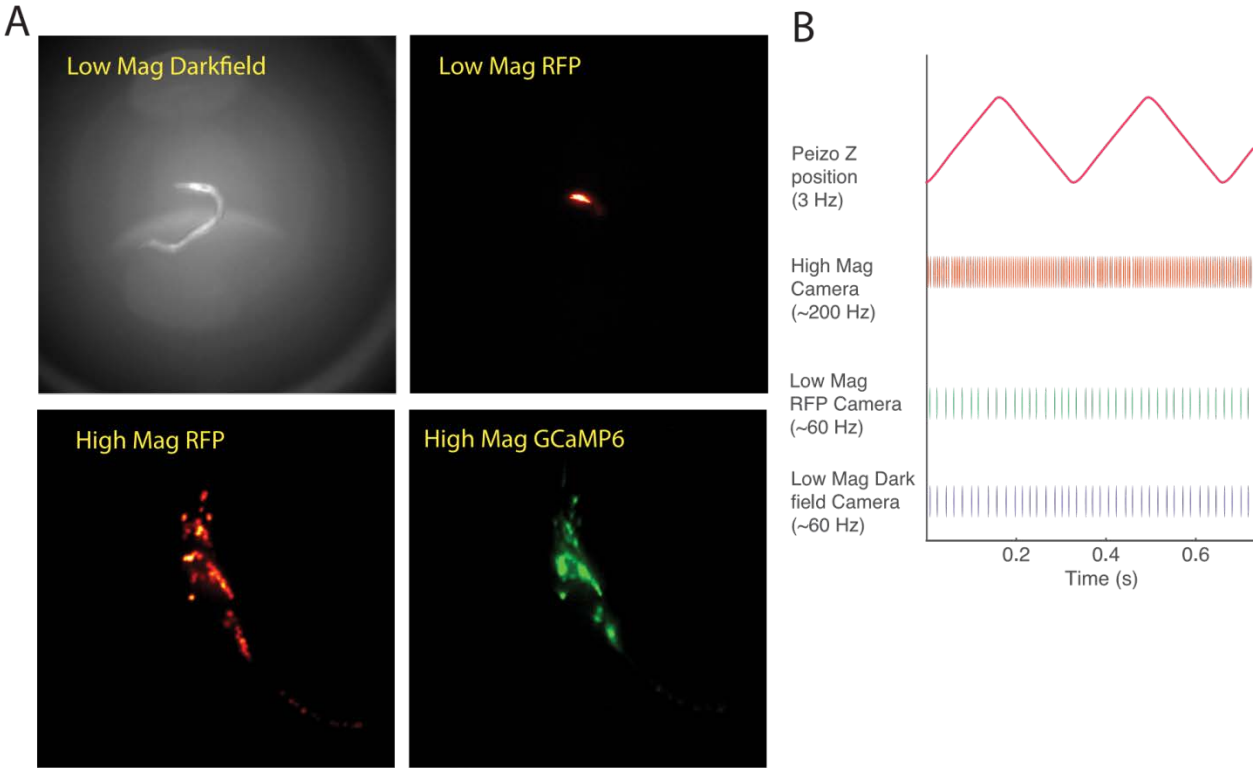


Figure 3.2. Input to the pipeline. (A) Example images from all four video feeds from our imaging system. Both scale bars are 100µm. Fluorescent images are shown with false coloring. (B)A schematic illustrating the timings from all the devices that run in open loop in our imaging setup. The camera that collects high magnification images captures at 200Hz. The two low magnification images capture at 60Hz, and the focal plane moves up and down in a 3 Hz triangle wave. The cameras are synchronized post-hoc using light flashes and each image is assigned a timestamp on a common timeline.

tracking the neurons. The microscope provides four raw image streams that serve as inputs for our neural tracking pipeline, seen in Fig 2A. They are: (1) low-magnification dark-field images of the animal's body posture (2) low-magnification fluorescent images of the animal's brain (3) high-magnification green fluorescent images of single optical slices of the brain showing GCaMP6s activity and (4) high-magnification red fluorescent images of single optical slices of the brain showing the location of RFP. The animal's brain is kept centered in the field of view by realtime feedback loops that adjust a motorized stage to compensate for the animal's crawling. To acquire volumetric information, the high magnification imaging plane scans back and forth along the axial dimension, z, at 3 Hz as shown in Fig 2B, acquiring roughly 33 optical slices per volume, sequentially, for 6 brain-volumes per second. The animal's continuous motion causes each volume to be arbitrarily sheared. Although the image streams operate at different volume acquisition rates and on different clocks, they are later synchronized by flashes of light that are simultaneously visible to all cameras. Each image in each stream is given a timestamp on a common timeline for analysis. Each of the four imaging streams are spatially aligned to each other in software using affine transformations found by imaging fluorescent beads. An example of the high magnification RFP recording is shown in S1 Movie.

3.3.3 Centerline detection and gross brain alignment

The animal's posture contains information about the brain's orientation and about any deformations arising from the animal's side-to-side head swings. The first step of the pipeline is to extract the centerline that describes the animal's posture. Centerline detection in C. elegans is an active field of research. Most algorithms use intensity thresholds to detect the worm's body and then use binary image operations to extract a centerline [16–18]. Here we use an open active

contour approach [19, 20] to extract the centerline from dark field images with modifications to account for cases when the worm's body crosses over itself as occurs during so-called "Omega Turns." In principle any method, automated or otherwise, that detects the centerlines should be sufficient. At rare times where the worm is coiled and the head position and orientation cannot be determined automatically, the head and the tail of the worm are manually identified.

The animal's centerline allows us to correct for gross changes in the worm's position, orientation, and conformation (Fig 3a). We use the centerlines determined by the low magnification behavior images to straighten the high magnification images of the worm's brain. An affine transform must be applied to the centerline coordinates to transform them from the dark field coordinate system into the coordinate system of the high magnification images. Each

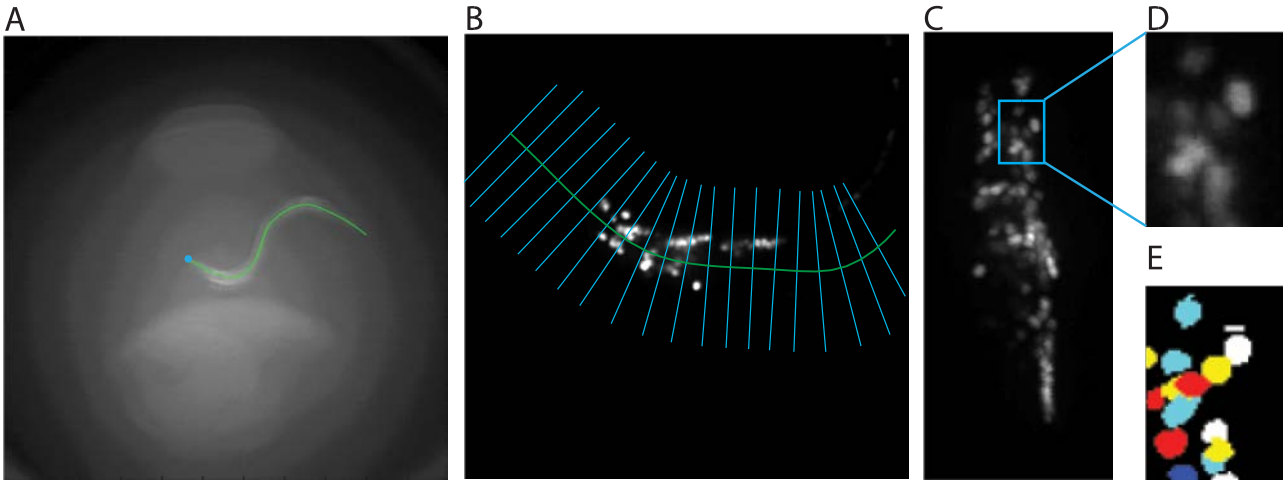


Figure 3.3 (A) Centerlines are detected from the low magnification dark field images. The centerline is shown in green and the tip of the worm's head is indicated by a blue dot. (B) The centerline found from the low magnification image is overlaid on the high magnification RFP images. The lines normal to the centerline, shown in blue, are used to straighten the image. All scale bars are 100 μm. (C) A maximum intensity projection of the straightened volume is shown. Individual neuronal nuclei are shown (D) before and (E) after segmentation.

image slice of the worm brain is straightened independently to account for motion within a single volume. The behavior images are taken at a lower acquisition rate than the high magnification brain images, so a linear interpolation is used to obtain a centerline for each slice of the brain volume. In each slice, we find the tangent and normal vectors at every point of the centerline (Fig 3b). The points are interpolated with a single pixel spacing along the centerline to preserve the resolution of the image. The image intensities along each of the normal directions are interpolated and the slices are stacked to produce a straightened image in each slice (Fig 3c). In the new coordinate system, the orientation of the animal is fixed and the gross deformations from the worm's bending are suppressed. More subtle motion and deformation, however, remains. We further reduce shearing between slices using standard video stabilization techniques. Specifically, bright-intensity peaks in the images are tracked between neighboring image slices. The coordinates of these peaks are used to calculate the affine transformations between neighboring slices of the volume using least squares. All slices are registered to the middle slice by applying these transformations sequentially throughout the volume. Each slice would undergo transformations for every slice in between it and the middle slice to correct shear throughout the volume. A final rigid translation is required to align each volume to the first volume of the recording. The translations are found by finding an offset that maximizes the cross-correlation between each volume and the initial volume.

A video of straightening is shown in S1 Movie. Straightened images are used for the remaining steps of the analysis pipeline. Only the final measurement of fluorescence intensity is performed in the original unstraightened coordinated system.

3.3.4 Segmentation

Before neuron identities can be matched across time, we must first segment the individual neurons within a volume to recovers each neuron's size, location, and brightness (Fig 3d and 3e). Many algorithms have been developed to segment neurons in a dense region[75], [76]. We segment the neurons by finding volumes of curvature in fluorescence intensity in the straigthened volumes. After an initial smoothing, we compute the 3D Hessian matrix at each point in space and threshold for points where all of the three eigenvalues of the Hessian matrix are negative. This process selects for regions around intensity peaks in three dimensions. In order to further divide regions into objects that are more likely to represent neurons, we use a watershed separation on the distance transform of the thresholded image. The distance transform is found by replacing each thresholded pixel with the Euclidean distance between it and the closest zero pixel in the thresholded image. This approach is sufficient to segment most neurons. Occasionally neurons are missed or two neurons are incorrectly merged together. These occasional errors are corrected automatically later in the pipeline.

3.3.5 Neuron registration vector construction

Extracting neural signals requires the ability to match neurons found at different time points. Even after gross alignment and straightening, neurons in our images are still subject to local nonlinear deformations and there is significant movement of neurons between volumes. This remaining motion and deformation is clearly visible, for example, in S1 Movie. Rather than tracking neurons sequentially in time, the neurons in each volume are characterized based on how they match to neurons in a set of reference volumes. Our algorithm compares constellations of neurons in one volume to unannotated reference volumes and assigns correspondences or

"matches" between the neurons in the sample and each reference volume. We modified a point-set registration algorithm developed by Jian and Vemuri to do this (Fig 4a). The registration algorithm represents two point-sets, a sample point-set denoted by X = {xi} and a reference point-set indicated by R = {ri}, as Gaussian mixtures and then attempts to register them by deforming space to minimize the distance between the two mixtures. In their implementation, each point is modeled by a 3D Gaussian with uniform covariance. Since we are matching images of neurons rather than just points, we can use the additional information from the size and brightness of each neuron. We add this information to the representation of each neuron by adjusting the amplitude and standard deviation of the Gaussians. The Gaussian mixture representation of an image is given by,

$$f(\xi, \boldsymbol{X}) = \sum_i A_i exp(-\frac{\left|\left|\xi - x_i\right|\right|^2}{2(\lambda\sigma_i)^2}) \quad (1)$$

where Ai, xi, and σi are the amplitude, mean, and standard deviation of the i-th Gaussian. These parameters are derived from the brightness, centroid, and size of the segmented neuron, while ξ is the 3D spatial coordinate. A scale factor λ is added to the standard deviation to scale the size of each Gaussian. This will be used later during gradient descent. The sample constellation of neurons is then represented by the Gaussian mixture $f(\boldsymbol{\xi}, \mathbf{X})$. Similarly, the reference constellation's own neurons are represented as a $f(\boldsymbol{\xi}, \mathbf{R})$.

To match a sample constellation of neurons **X** with a reference constellation of neurons **R**, we use the non rigid transformation *u*: IR^3 7! IR^3. The transformation maps **X** to *u*[**X**] such that the L_2 distance between $f(\boldsymbol{\xi}, u[\mathbf{X}])$ and $f(\boldsymbol{\xi}, \mathbf{R})$ is minimized with some constraint on the amount of deformation. This can be written as an energy minimization problem, with the energy of the transformation, $E(u)$, written as

$$E(u) = \int [f(\xi, u[\boldsymbol{X}]) - f(\xi, R)]^2 d\xi + E_{Deformation}(u) \quad (2)$$

Note that the point-sets **X** and **R** are allowed to have different numbers of points. We model the deformations as a thin-plate spline (TPS). The TPS transformation equations and resulting form of $E_{\text{Deformation}}(u)$ are shown in the methods. The minimization of E is found by gradient descent. Working with Gaussian mixtures as opposed to the original images allows us to model the deformations and analytically compute the gradients of Eq 2 making gradient descent more efficient. The gradient descent approach used here is similar to that outlined by Jian and Vemuri[61]. Since the energy landscape has many local minima, we initially chose a large scale factor, λ, to increase the size of each Gaussian and smooth over smaller features. Gradient descent is iterated multiple times with λ decreasing multiple times. After the transformation, sample points are matched to reference points by minimizing distances between assigned pairs using an algorithm from [77] . The matching is not greedy, and neurons in the sample that are far from any neurons in the reference are not matched. A neuron at $\mathbf{x}_i$ is assigned a match v_i to indicate which neuron in the set **R** it was matched to. For example if $\mathbf{x}_i$ matched with $\mathbf{r}_j$ when **X** is registered to **R**, then $v_i = j$. If $\mathbf{x}_i$ has no match in **R**, then $v_i =$;.

The modified non-rigid point-set registration algorithm described above allows us to compare one constellation of neurons to another. In principle, neuron tracking could be achieved by registering the constellation of neurons at each time-volume to a single common reference. That approach is susceptible to failures in non-rigid point-set registration. Non-rigid point-set registration works well when the conformation of the animal in the sample and the reference are similar, but it is unreliable when there are large deformations between the sample and the reference, as happens with some regularity in our recordings. In addition, this approach is especially sensitive to any errors in segmentation, especially in the reference. An alternative approach would be to sequentially register neurons in each time volume to the next time-volume.

This approach, however, accumulates even small errors and quickly becomes unreliable. Instead of either of those approaches, we use registration to compare the constellation of neurons at each time volume to a set of reference time-volumes that span a representative space of brain conformations (Fig 4b), as described below.

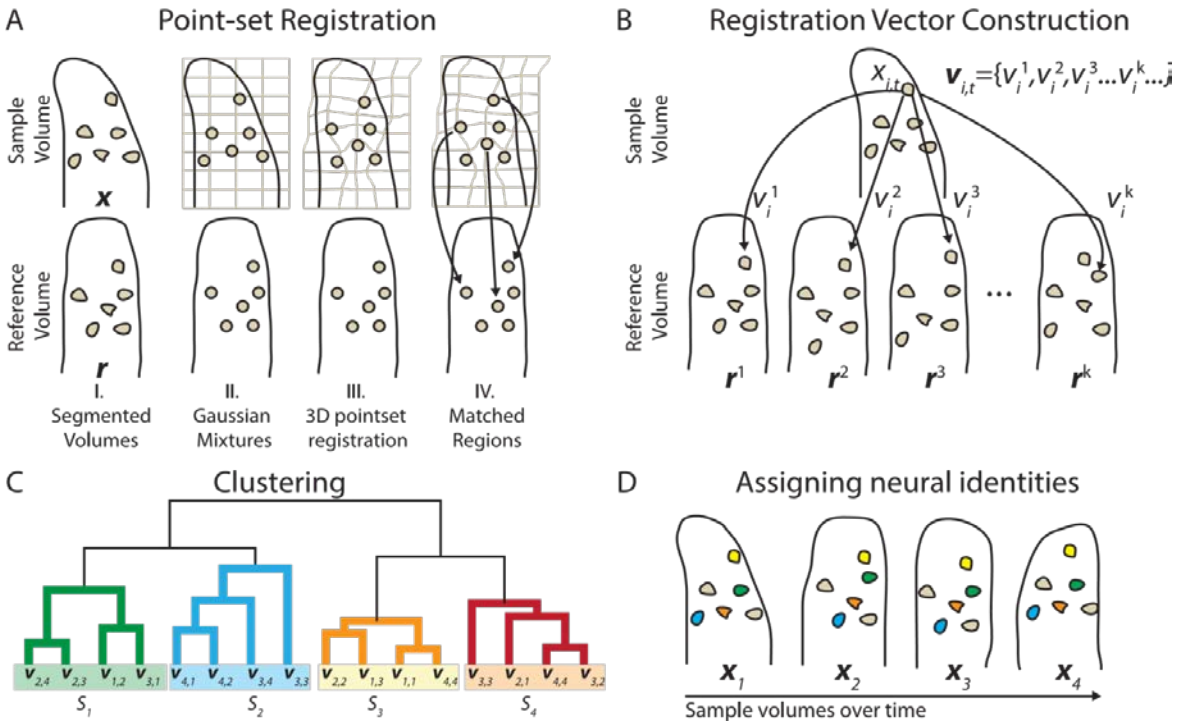


Figure 3.4 **Schematic of Neuron Registration Vector Encoding.** (A) The registration between a sample volume and a single reference volume is done in several steps. I. The image is segmented into regions corresponding to each of the neurons. II. The image is represented as a Gaussian mixture, with a single Gaussian for each segmented region. The amplitude and the standard deviation of the Gaussians are derived from the brightness and the size of the segmented regions. III. Non-rigid point-set registration is then used to deform the sample points to best overlap the reference point-set. IV. Neurons from the sample and the reference point-sets are paired by minimizing distances between neurons. (B) Neuron registration vectors are constructed by assigning a feature vector $\mathbf{v}_{i,t}$ to each neuron $x_{i,t}$ in a sample volume $\mathbf{x}_t$ by performing the registration between the sample volume and a set of 300 reference volumes, each denoted by $\mathbf{r}^k$. Each registration of the neuron results in a neuron match, v_i^k, and the set of matches becomes the feature vector $\mathbf{v}_{i,t}$. (C) Vectors from all neuron-times are clustered into similar groups in a two step process: Hierarchical clustering (illustrated in the figure) is performed on a subset of neurons to define clusters, each of which is given a label S_n. Then each feature vector $\mathbf{v}_{i,t}$ is assigned to a cluster based on a distance metric (not illustrated). (D) The clustering of the feature vectors shown in (C) assigns an identity to each of the neurons in every volume. This allows us to track the neurons across different volumes of the recording.

The constellation of neurons at a particular time in our recording is given by $\mathbf{X}_t$, and the position of the i-th neuron at time t is denoted by $\mathbf{x}_{i,t}$. We select a set of K reference constellations, each from a different time volume $\mathbf{X}_t$ in our recording, so as to achieve a representative sampling of the many different possible brain conformations the animal can attain. These K reference volumes are denoted by $\{\mathbf{R}^1, \mathbf{R}^2, \mathbf{R}^3,...,\mathbf{R}^K\}$. We use 300 volumes spaced evenly through time as our reference constellations. Each $\mathbf{X}_t$ is separately matched with each of the references, and each neuron in the sample, $\mathbf{x}_{i,t}$, gets a set of matches $\mathbf{v}_{i;t}$ ¼ f$v_i^1{}_{;t}$; $v_i^2{}_{;t}$; $v_i^3{}_{;t}$;::$v_i^K{}_{;t}$g, one match for each of the K references. This set of matches is a feature vector which we call a Neuron Registration Vector. It describes the neuron's location in relation to its neighbors when compared with the set of references. This vector can be used to identify neurons across different times.

We find that 300 reference volumes creates feature vectors that are sufficiently robust to identify neurons in our recordings. What determines the optimal number of reference volumes? As long as the reference volumes contain a representative sample of the space of brain conformation occupied during our recordings, the number of reference volumes needed to create a robust feature vector depends only on the size of this conformation space. Because the conformation space of a real brain in physiological conditions is finite, there exists some number of reference volumes beyond which adding more reference volumes provides no additional information. Crucially, the worm brain seems to explore this finite conformation space quickly relative to the time scales of our recordings. As a result, the number of required reference volumes should not depend on recording length, at least for the minutes-long timescales that we consider here.

3.3.6 Clustering registration vectors

The neuron registration vector provides information about that neuron's position relative to its neighbors, and how that relative position compares with many other reference volumes. A neuron with a particular identity will match similarly to the set of reference volumes and thus that neuron will have similar neuron registration vectors over time. Clustering similar registration vectors allows for the identification of that particular neuron across time (Fig 4c and 4d).

To illustrate the motivation for clustering, consider a neuron with identity *s* that is found at different times in two sample constellations $\boldsymbol{X}_1$ and $\boldsymbol{X}_2$. When $\boldsymbol{X}_1$ and $\boldsymbol{X}_2$ have similar deformations, the neuron *s* from both constellations will be assigned the same set of matches when registered to the set of reference constellations, and as a result the corresponding neuron registration vectors $\mathbf{v}_1$ and $\mathbf{v}_2$ will be identical. This is true even if the registration algorithm itself fails to correctly match neuron *s* in the sample to its true neuron *s* in the reference. As the deformations separating $\boldsymbol{X}_1$ and $\boldsymbol{X}_2$ become larger, the distance between the feature vectors $\mathbf{v}_1$ and $\mathbf{v}_2$ also becomes larger. This is because the two samples will be matched to different neurons in some of the reference volumes as each sample is more likely to register poorly with references that are far from it in the space of deformations.

Crucially, the reference volumes consist of instances of the animal in many different deformation states. So while errors in registering some samples will exist for certain references, they do not persist across all references, and thus do not effect the entire feature vector. For the biologically relevant deformations that we observe, the distance between $\mathbf{v}_1$ and $\mathbf{v}_2$ will be smaller if both are derived from neuron *s* than compared to the distance between $\mathbf{v}_1$ and $\mathbf{v}_2$ if they

were derived from *s* and another neuron. We can therefore cluster the feature vectors to produce groups that consist of the same neuron found at many different time points.

The goal of clustering is to assign each neuron at each volume to a cluster representing that neuron's identity. Clustering is performed on the list of neuron registration vectors from all neurons at all times, $\{\mathbf{v}_{i,t}\}$. Each match in the vector, $v_i^k{}_{;t}$, is represented as a binary vector of 0s with a 1 at the $\mathbf{v}^k{}_i^{\text{th}}$ position. The size of the vector is equal to the number of neurons in $\mathbf{R}^k$. The feature vector $\{\mathbf{v}_{i,t}\}$ is the concatenation of all of the binary vectors from all matches to the *K* reference constellations.

For computational efficiency, a two-step process was used to perform the clustering: First agglomerative hierarchical clustering was used on the neurons from an initial subset of volumes to define the clusters. Next, neurons from all volumes at all times were assigned to the nearest cluster as defined by correlation distance to the clusters' center of mass. Assignments were made in such a way so as to ensure that a given cluster is assigned to at most one neuron per volume. Details of this clustering approach are described in the methods. Each cluster is given a label $\{S_1, S_2, S_3,...\}$ which uniquely identifies a single neuron over time, and each neuron at each time $\mathbf{x}_{i,t}$ is given an identifier $s_{i,t}$ corresponding to the cluster to which that neuron-time belongs. Neurons that are not classified into one of these clusters are removed because they are likely artifactual or represent a neuron that is segmented too poorly for inclusion.

3.3.7 Correcting errors in tracking and segmentation

Neuron Registration Vector Encoding successfully identifies segmented neurons consistently across time. A transient segmentation error, however, would necessarily lead to missing or misidentified neurons. To identify and correct for missing and misidentified neurons,

we check each neuron's locations and fill in missing neurons using a consensus comparison and interpolation in a TPS deformed space. For each neuron identifier s and time t^*, we use all other point-sets, $\{\mathbf{X}_t\}$ to guess what that neuron's location might be. This is done by finding the TPS transformation, $u_{t\to t^*}$: $\mathbf{X}_t \to \mathbf{X}_{t^*}$, that maps the identified points from $\mathbf{X}_t$ to the corresponding points in $\mathbf{X}_{t^*}$ excluding the point s. Since the correspondences between neurons has already been determined, , $u_{t\to t^*}$ can be found by solving for the parameters from the TPS equation (see methods). The position estimate is then given , $u_{t\to t^*}[\mathbf{x}_{i,t}]$ with i selected such that $s_{i,t} = s$. This results in a set of points representing the set of predicted locations of the neuron at time t^* as inferred from the other volumes. When a neuron identifier is missing for a given time, the position of that neuron s is inferred by consensus. Namely, correct location is deemed to be the centroid of the set of inferred locations weighted by the underlying image intensity. This weighted centroid is also used if the current identified location of the neuron s has a distance greater than 3 standard deviations away from the centroid of the set of locations inferred from the other volumes, implying that an error may have occurred in that neuron's classification. This is shown in Fig 5, where neuron 111 is correctly identified in volume 735, but the the label for neuron 111 is incorrectly located in volume 736. In that case the weighted centroid from consensus voting was used.

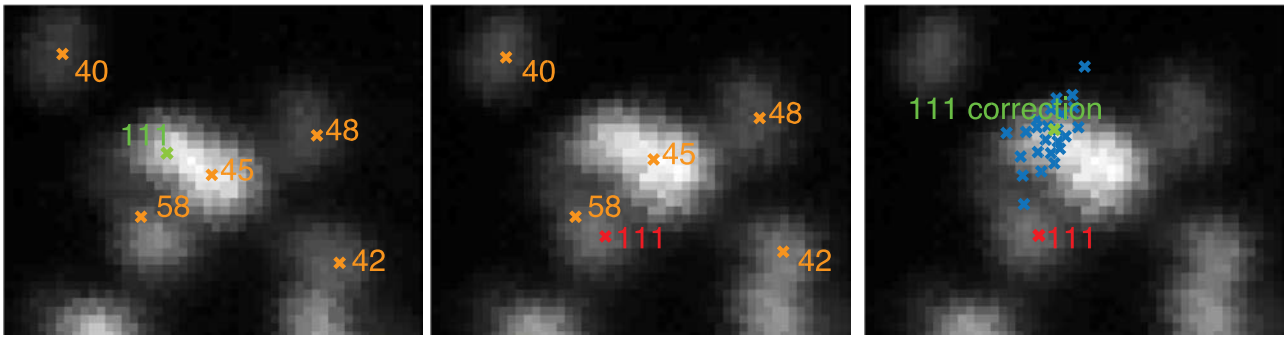


Figure 3.5 **Example of consensus voting to correct a misidentified neuron.** In volume 735, neuron #111 is found successfully and is indicated in green. In volume 736, however, the neuron is misidentified, shown in red. During the correction phase, all other time points vote for what the position of neuron #111 should based on a thin-plate spline deformation. A sample of votes are shown (blue 'x'). Since the initial estimate of the position is far from the majority of consensus votes, a corrected position is assigned to be the centroid of the votes weighted by image intensity. This process is repeated to correct any errors for every neuron at every time.

3.3.8 Comparison with manually annotated data

To assess the accuracy of the Neuron Registration Vector Encoding pipeline, we applied our automated tracking system to a 4 minute recording of whole brain activity in a moving C. elegans that had previously been hand annotated and published [70]. A custom Matlab GUI was used for manually identifying and tracking neurons. Nine researchers collectively annotated 70 neurons from each of the 1519 volumes in the 4 minute video. This is much less than the 181 neurons predicted to be found in the head[7]. The discrepancy is likely caused by a combination of imaging conditions and human nature. The short exposure time of our recordings makes it hard to resolve dim neurons, and the relatively long recordings tend to cause photobleaching which make the neurons even dimmer. Additionally, human researchers naturally tend to select only those neurons that are brightest and are most unambiguous for annotation, and tend to skip dim neurons or those neurons that are most densely clustered.

We compared human annotations to our automated analysis in this same dataset. We performed the entire pipeline including detecting centerlines, worm straightening, segmentation, and neuron registration vector encoding and clustering, and correction. Automated tracking detected 119 neurons from the video compared to 70 from the human. In each volume, we paired the automatically tracked neurons with those found by manual detection by finding the closest matches in the unstraightened coordinate system. A neuron was perfectly tracked if it matched with the same manual neuron at all times. Tracking errors were flagged when a neuron matched with a manual neuron that was different than the one it matched with most often. The locations of the detected neurons are shown in Fig 6A. Only one neuron was incorrectly identified for more than 5% of the time volumes (Fig 6B). The locations of neurons and the corresponding error rates are shown in Fig 6B. Neurons that were detected by the algorithm but not annotated manually are shown in gray. Upon further inspection, it was noted that some of the mismatches between our method and the manual annotation were due to human errors in the manual annotation, meaning the algorithm is able to correct humans on some occasions.

GCaMP6s fluorescent intensity is ultimately the measurement of interest and this can be easily extracted from the tracks of the neuron locations across time. The pixels within an approximate 2 μm radius sphere around each point are used to calculate the average fluorescent intensity of a neuron in both the red RFP and green GCaMP6s channels at each time. This encompasses regions of the cell body, but excludes the neuron's processes. The pixels within this sphere of interest are identified in the straightened RFP volume, but the intensity values are found by looking-up corresponding pixels in the unstraightened coordinate system in the original red- and green-channel images, respectively. We use the calcium-insensitive RFP signal to account for noise sources common to both the GCaMP6s and the RFP channel [10]. These

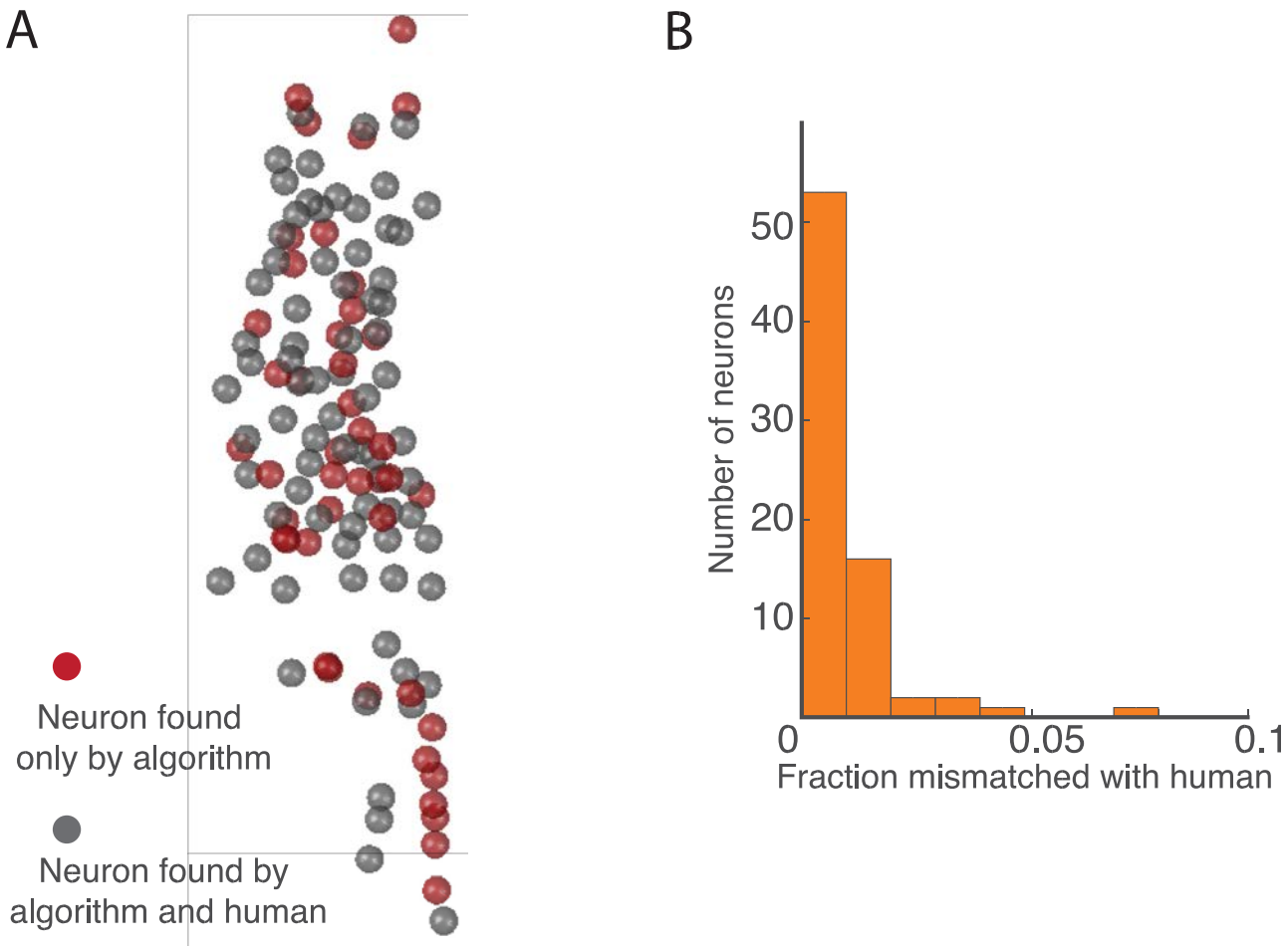


Figure 3.6 Comparison of the automated Neuron Registration Vector Encoding algorithm with manual human annotation. A previously published 4 minute recording of calcium activity (strain AML14) was annotated by hand, [10]. (A) Spheres show position of neurons that were detected by the automated algorithm. Grey indicates a neuron detected by both the algorithm and the human. All neurons detected by the human were also detected by the algorithm (70 neurons). Red indicates neurons that were missed by the human and detected only by the algorithm (49 neurons). (B) Histogram showing number of neurons that were mismatched for a given fraction of time-volumes when comparing automated and manual approaches. Only those neurons that were consistently found by both algorithm and human were considered. An automatically identified neuron was deemed correctly matched for a given time-volume if it was paired with the correct corresponding manual neuron.

include, for example, apparent changes in intensity due to focus, motion blur, changes in local fluorophore density arising from brain deformation and apparent changes in intensity due to inhomogeneities in substrate material. We measure neural activity as a fold change over baseline of the ratio of GCaMP6s to RFP intensity,

$$\text{Activity} = \frac{\Delta R}{R_0} = \frac{(R - R_0)}{R_0}, \; R = \frac{I_{GCaMP6s}}{I_{RFP}} \qquad (3)$$

The baseline for each neuron, R_0, is defined as the 20th percentile value of the ratio R for that neuron. Fig 7 shows calcium imaging traces extracted from new whole-brain recordings using the registration vector pipeline. 156 neurons were tracked for approximately 8 minutes as the worm moves. Many neurons show clear correlation with reversal behaviors in the worm.

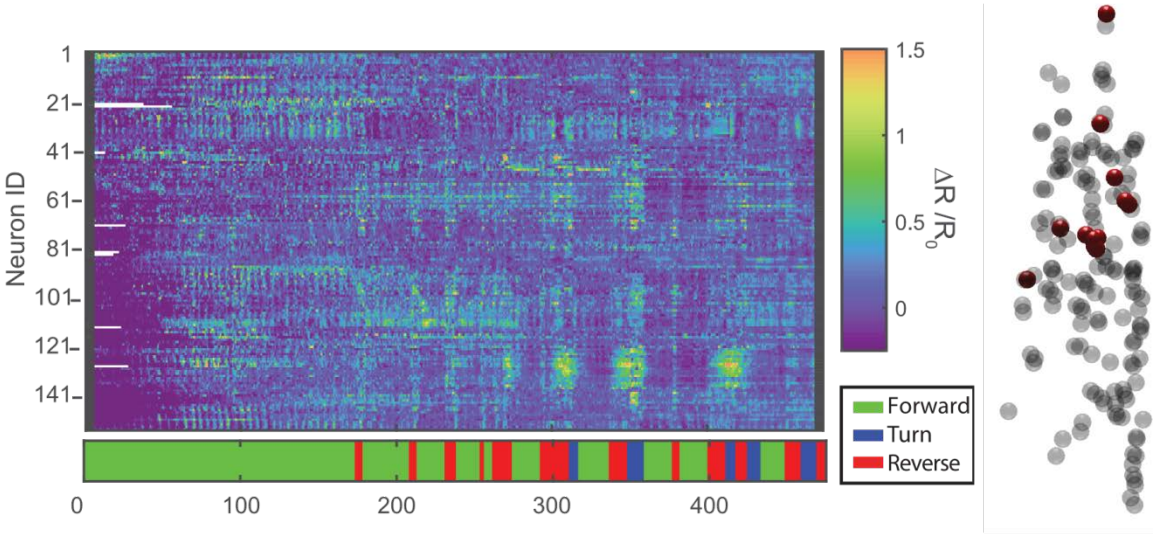


Figure 3.7 Calcium activity traces. Neural activity traces from 156 neurons in the brain a C. elegans as it freely moves on an agarose plate for 8 minutes (strain AML32). The neural activity is expressed as a fold change over baseline of the ratio of GCaMP6s to RFP for each neuron. The behavior is indicated in the ethogram. On the right is the locations of all of the detected neurons (the head of the worm is towards the top of the page). The neurons that have significant correlation with reverse locomotion are indicated in red. White gaps indicate instances where neurons failed to segment. This is a newly acquired recording, different from that in Fig 6.

3.4 Discussion

The Neuron Registration Vector Encoding method presented here is able to process longer recordings and locate more neurons with less human input compared to previous examples of whole-brain imaging in freely moving C. elegans [70]. Fully automated image processing means that we are no longer limited by the human labor required for manual

annotation. In new recordings presented here, we are able to observe 156 of the expected 181 neurons, much larger than the approximately 80 observed in previous work from our lab and others [70,71].

By automating tracking and segmentation, this relieves one of the major bottlenecks to analyzing longer recordings.

The neuron registration vector encoding algorithm primarily relies on the local coherence of the motion of the neurons. It permits large deformations of the worm's centerline so long as deformations around the centerline remain modest. Crucially, the algorithm's time-independent approach allows it to tolerate large motion between consecutive time-volumes. These properties make it well suited for our neural recordings of C. elegans and we suspect that our approach would be applicable to tracking neurons in moving and deforming brains from other organisms as well.

Certain classes of recordings, however, would not be well suited for Neuron Registration Vector Encoding and Clustering. The approach will fail when the local coherence of neuron motion breaks down. For example, if one neuron were to completely swap locations with another neuron relative to its surroundings, registration would not detect the switch and our method would fail. In this case a time-dependent tracking approach may perform better.

In addition, proper clustering of the feature vectors requires the animal's brain to explore a contiguous region of deformation space. For example, if a hypothetical brain were only ever to occupy two distinct conformations that are different enough that registration is not reliable between these two conformation states, the algorithm would fail to cluster feature vectors from the same neuron across the two states. To effectively identify the neurons in these two conformations, the animal's brain must sample many conformations in between those two states.

This way, discrepancies in registration arise gradually and the resulting feature vectors occupy a continuous region in the space of possible feature vectors. Note that a similar requirement would necessarily apply to any time-dependent tracking algorithm as well.

We suspect that brain recordings from most species of interest meet these two requirements: namely neuron motion will have local coherence and the brain will explore a contiguous region of deformation space. Where these conditions are satisfied, we expect registration vector encoding to work well. Tracking in C. elegans is especially challenging because the entire brain undergoes large deformations as the animal bends. In most other organisms like zebrafish and Drosophila, brains are contained within a skull or exoskeleton and relative motion of the neurons is small. In those organisms, fluctuations in neuron positions take the form of rigid global transformations as the animal moves, or local non-linear deformations due to motion of blood vessels. We expect that this approach will be applicable there as well.

3.5 Materials and Methods

3.5.1 Strains

Transgenic worms were cultivated on nematode growth medium (NGM) plates with OP50 bacteria. Strain AML32 (wtfIs5[Prab-3::NLS::GCaMP6s; Prab-3::NLS::tagRFP]) was generated by UV irradiating animals of strain AML14 (wtfEx4[Prab-3::NLS::GCaMP6s; Prab-3::NLS:: tagRFP]) [10] and outcrossing twice.

3.5.2 Imaging C. elegans

Imaging is performed as described in Nguyen et al [10]. The worm is placed between an agarose slab and a large glass coverslip. The coverslip is held up by 0.006” plastic shims in order

to reduce the amount of pressure on the worm from the glass, and mineral oil is spread over the worm to better match refractive indices in the space between the coverglass and the worm. The dark field image is used to extract the animal's centerline while the fluorescent image is used for tracking the worm's brain. Only the head of the worm is illuminated by the fluorescent excitation light and can be observed in the low magnification fluorescent image.

The two low magnification videos and the RFP and GCaMP6 high magnification videos are aligned by imaging a slide of 4 μm "Tetraspeck" beads (ThermoFisher) that emit light in both red and green channels. We manually or automatically locate the beads from calibration images and use the bead positions to find affine transformations between each camera's coordinate system. The affine parameters are found using a least squares fit on the coordinates of the beads in the image.

3.5.3 Thin plate spline transformations

Thin plate spline (TPS) transformations play an important role in error correcting and are also critical for the point set registration algorithm [24]. Given a set of n initial control points $\mathbf{X} = \{\mathbf{x}_i\}$, and the set of transformed points, $u[\mathbf{X}]$, the TPS transformation u can be written as $u[\mathbf{X}] = \mathbf{W}\mathbf{U}(\mathbf{X}) + \mathbf{A}\mathbf{X} + \mathbf{t}$. The affine portion of the transformation is $\mathbf{A}\mathbf{X} + \mathbf{t}$, while $\mathbf{W}\mathbf{U}(\mathbf{X})$ is the non-linear part of the transformation from TPS. $\mathbf{U}(\mathbf{X})$ is an $n \times n$ vector with $\mathbf{U}_{\mathbf{i};\mathbf{j}} ¼ {}_{\mathrm{k}}____{}_{\mathbf{x}}\mathbf{j}\ {}^{\mathbf{1}}{}_{\mathbf{x}}\mathbf{i}\mathrm{k}$ and $\mathbf{W}$ is a $3 \times n$ matrix. The elements of $\mathbf{W}$, $\mathbf{A}$ and $\mathbf{t}$ are the parameters of the transformation u. These parameters are found in different ways dependant on context. During the error correction processing step, these parameters are fit by knowing both the the set of control points $\mathbf{X}$ and the location of the transformed points $u[\mathbf{X}]$. In the context of the point set registration algorithm, $u[\mathbf{X}]$ incurs an energy penalty for deforming space given by $E_{\mathrm{Deformation}}(u) = \mathrm{trace}(\mathbf{W}\mathbf{U}\mathbf{W}^{\mathbf{T}})$ [24].

This cost is used in Eq 2 to determine the total energy of the transformation. Gradient descent is then used to determine the optimal TPS transformation parameters by minimizing the total energy of the transformation.

3.5.4 Clustering

Clustering is performed in two steps: hierarchical clustering and neuron classification. We chose to perform hierarchical clustering only on an initial subset of 800 volumes because hierarchical clustering can become prohibitively computationally intensive for larger datasets. The correlation distance, $1 - \mathrm{corr}(\mathbf{v}_m, \mathbf{v}_n)$, was used as the pairwise distance metric for clustering. Agglomerative hierarchical clustering was implemented using complete linkage with a distance cutoff of 0.9. Clusters which are smaller than 40% of the number of subset volumes were removed. After the clusters were defined via hierarchical clustering, we then performed neuron classification.

To classify neurons, we assigned neurons from every volume to the cluster with the nearest centroid. Only the best matched neuron in each volume is assigned to a cluster and only if the neuron is closer than some threshold distance, described below. If two or more neurons from a volume would otherwise be assigned to a single cluster, the closest neuron retains that classification and other neurons are unassigned. As a result, some putative neurons are not assigned to any cluster and at most one neuron per volume is assigned to any given cluster. The implementation of the algorithm is shown in Algorithm 1.

The threshold distance to determine whether a neuron is assigned to a cluster is calculated using a statistical analysis of the clusters generated by the initial hierarchical clustering so as to discriminate between neurons that are likely correctly or incorrectly assigned. The threshold is

calculated as follows: For each neuron assigned during the initial clustering, we collect the distance between that neuron and the center of the cluster it was assigned to. The distribution of these distances is the “correctly assigned” distribution. In contrast, the null distribution is found by collecting the distances between each neuron and all clusters to which that neuron is not assigned. The threshold distance is set to be the largest distance for which a distance is more likely to be found in the “correctly assigned” distribution than the null distribution.

Algorithm 1 Clustering the Neuron Registration Vectors

input: Set of registration vectors $V = \{\mathbf{v}_{i,t}\}$
output: Cluster assignments for each of the vectors in V
procedure CLUSTER(V)
    S = subset of V
    subset_assignments = hierarchically cluster S with distance cutoff 0.9
    cluster_list = unique(*subset_assignments*)
    for each *cluster* in *cluster_list* **do**
        If size(*cluster*) > 40% of volumes used **then**
            cluster_center = average of S assigned to *cluster*
        else
            remove *cluster*
        end if
    end for
    compute *threshold* from S
    for each $\mathbf{v}_{i,t}$ in V **do**
        d = distances from $\mathbf{v}_{i,t}$ to *cluster_centers*
        if any(d < *threshold*) **then**
            assign $\mathbf{v}_{i,t}$ to closest cluster
        end if
    end for
    for each volume in the recording **do**
        for each *cluster* in *cluster_list* **do**
            if multiple $\mathbf{v}_{i,t}$ from volume assigned to cluster **then**
                unassign all $\mathbf{v}_{i,t}$ from the cluster except the closest one
            end if
        end for
    end for
end procedure

3.5.5 Algorithm implementation

The analysis was performed on Princeton University's high-performance scientific computing cluster, "Della" primarily consisting of 240 nodes and 4288 cores, each with 2.4 GHz processors. Jobs were run on up to 200 cores simultaneously. Timing information for the steps listed in Fig 1 are described below and summarized in Table 1.

Table 1. Breakdown of computation time and scalings for Neuron Registration Vector Encoding pipeline. n_{frames} is the total number of low magnification images used to detect centerlines, n_{vol} is the total number of volumes in the recording, n_{ref} is the number of reference volumes used for creating feature vectors, $n_{neurons}$ is the total number of neurons detected, and n_{subset} is the number of neurons in the subset of volumes used for initial clustering.

Analysis Step		**Computation**	**Approx. % of real time**	**Computational time scales as**
Centerline Detection		Linear	4	$O(n_{frames})$
Worm Straightening		Parallel	10	$O(n_{vol})$
Segmentation				
Registration Vector Encoding		Parallel	80	$O(n\text{vol} \times n\text{ref})$
Clustering	Hierarchical	Linear	2	*O*ðn2subset *n*2neuronsÞ
	Classification	Linear	0	$O(n\text{vol} \times n\text{neurons})$
Error Correction		Parallel	4	up to *O*ðn2volÞ *n*neurons

Centerline detection. Centerlines in each image are calculated using information from the previous centerline and as a result must be computed linearly. Total computational time for centerline detection scales linearly with recording length. Specifically, centerlines must be fit for every frame of the low magnification video so the computation time scales as $O(n_{frames})$.

Worm straighteningand and *segmentation*. Straightening and segmentation are parallelized over each volume. Total computation time for worm straightening and segmentation scales as $O(n_{vol})$, with each volume taking *20 seconds on a single core.

Registration vector construction. Registration vector construction is the most computationally intensive part of the algorithm. The vectors are created by performing non-rigid point-set registration between all sample volumes and all reference volumes. Total computation time scales as $O(n_{vol} \times n_{ref})$ with the bulk of the computational time consumed by gradient descent during point-set registration. The gradient descent for matching a single sample volume to a single reference on one processing core takes *15s. This step is parallelized over each volume.

Clustering. Clustering is broken into two subparts, hierarchical clustering and classification. Clustering is overall fast compared to point-set registration. Computation time for hierarchical clustering scales quadratically with the number of neurons in the worm times the size of the initial set of volumes used to define the clusters. This can become prohibitively slow if we increase the number of volumes used for hierarchical clustering as the length of the recordings increase. Thus, we fix the number of volumes used for initial hierarchical clustering to an arbitrary size (e.g. 800 volumes) regardless of the length of the recording. Thus, the clustering time scales as $O(n^2_{subset}\ n^2_{neurons})$. After the clusters are defined via hierarchical clustering in the first subpart, all neurons can then be quickly classified into clusters with negligible computational time in the second subpart.

Error correction. Error correction is parallelized over each neuron, with each neuron checked in every volume. The error checking in each volume is done by comparing the pointset to all other point-sets using a thin-plate spline transformation. This operation is fast compared to

the registration vector construction step because here the correspondences between the point sets are already known. Computation time for this process scales as $O(n_{vol}^2 \; n_{neurons})$. We chose to compare each neuron in each volume to all other volumes because these comparisons are relatively fast. However, we also observe that comparing each neuron with merely a subset of volumes seems to suffice without loss of performance. In that case the computation time for error correction would be $O(n_{vol} \times n_{neurons} \times n_{subset})$, where n_{subset} is the number of volumes selected for comparison during error correcting.

An 8 minute recording of a moving animal has approximately 3000 volumes and 250 GB of raw imaging data and can be processed from start to finish on the university cluster in less than 40 hours. Major time reduction could be achieved by reducing the number of reference volumes used during Registration Vector Encoding.

Chapter 4

Whole brain dynamics underlying behavior

4.1 Introduction

Advances in neural recording technologies have enabled unprecedented insight into how neural circuits coordinate and generate behavior. Optical imaging of partial circuits have been used across model organisms to probe the neural activity underlying behavior, from decision making in mice during navigation[1] to behavioral choices in the leech[5]. Recording from the entire brain is possible in smaller, transparent model organisms, such as *Caenorhabditis elegans*[24], [70], [71], *Drospophila*, and zebrafish[2]. Such recordings from freely moving *C. elegans* provide an attractive platform to more fully probe the whole brain dynamics that underlie behavior.

Through knowledge of the connectome and ablation studies, many of *C. elegans* 302 neurons have been identified as being involved in specific behaviors. Mechanosensory neurons

synapse on to command-like interneurons, such as AVA and AVB, which synapse onto motor neurons. Ablation of AVA leads to deficits in backward movement, while ablation of AVB impairs forward movement[7], [20]. Suppression of RIM has also been shown to induce reversals independently of the AVA mediated circuit[42]. Turns are tightly coupled to reversals, but are thought to be mediated by a distinct circuit. Ablation studies have shown that SMD regulates turning, while RIV controls the turn direction[23]. These ablations had no effect on reversals, indicating a separation of the two circuits. While these studies have identified key components of the circuits driving behavior, it remains unknown whether there are other neurons involved, and at what time scales their activity is necessary.

Calcium imaging and optogenetic manipulations have helped address the shortcomings of ablation studies. Activity of AVA increases during reversals, and optogenetic stimulation induces reversals, confirming its role in backward locomotion[24], [25]. Several other neurons, such as RIM and AIB, have been shown to exhibit similar responses, suggesting that these neurons, and possibly others, are involved in the circuit[24], [25], [43]. Whole-brain imaging in restrained worms has shown that many neurons participate in coordinated dynamic activity, but it is unclear whether these states of activity dispersed throughout the network actually relate to behavior[24].

A key aspect of understanding how neural activity drives behavior is determining the time scale at which the neurons are performing these computations. Calcium imaging studies of the olfactory circuit of *C. elegans* suggest that odor concentration is integrated over time in sensory neurons to behavioral decisions[77]. In the leech, behavioral decisions can predicted from the activity of the neural population occurring 300 msec before the actual behavior[5]. While these studies show that the nervous system can use past neural activity to drive current

behaviors, it is unknown if this is only the case for decision making in response to variable sensory information, or if it holds true for choosing action sequences in spontaneous behavior.

We sought to understand the size and separation of the circuits controlling locomotion and turning, as well as the time scales of the activity driving these behaviors. Using the methods described in Chapters 2 and 3, we recorded the calcium dynamics from the entire head of freely moving worms as they explored an arena[70], [78]. As discussed in these chapters, we cannot infer neuronal identity from position, nor can we match neuron identity between worms. However, from the neural activity, we are able to predict the behavior of the animal. The weighted neural activity from these predictions indicates several features of the dynamics underlying behavior. We show that the behavior is best predicted by using the concurrent neural activity, and not integrating over prior activity. Additionally, the number of predictive neurons found indicates that behavioral information is dispersed throughout a large portion of the nervous system. The two behaviors considered, forward/backward locomotion and turning, are encoded in mostly non-overlapping subsets of neurons, with some cross talk between them. This work suggests behavior is enacted by mostly distinct circuits.

4.2 Results

4.2.1 Moving worms have more activity and dynamics than immobilized worms

As a first step in exploring the global brain dynamics underlying behavior, we looked at the difference between immobilized worms and worms that were freely moving. Changes in the ratiometric fluorescence of GCaMP6s and RFP were recorded from most of the neurons in the worms head. Figures 1A and 2A show these changes in fluorescence, a proxy for neural activity,

in a large population of head neurons for worms that were either immobilized (Fig 1) or freely behaving (Fig 2). These heat maps show that freely behaving worms exhibit striking differences in activity compared to immobilized worms.

We performed principal components analysis on the neural activity of each worm, seeking a description of neural activity in a reduced dimensional space for easier comparison of the dominant dynamics in freely moving versus immobilized worms. In both moving and immobilized worms, the weights in the first component are distributed across a large number of neurons (Fig 1B, Fig 2B). This appears to be the result of antagonistic activity of two sets of neurons. A similar distribution of weights is seen in the second component in behaving worms. However, the second component in immobilized worms consists of large weights on a small number of neurons. While the principal components describe roughly the same percentage of variance (Fig 1d, Fig 2d), the number of neurons involved in generating that variance is smaller in immobilized worms. This indicates that while moving and immobilized worms share some basic dynamics, the activity in moving worms is dispersed across more neurons.

The projections of the neural activity onto this lower dimensional space also illustrate some of the difference and similarities between neural activity in freely moving versus immobilize worms. The projection onto each component as a function of time shows that the antagonistic set of neurons in the first mode has a strong oscillatory component (Fig 1c, Fig 2c). However, this oscillation is much faster in moving worms than in immobilized worms, suggesting that the switch between these two sets of neurons occurs more frequently in behaving worms.

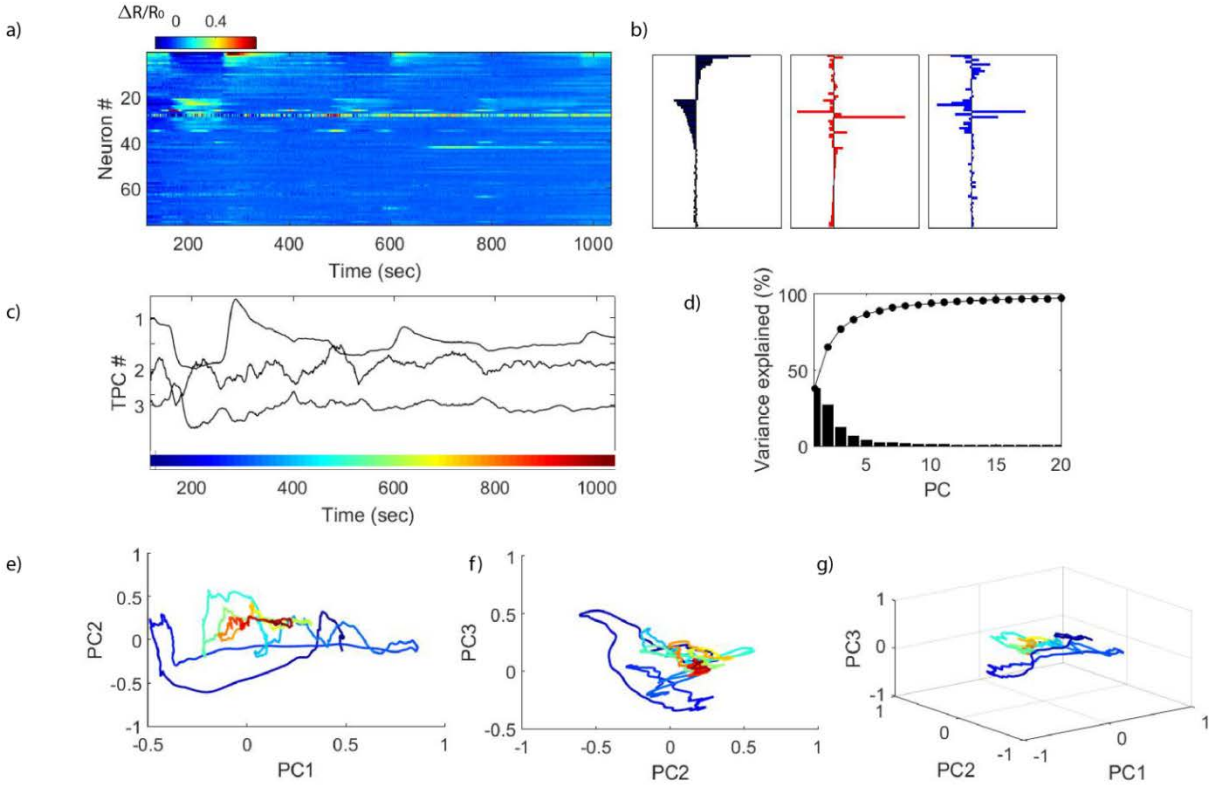


Figure 4.1: Brain-wide activity of an immobilized worm a) Heat map of the ratiometric fluorescence of 76 head neurons, sorted by their principal component weight and signs. b) First three principal components weight and signs. Neuron numbers correspond to those of the heat map. c) Projections onto the first three principal components as a function of time. d) Variance explained by the principal components. The black line shows the cumulative variance explained. e-g) Projections onto principal components, color coded as a function of time. The colormap of time is seen in figure 4.1 c).

Previous studies have found that in immobilized worms, the projection onto the first three principal components traces a cyclical trajectory in this low dimensional space. Unlike this study, we do not see a consistent, stereotyped trajectory of neural activity in this space in either immobilized or moving worms (Fig 4.1e-g and Fig 4.2 e-g). In the case of immobilized worms, this is likely due to differences in the immobilization methods. The lack of a cyclical trajectory for freely behaving worms suggests that these first three dimensions are not exclusively related to the motor behavior of the worm, and thus do not embed the motor command sequence.

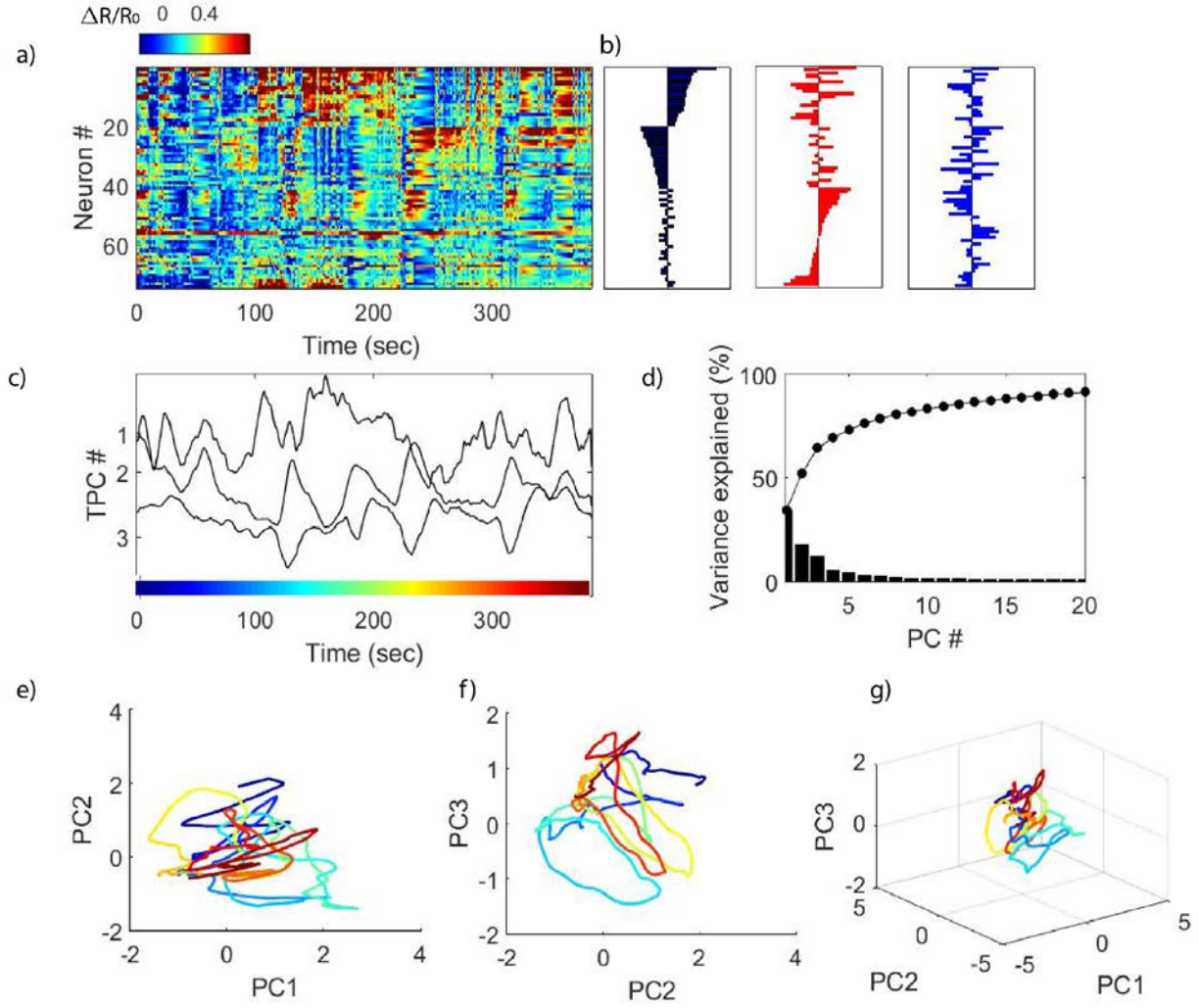


Figure 4.2: Brain-wide activity of a freely behaving worm a) Heat map of the ratiometric fluorescence of 74 head neurons, sorted by their principal component weight and signs. b) First three principal components weight and signs. Neuron numbers correspond to those of the heat map. c) Projections onto the first three principal components as a function of time. d) Variance explained by the principal components. The black line shows the cumulative variance explained. e-g) Projections onto principal components, color coded as a function of time. The colormap of time is seen in figure 4.2 c).

While it would be interesting to know if the same neurons dominate the first modes across worms, both moving and immobilized, we are currently unable to address this question. As shown in Chapter 2, the positions of the neurons are insufficient for reliable identification across worms. This prevents us from pooling data across worms, limiting our statistical power

and ability to draw conclusions about how any individual neuron contributes to the global neural activity across worms.

Although immobilized worms have been used to provide insight into how neural activity drives behavior, we see large differences in the global brain dynamics between immobilized and freely moving, behaving worms. Looking at the distribution of time that a neuron is active for, defined as being 1.5 standard deviations above baseline, we see that in immobilized worms, a larger portion of neurons are active for less than 10% of the time. In freely moving worms, most neurons are active for at least 20% of the time. In immobilized worms, we see a longer tail on the distribution of the time, indicating that when neurons are active, they are active for longer compared to moving worms (Fig 4.3a). This is further supported by looking at the power spectral density of the neurons in immobilized versus moving worms (Fig 4.3b). We see that neurons in moving worms have more power in higher frequencies than in immobilized worms, indicating that neurons in moving worms are active at a higher frequency than immobilized worms.

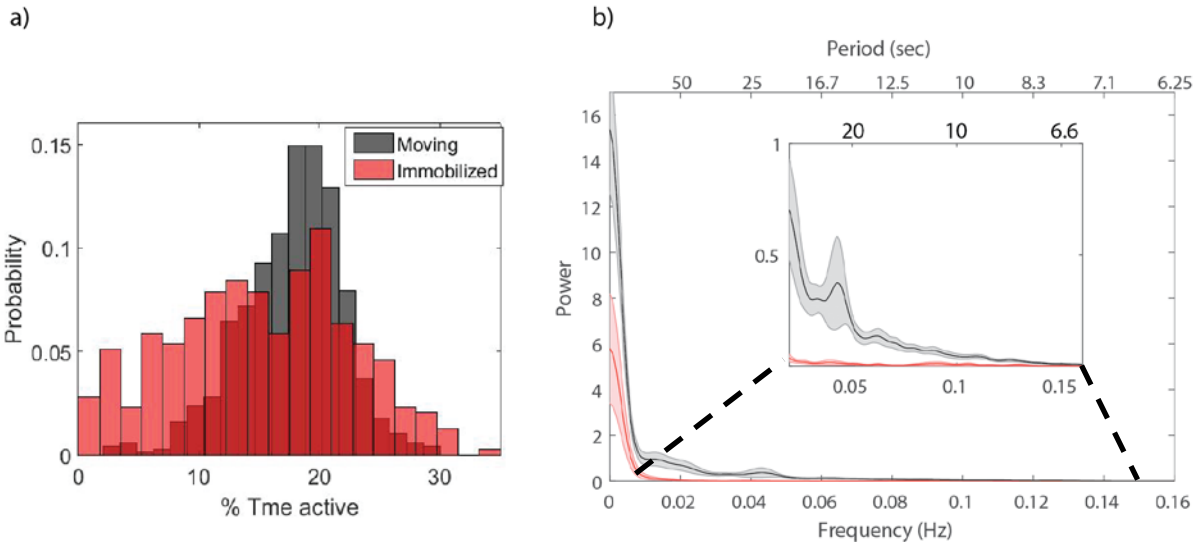


Figure 4.3: Activity in freely moving vs. immobilized worms. a) Distribution of the probability of the amount of time individual neurons are active in immobilized (red) and freely moving (black) worms. b) Power spectral density of neuronal activity in immobilized (red) and freely moving (black) worms. Shaded error bars indicate $\pm$ SEM. Inset shows a zoomed in portion of the PSD, indicated by the dashed lines. A time axis corresponding to the period corresponding to the frequency is provided at the top of the figure.

4.2.2 Neural activity can predict forward and backward locomotion

To find a mapping between neural activity and behavior, we need a quantitative description of behavior that is relevant to what the neural activity might actually be driving. To derive such a description, we begin with the centerline of the worm, or its posture. The posture can be decomposed into four posture modes, such that every shape that the worm assumes can be described as a weighted sum of these four modes (Fig 4.4a). By projecting the worm's posture into the space of these modes, we can now describe the behavior as a trajectory through a low dimensional posture space. Specifically, the first two modes are sinusoidal with a phase offset, corresponding to the body bending wave that propagates along the worm's body as it moves forward or backward. However, given a single point in this posture space, it is impossible to say if the worm is moving forward or backward (Fig 4.4b). To determine this, we look at the angle

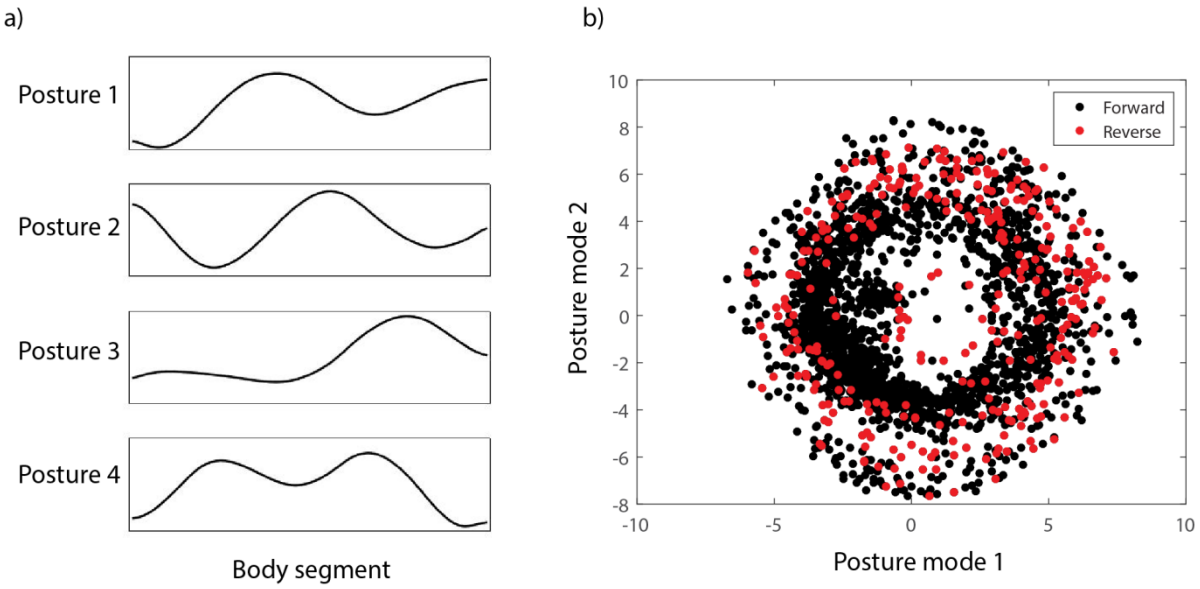


Figure 4.4. Postural dynamics of the worm. a) First four principal posture modes, or eigenworms. b) Projection onto the first two principal posture modes. Black indicates times when the worm was moving forward, red indicates backwards locomotion.

that a point makes with the x axis, and quantify the worms behavior as the change in that angle (Fig 4.5a). The trajectory of forward locomotion follows a clockwise trajectory, resulting in a negative dθ/dt, while reversals follow a counterclockwise trajectory, leading to a positive dθ/dt (Fig 4.5c).

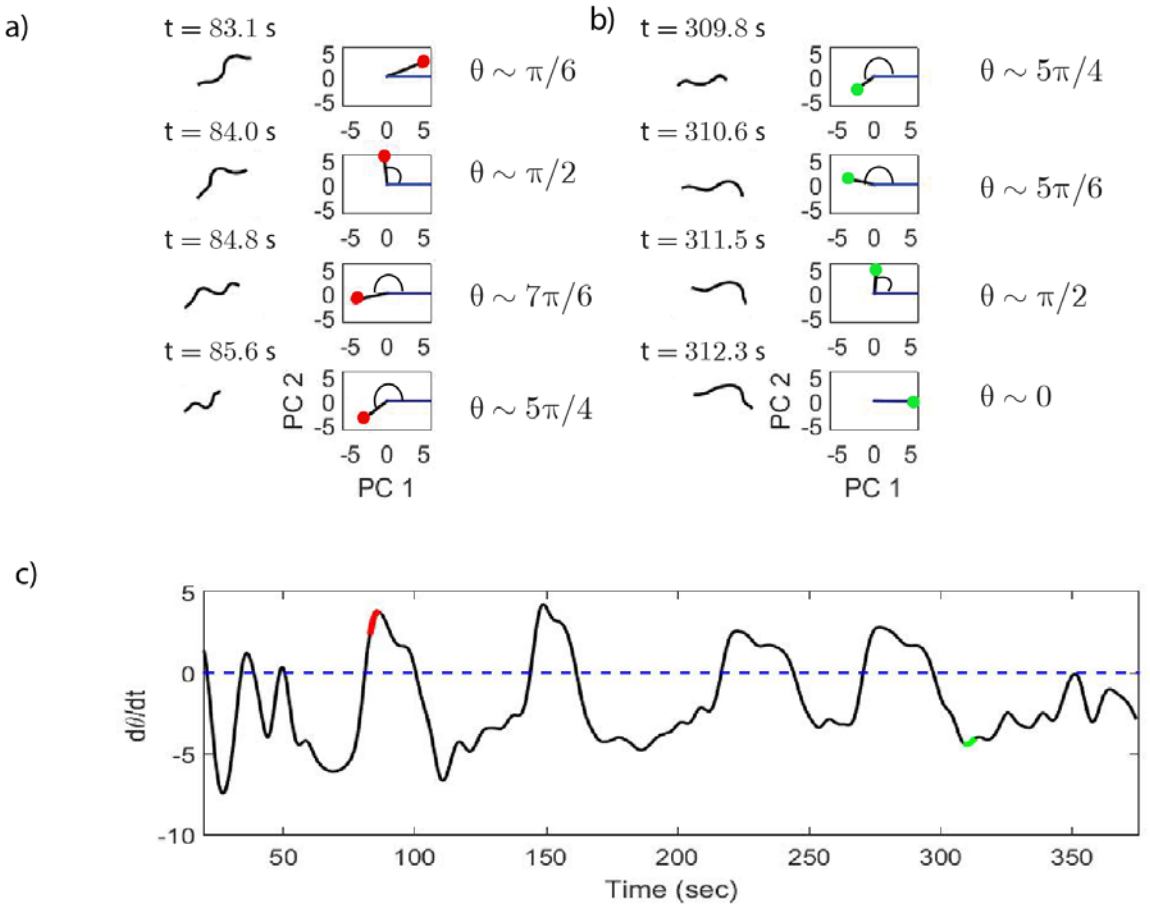


Figure 4.5: Distinguishing forward and backward locomotion in posture space. a) Example of backward locomotion in posture space. The left column shows time lapsed postures of the worm in the arena. The second column shows the projection of the corresponding frame onto the first two principal components, indicated by the red dot. Lines were added to indicate the angle associated with that point, an estimate of which is given in the third column. b) Example of forward locomotion in posture same. Columns are the same as in a), but with a green dot to indicate the projection in posture space. c) Change in the angle as a function of time. Dashed line at zero indicates the switch between forward and reverse locomotion. The location of the examples in a) and b) are indicated by red and green points respectively.

If the neural activity in the head of the worm is driving this behavior, it should be possible to predict this quantitative representation from the activity we have recorded. This would generate a mapping between neural activity and behavior, and demonstrate that these neurons are encoding information about what the worm is doing. Additionally, this would provide information about which neurons are involved in this behavior, providing a framework for us to explore other properties of the circuit, such as the time scales and overlap with other circuits.

To predict the behavior from the neural activity, we model behavior ($d\theta/dt$) as a linear function of the neural activity (N),

$$\frac{d\theta}{dt}(t) = \sum_{i=1}^{nNeuron} w_i N(i,t) \quad (1)$$

Finding the weights, w_i, that best solve this equation can be done with linear regression. However, as we are interested in exploring the size of the network driving locomotion, we want to see how the prediction of behavior changes as a function of the number of neurons used. This is accomplished by using lasso (least absolute shrinkage and selection operator) regression. Lasso adds a regularization parameter on the weight matrix in the minimization problem to induce sparsity. So weights are found by solving

$$\min_{w \in \mathbf{R^n}} \left(\left\| \frac{d\theta}{dt} - Nw \right\|_2^2 + \lambda \|w\|_1 \right). \quad (2)$$

Increasing the value of λ drives more of the weights to zero.

The data from each worm was divided into three sections: training (60%), validation (20%) and testing (20%). In training, ten random subsets of points, sampled such that the entire range of dθ/dt was present in each subset, was chosen. For each of these, a set of weights was found by solving Eq. 2 for a range of lambdas. To choose an appropriate value of lambda, we use the validation set of the recording. In this validation section, we look at the average mean squared error across these subsets, and pick the λ that induced the most sparsity while still having a mean squared error within one standard deviation of the minimum mean squared error (Fig 4.6a). We see that increasing the penalty for nonzero weights initially enhances our prediction, but that at high values of lambda with a very sparse weight matrix, our predictions become much worse. This indicates that information about behavior is dispersed throughout a small subset of the neurons recorded, and suggests that the activity of an individual command interneuron is not solely responsible for encoding this behavior.

Predicting the behavior also allows us to explore the time scale at which the neural activity is driving the behavior. Ablation studies have identified neurons that are involved in locomotion, but it is unknown whether behavior is driven by the magnitude of their current neural activity, or if the circuit is integrating over what has happened previously. To probe the time scale at which neural activity drives behavior, we looked at how changing the amount of time included in the prediction changes the outcome. This was modeled as the behavior being a linear combination of the concurrent neural activity as well as the neural activity preceding it.

$$\frac{d\theta}{dt}(t) = \sum_{i=1}^{nNeuron} w_i N(i, t - dt: t) \quad (3)$$

Lasso regression was used to find the weights of neural activity at times between the current

behavior and up to 1.67 sec preceding it. For a given behavior point, weights were derived for the concurrent neural activity (t = 0), as well as for the neural time points preceding it. We see that including more past information does not improve our predictions of behavior (Fig. 4.6b). This suggests that the magnitude of the current neural activity is what is driving this behavior, and that prior neural activity is not necessary to predict behavior.

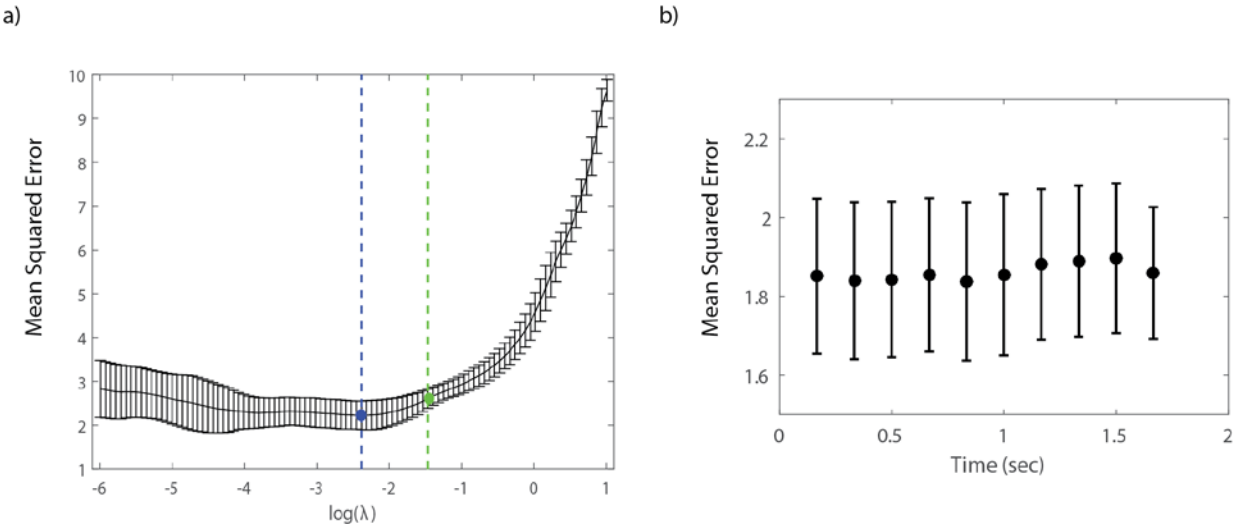


Figure 4.6: Mean squared error of dθ/dt from varying parameter values in the validation set. a) Mean squared error as a function of λ. Increasing λ increases the sparsity of the weight matrix. Blue dot and line indicate the value of λ with lowest mean squared error, green dot and line indicate the value within one standard error of the minimum. b) Mean squared error as a function of time scale. Time indicates the amount of time prior to the behavior was used to predict the behavior.

In predicting behavior from neural activity, motion artifacts pose a potential concern. The movement of the worm might cause neurons to expand or compress which could change the density of the fluorescent indicators and create the appearance of a calcium transient. If this happens in a stereotyped manner based on the posture of the worm, the motion artifact would be predictive of the behavior. In this situation, we would essentially be predicting the worm's

behavior from its behavior, and not its neural activity. To see if this was the case, we recorded from worms expressing GFP, a fluorophore which is calcium insensitive. Any signal used to predict the behavior in these worms is entirely the result of motion artifact. As we can see from the examples shown, the activity of the GCaMP6 worms is significantly better at predicting the behavior than the GFP worms (Fig 4.7). This shows that it is the neural activity that is predictive of the behavior, and not changes in fluorescence due to motion.

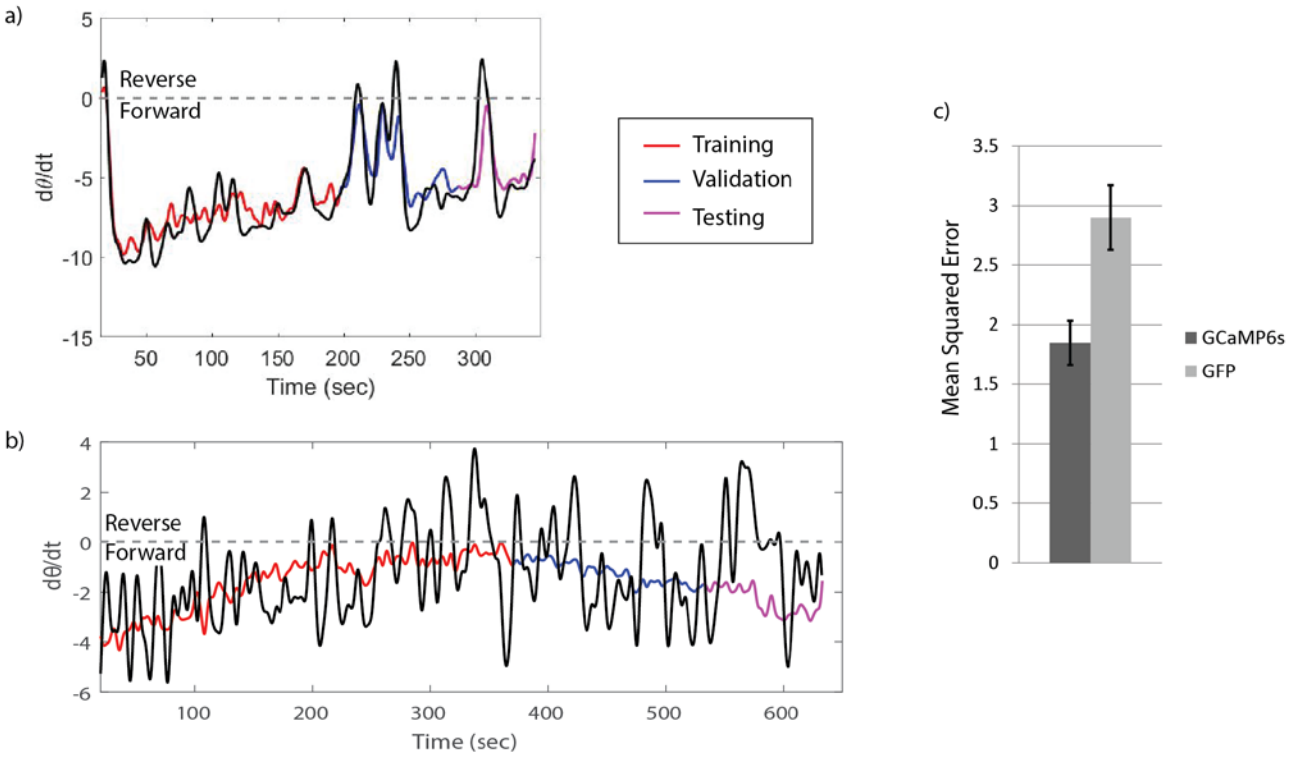


Figure 4.7: Predicting forward and backward locomotion from neural activity. a) Example of a prediction of dθ/dt in a freely moving worm expressing GCaMP6s. Red indicates the section used for training, blue is the validation set, and pink is the test set. b) Example of predicting dθ/dt from a freely moving worm expressing GFP. c) Mean squared error of the test set across worms. Error bars indicate ± SEM. (GCaMP6s n = 8, GFP n = 5).

4.2.3 Predicting turns from neural activity

While forward and backwards locomotion are intuitively characterized as a continuous variable, turning is better understood as a binary event. To predict turning, we classify the behavior as either not turning (value of 1) or turning (value of 2), and use support vector machines (SVMs) on the neural activity to predict the behavioral classification. As with forward and backward locomotion, we seek to explore the size of the network driving this behavior. To do so, we modified the classic soft-margin SVM to use the L_1 norm of the weight matrix. This is done by solving the minimization problem

$$\min_{w \epsilon R^n} \left(\lambda \|w\|_1 + \frac{1}{M} \sum_{i=1}^{M} \max(0, 1 - y_i(w * N - b). \right.$$

$$\begin{gathered} y_i = \text{binary value i} \\ M = \text{number of observations} \\ b = \text{offset} \end{gathered} \tag{4}$$

As with lasso, increasing λ allows us to increase the sparsity of our weight matrix. The first part of each recording that included 70% of the turns was used for training and validation. Within this portion, each individual turn was paired with an equal number of non-turning points to generate a fold. Leave-one-out cross validation was used on these folds to determine the appropriate value of λ. Since turning is a binary event, we seek to maximize the F_1 score, a weighted average of the precision and recall. This was calculated from the true positives (TP), false positives (FP), and false negatives (FN),

$$F_1 \text{score} = 2 * \frac{TP}{2*TP+FN+FP} \tag{5}$$

Using the F_1 score from the validation folds, we choose the value of lambda that is within one standard error of the maximum F_1 score (Fig. 4.8.a). As with forward and backward locomotion, we explored whether including prior neural activity enhanced our prediction, and found that it did not (Fig. 4.8b). This shows that turning is encoded by a small subset of neurons whose current neural activity provides the most predictive information about behavior.

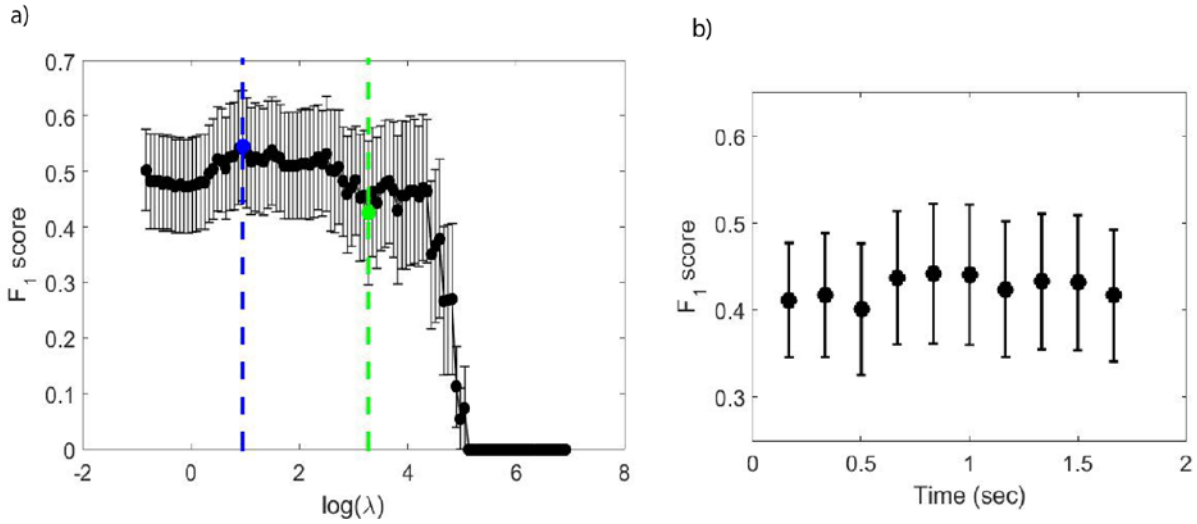


Figure 4.8: F_1 score of binary classification of turns from varying parameters. a) F_1 score as a function of λ. Blue dot and line indicate the highest F_1 score, green dot and line indicate the value within one standard error of the maximum. b) F_1 score as a function of time scale. Time indicates the amount of time prior to the behavior was used to predict the behavior.

To determine whether our classification of behavior was from actual signal in the neural activity or a result of motion artifact, we compared our predictions in GCaMP6s worms to GFP worms. We see that in GcaMP6s worms the weights we've derived do qualitatively good job of predicting whether the worms is turning or not (Fig. 4.9a), while GFP worms are incorrectly predicted to be turning the entire time (Fig 4.9b). This difference in prediction accuracy is quantitatively true across worms, with GcaMP6s worms have a much higher F_1 score than GFP worms (Fig. 4.9c), showing that it is the neural activity that is predicting behavior and not just a

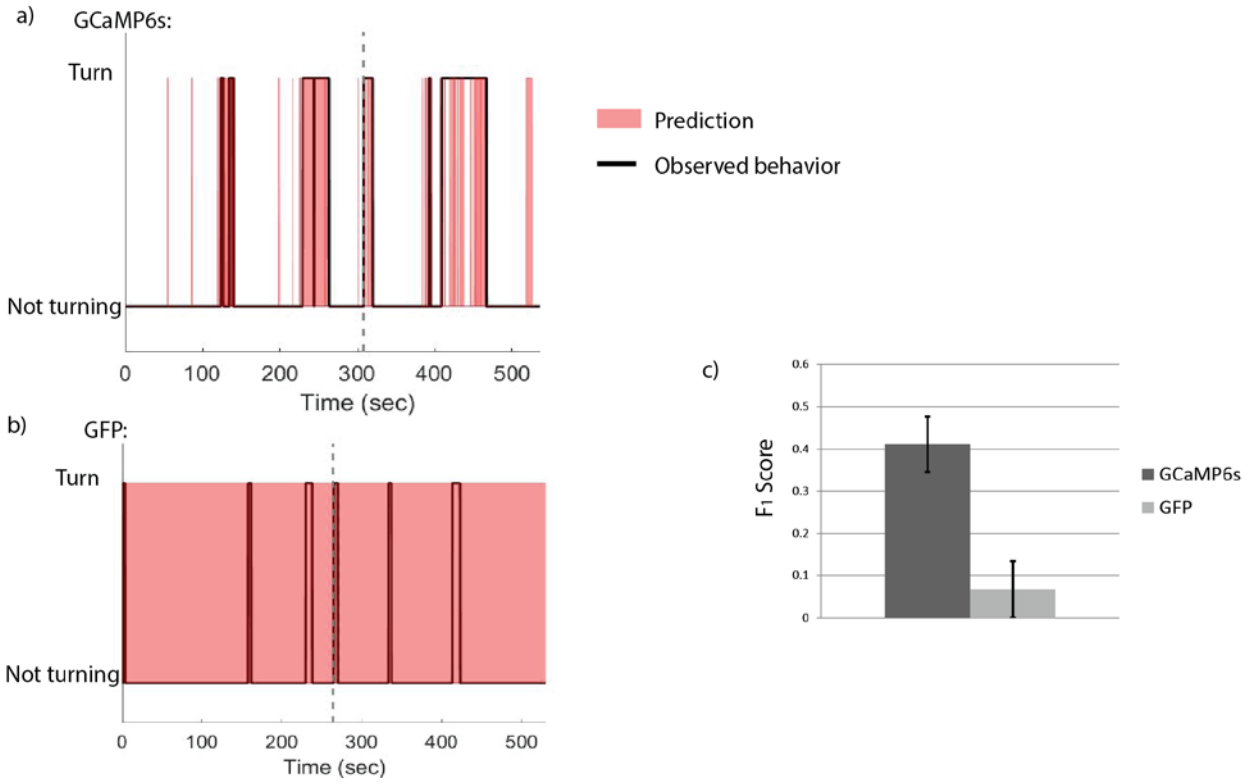


Figure 4.9: Predicting turns from neural activity. a) Example of predicted turns from the neural activity of a freely moving worm expressing GCaMP6s. Black line indicates the observed behavior, red indicates the predicted behavior. Dashed line shows where the training/validation set ends and test set begins. b) Example of predicted turns from the neural activity of a freely moving worm expressing GFP. c) F_1 score of the testing set across worms. Error bars indicate $\pm$ SEM. (GCaMP6s n = 8, GFP n= 4).

motion artifact.

4.2.4 Comparing locomotion and turning

From using lasso and modified SVMs to predict behavior, we have generated two sets of weights for the neurons in each worm: one which predicts locomotion and one which predicts turning. Using this, we can explore the relationship between these two circuits, determining whether they are distinct and whether information about one behavior is present in the circuit that encodes the other. We find that turning is best predicted from the neural activity of about 8 neurons, while forward and backward locomotion is best predicted from the activity of about 25

neurons (Fig 4.10a). The neurons with large weights for each of these behaviors appear to be largely non-overlapping (Fig. 4.10b). Ranking the neurons by the magnitude of their weight for each behavior and seeing how many of the neurons overlap at each rank, we see that the neurons that best predict each behavior are distinct. There is never more than a 20% overlap between the subsets of neurons that predict these two behaviors (Fig.4.10b). This shows that these two behaviors are encoded by two mostly different subsets of neurons, suggesting the presence of two distinct circuits used to drive distinct behaviors.

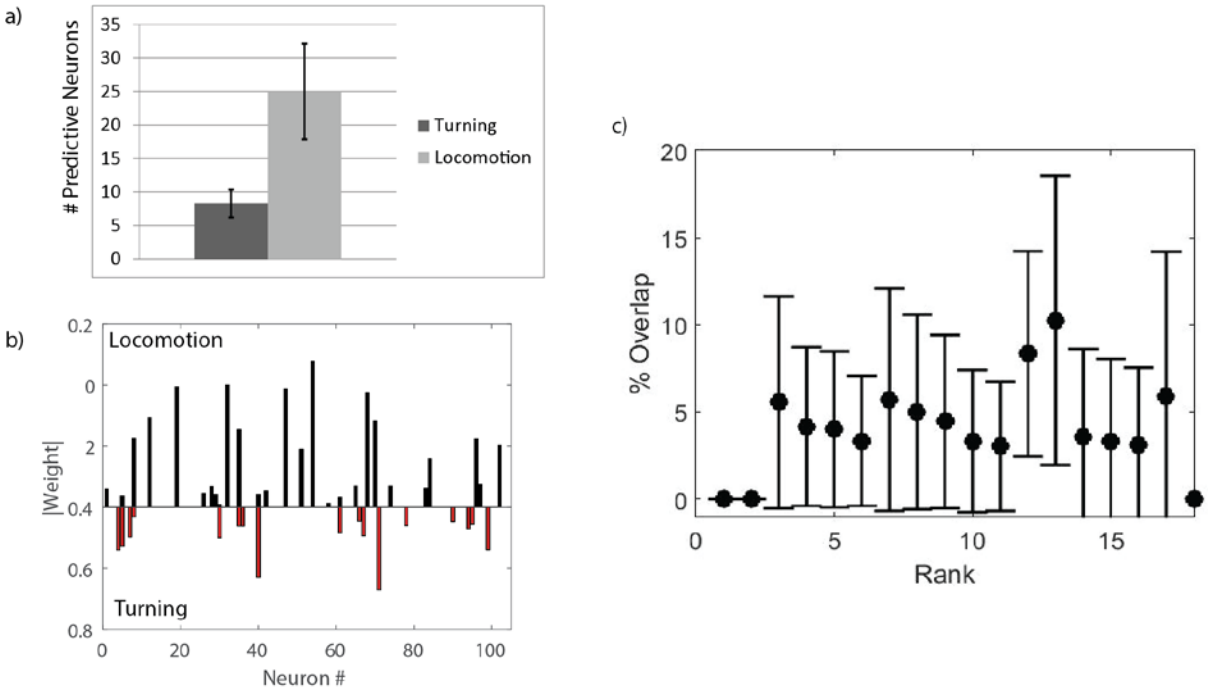


Figure 4.10: Comparing weights of turning and locomotion. a) Number of neurons with nonzero weights for each behavior. b) Example of the weight distribution for locomotion (top, black) and turning (bottom, red). b) Percentage of overlap between top ranking (highest weighted) neurons in turning and locomotion. Error bars indicate $\pm$ SEM, n = 7.

To test how distinct these two subsets of neurons are, we predicted each behavior using only the neurons that were identified as predicting the other. First, we used support vector machines to predict whether the animal was turning or not turning, as was done previously, but only using the neurons that had non-zero weights from lasso (locomotor neurons with overlap).

We additionally did this using neurons that had non-zero weights from lasso and were distinct from the neurons that had non-zero weights for predicting turns (locomotor neurons with no overlap). We see that locomotor neurons with overlap do slightly worse at predicting turning, and that locomotor neurons without overlap do significantly worse at predicting turns. Interestingly, the purely locomotor neurons are still better at predicting turns than the best predictors of turns in GFP animals (Fig 4.11a). This shows that although these neurons are primarily involved in locomotion, they still encode some information about turning.

To further explore the potential separation of these two neuronal subsets, we predicted $d\theta/dt$ using turning neurons. This was done with all neurons that predict turning (turn neurons with overlap), was well as with neurons that predict turning but not locomotion (turn neurons with no overlap). We find that even with a subset of neurons that partially overlaps with those that predict locomotion, we do a significantly worse job at predicting locomotion. This holds true for the subset of neurons that exclusively predict turning. (Fig. 4.11b), indicating that neurons that are predictive of turning have very little, if any, information about locomotion.

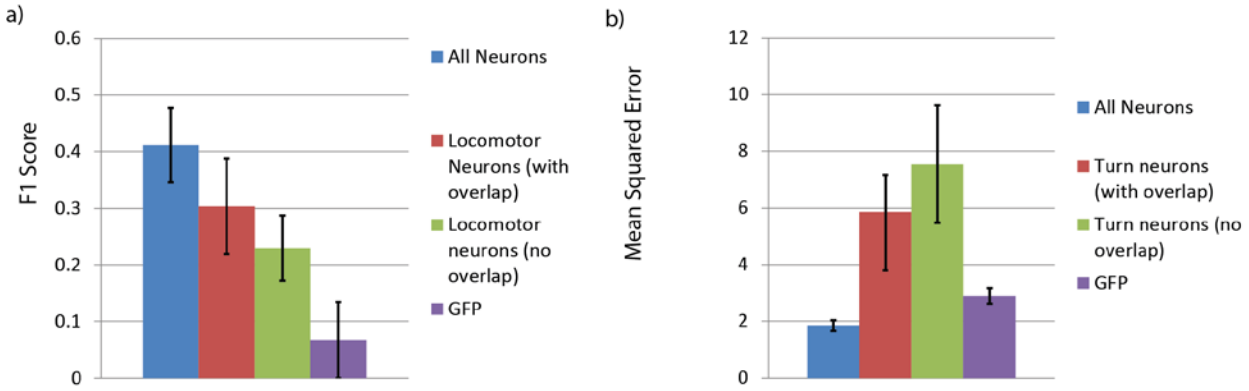


Figure 4.11: Predicting behaviors with different neuron subsets. a) Predicting turns using neurons identified as predicting locomotion. The F1 score was calculated from the behavior predicted in the test set using either all the neurons (blue, same as Figure 4.9c), all neurons identified as predicting locomotion (red), neurons that predict locomotion and do not predict turns (green), and GFP (purple, same as Figure 4.9c). b) Predicting locomotion using neurons identified as predicting turns. The mean squared error was calculated from the behavior predicted in the test set using either all neurons (blue, same as Figure 4.7c), all neurons identified as predicting turns (red), neurons identified as only predicting turns (green), or GFP (purple, same as Figure 4.7c).

4.3 Discussion

In higher level organisms, it is well known that there are differences in neural activity between awake and anesthetized animals. We extend these finding to include *C. elegans*, showing that anesthetized, immobilized animals have less activity and slower dynamics. This appears to be a brain-wide state in the worm, as the overall activity has almost all of its power in very low frequencies.

Unlike other immobilized recordings of C. elegans, we do not see the global brain dynamics embedding the motor command sequence, in either immobilized or freely moving experiments. This is likely due to differences in the experimental preparations. In Kato et al, worms are immobilized using a microfluidic device, in which the worms head is held in place by a small channel, while the rest of the body is resting on a surface. It is likely that the continuous sensory input to the head of the worm does engage the motor sequence repeatedly, as the worm is unable to escape. In our preparation, the worm is immobilized by 100nm beads, creating a constant physical input along its body. This is unlikely to consistently and repeatedly engage the command motor sequence driving escape, which would lead to the less stereotyped neural trajectory we see in our data.

The differences we see in immobilized versus freely moving worms suggests that one should exercise caution when drawing conclusions about behavior from immobilized worms. The decrease in the number of neurons that are active for less than 10% of the time between immobilized and behaving worms suggests that there are more neurons that may be involved in behavior when the worm is actually behaving. Because of this, immobilized recordings may present an overly simplified description of the neural activity.

We show that using a simple linear model, we can predict the behavior of the worm from the neural activity. The weights that arise from this model have several interesting features. For one, a high number of neurons have nonzero weights for locomotion. While not all of these neurons may be actively driving the behavior, it does suggest that information about the current behavior is present throughout the network. The same holds true for turning, as the simple command interneuron driving turns model would suggest that fewer neurons should have nonzero weights.

Another interesting finding is that including prior neural activity does not enhance our prediction of behavior for either turning or locomotion. This suggests that for spontaneous exploration of an environment, the current state of the neural network is driving behavior, and not integrating over the prior activity. Including prior neural activity also allowed for the derivative of the neural activity to predict behavior. As allowing this did not enhance our predictions, it appears likely that it is the magnitude of current activity that is producing these behaviors.

Comparing the weights of neurons for locomotion and turning reveals two largely non-overlapping subsets of neurons. As the neurons that predict turning cannot predict locomotion, it is likely that they are functional distinct from locomotion neurons. However, locomotion neurons can predict turning better than GFP can, indicating that these neurons have some information about whether the animal is turning or not. This suggests that while the circuits underlying these two behaviors are mostly distinct, there is some overlap between them. Such overlap may be a way for the nervous system to coordinate between performing these two behaviors.

While the connectome of the C. elegans nervous system has been mapped out, we are unable to match the neurons we have recorded with their identities of this atlas. Current efforts aim to solve this problem using multicolored fiducial references, and would add great insight into the neural dynamics driving behavior. Knowledge of the neural identities would allow us to determine if the same set of neurons are driving behavior across worms, or if different animals utilize the circuitry differently to generate behavior.

4.4 Materials and Methods

4.4.1 Strains

GCaMP6s recordings were done on strain AML32, while strain AML12 was used for GFP recordings. Strain AML32 (wtfIs5[Prab-3::NLS::GCaMP6s; Prab-3::NLS::tagRFP]) was generated by UV irradiating animals of strain AML14 (wtfEx4[Prab-3::NLS::GCaMP6s; Prab-3::NLS:: tagRFP]) [10] and outcrossing twice. Transgenic worms were cultivated on nematode growth medium (NGM) plates with OP50 bacteria.

4.4.2 Calcium imaging in immobilized worms

Immobilization was achieved through a combination of drug application and physical constraint. The worm was removed from a bacterial lawn and rinsed in a 1mM solution of tetramisole in M9 buffer. The worm was then placed on a thin 10% agarose pad atop a glass slide. One microliter of 100nm polystyrene beads was added on top of the worm. This was covered with a glass coverslip and sealed. Imaging was performed as described in Nguyen et al[70], except the tracking was turned off as the worm was not moving.

4.4.3 Calcium imaging in freely moving worms

Imaging was performed as described in Nguyen et al []. The worm was removed from the bacterial lawn and rinsed in M9 solution. It was then placed between an agarose slab and a glass coverslip. Mineral oil was spread over the worm to better match refractive indices in the space between the coverglass and the worm. To reduce pressure on the worm from the glass, .006" plastic shims were placed between the agarose pad and the coverglass.

4.4.4 Extraction and processing of neural signals

For both immobilized and freely moving animals, individual neurons were identified and tracked throughout the recordings as described in Nguyen et al []. For freely moving worms, 300 reference volumes were used. In immobilized recordings, the lack of motion allowed for the use of only 100 reference volumes, speeding up computation time. Additionally, several of the immobilized recordings were significantly longer than other recordings, such that photobleaching of RFP was best fit with a sum of exponentials instead of a single exponential.

As movement induces noise in the fluorescent signal, we used the calcium insensitive RFP to account for changes common to both the GCaMP6s and RFP channels. Neural activity was measured as a fold change over baseline of the ratio of GCaMP6s to RFP instensity,

$$\text{Activity} = \frac{\Delta R}{R_0} = \frac{(R - R_0)}{R_0}, \; R = \frac{I_{GCaMP6s}}{I_{RFP}} \tag{7}$$

The baseline for each neuron, R_0, is defined as the 20th percentile value of the ratio R for that neuron. On rare occasion, a combination of worm motion and tracking latency caused neurons to briefly leave the field of view. Any neurons that were not present for more than 98% of a given

recording were excluded. Following this and prior to any further analysis, NaN's were removed by interpolation between the adjacent values and a smoothing window of 10 frames was applied to each neurons activity trace.

4.4.5 Principal component analysis of immobilized and freely moving worms

PCA was performed on the ratiometric change in fluorescence. A 10-sample sliding-average was window was applied to the temporal principal component projections. Neurons were sorted by the weight and sign of their principal components. The first 20 are those with the highest positive weights in first component, and the next twenty are those with the most negative weights in the first component. The rest of the neurons were sorted by their weight in the second component.

4.4.6 Measures of activity in immobilized and freely moving worms

A neuron was defined as active if its activity was 1.5 standard deviations above its baseline value. The percentage of time active is the amount of time the neuron was active divided by the total length of the recording. Keeping immobile and mobile worm neurons separate, these values were pooled across worms and segmented into 6% bins. The count of each bin was divided by the total number of neurons to yield the probability.

For reach neuron, a power spectral density was obtained using Welch's method, with a window of 1200 frames (~200 seconds) and overlap of 50 frames (~8.2 seconds). For each worm, the power spectral densities of each neuron were added together and divided by the total number of neurons. The resulting power spectral densities were averaged across worms.

4.4.7 Quantitatively describing locomotion as a continuous variable

The centerline of the worm was found in each high low-magnification behavior image using an active contour model with modifications, as described in Nguyen, et al[70]. The principal components of worm posture, or eigenworms, were derived using principal components analysis on approximately 70,000 images. Because the worms in our set up exhibit slight differences in behavior compared to wild type worms, the first two projections were slightly rotated to lie more on a circle. The angle in the first two modes was found by taking the four quadrant inverse tangent of the two values. The derivative of the angle was found by convolving the angle with the first derivative of a Gaussian with length 100 and σ=15.

4.4.8 Predicting continuous behavior using lasso

Training: The first 60% of each recording was used for training the weights for lasso. To ensure that $d\theta/dt$ was equally sampled, the values of $d\theta/dt$ were separated into five bins. For each subsample, n points were randomly drawn from each bin. The number of points drawn from each bin was half the number of points in the bin with the fewest total number of points. The lasso regression function in Matlab was used on ten different subsamples for each recording.
Validation: The 20% of the recording following the training set was used for validation and choosing parameters. This data was not used in the training set. The mean squared error for each value of λ for each of the ten subsamples was calculated. For each λ, the average and standard error of the mean squared error from each subsample was calculated. To choose a final value of λ for testing, we found the value that provided the lowest mean squared error, and then chose the highest value of λ for which the mean squared error was within one standard error of

the lowest mean squared error. Once this value was determined, the weights were chosen from the subsample that yielded the lowest mean squared error for that value of lambda.

Testing: Testing was performed on the last 20% of each recording. This data was completely separate from the data used in validation and training. The weights and parameters used were determined by the validation set.

Probing time scales: Weights for each time point for each neuron were treated independently. This was done by generating a matrix of the neural activity such that for each time t, the neural activity at times t-dt were concatenated with the matrix for the neural activity at time t. If the original neural activity matrix was size nNeuron x T, this matrix for dt = 2 would be size 2*nNeuron x T. For dt = 3, it would be size 3*nNeuron x T, and so on.

4.4.9 Predicting turns using support vector machines

Calculating weights: The weights were found using the TFOCS software to solve the modified, sparse version of the SVM in Matlab. Because this often resulted in weights that were very small, but not truly zero, all weights that were less than 5% of the maximum weight for the lowest value of λ were set to zero.

Training/Validation: Due to the limited number of turns in each recording, it was not feasible to partition the data into separate training, validation, and testing sets. Instead, leave-one-out cross validation was used on the first 70% of turns in each recording. Subsamples of this portion of the recording were generated by taking all the data points of a single turn and randomly selecting an equal number of points in this portion where the worm was not turning. From this, we have n subsamples of the data. Weights were derived for n-1 of these subsamples, and validation was performed on the subsample that was left out. This was repeated so that each subsample was

used as a validation set. The average F_1 score across validation sets for each λ was found, and the value which was within one standard error of the maximum F_1 score was used in testing.

Testing: Testing was performed on the last 30% of the turns in each recording, and thus did not overlap with the validation and training set. Weights and parameters used were determined by the validation from the previous portion of the recording.

Probing time scales: Including prior neural activity in the prediction of turning behavior was done by generating the same time lag matrix as was used for lasso.

4.4.9 Comparing weights

The rank of a neuron for each behavior was determined by the absolute value of its weight for that behavior, so that even a negative weight could be considered top ranking. The percentage of overlap for each rank was calculated by finding the number of neurons that were both of that rank or higher for both behaviors, regardless of position within that rank. Predicting behavior was done as described previously for each method, but only providing the neural activity of the subsets of interest.

Chapter 5

Conclusion

5.1 Adding whole-brain imaging with cellular resolution to the *C. elegans* toolkit

The study of how neural activity drives behavior can be most straightforwardly addressed by recording all of the neural activity while an animal is behaving. I have presented a method for doing so in the nematode *C. elegans*, along with the analytical tools for tracking these neurons through time. We use a system comprised of two simultaneous imaging set ups, one for low magnification recording of behavior and one for high magnification recording of the calcium dynamics with single cell resolution. Because the animal is behaving, the head moves and bends, translations and deformations of the brain that make identifying and tracking each individual neuron difficult. To address this problem, we developed an algorithm that uses machine learning to automatically segment and track all of the neurons in the moving brain. These advances have made it possible to image the calcium activity of every neuron in the worms head while it freely explores an environment.

This set up not only enables whole-brain imaging in freely moving worms, it may also serve as a building block for further advances in the field. While it was designed to record from a single, exploring worm, appropriate adaptations are easily implemented to permit calcium

imaging of a worm engaging in other behaviors, such as mating or chemotaxis. Additional work could allow for the delivery of optogenetic stimuli concurrent with whole brain imaging during behavior, allowing us to inhibit or excite neurons while measuring the downstream effects, both in the neural activity and the resulting behavior. Advances in calcium indicators and voltage indicators can easily be incorporated into this imaging system.

While this imaging system and neuron tracking method have been a substantial addition to the *C. elegans* toolkit, we are not currently able to match the identities of the neurons we have recorded to the known neural identities in the worm atlas. This would allow us to compare how neural activity across worms drives behaviors, exploring whether the same neural architecture results in the same neural dynamics, or if there is variability in the ways in which the brain drives behavior. The use of multicolored fiducial references in the subsets of neurons provides a potential solution to this problem, but has yet to have been achieved.

5.2 Neural dynamics underlying behavior in *C. elegans*

Whole-brain imaging in freely moving worms has provided us with unprecedented datasets of both the neural activity and the behavior it is producing. Compared to immobilized worms, freely moving worms exhibit faster dynamics distributed across a greater number of neurons. This additional activity may be the result of a number of sources, such as proprioceptive feedback or coordination of multiple behaviors. While the worm is freely moving, it is not only coordinating going forward, backward, or turning, but also behaviors such as egg laying, defecating, and foraging. This additional neural activity may explain why we do not see an embedding of the command motor sequence in the global brain dynamics, as the neural activity is not as low dimensional as when a worm is in a microfluidic chip.

Although we do not see a clear indication of the motor command sequence in a low dimensional space derived by principal components analysis, the neural activity that drives such sequences is still present, as we are able to predict both locomotion and turning from the recorded neural activity. We see that these behaviors are encoded in largely distinct subsets, although locomotion neurons contain information about turning, while turning neurons do not carry information about locomotion. This may indicate that the default behavior is locomotion, and that when the worm is going to turn, this circuit is suppressed.

One of the primary challenges in predicting behavior from the neural activity was the limited amount of data for each individual worm, as recordings could only last roughly 8 minutes. This is due to the photobleaching of RFP, the fluorophore used to segment and track neurons. While adjusting the way in which we sampled data in the training set enabled the accurate prediction of behavior, longer recordings would allow for larger training sets. This would aid in preventing over-fitting, reduce the impact of outliers, and diminish the effects of noise in the data. From this, our predictions would be more accurate and better reflect the circuitry underlying the behavior. Such recordings may be possible as new fluorophores that are brighter and photobleach slower are developed.

Having limited data could also be solved by knowing the identities of the neurons recorded. By identifying neurons across worms, we would be able to pool the data and increase our predictive accuracy. Additionally, we would be able to directly compare the known, physical connectome to the functional connectome derived from our recordings. This would allow us to see how the functionally distinct circuits that underlie turning and locomotion are physically connected.

Bibliography

[1] C. D. Harvey, P. Coen, and D. W. Tank, “Choice-specific sequences in parietal cortex during a virtual-navigation decision task,” *Nature*, vol. 484, no. 7392, pp. 62–68, Mar. 2012.

[2] M. B. Ahrens *et al.*, “Brain-wide neuronal dynamics during motor adaptation in zebrafish,” *Nature*, May 2012.

[3] D. A. Butts *et al.*, “Temporal precision in the neural code and the timescales of natural vision,” *Nature*, vol. 449, no. 7158, pp. 92–95, Sep. 2007.

[4] B. B. Scott, C. M. Constantinople, A. Akrami, T. D. Hanks, C. D. Brody, and D. W. Tank, “Fronto-parietal Cortical Circuits Encode Accumulated Evidence with a Diversity of Timescales,” *Neuron*, vol. 95, no. 2, p. 385–398.e5, Jul. 2017.

[5] K. L. Briggman, “Optical Imaging of Neuronal Populations During Decision-Making,” *Science*, vol. 307, no. 5711, pp. 896–901, Feb. 2005.

[6] I. R. Popescu and W. N. Frost, “Highly dissimilar behaviors mediated by a multifunctional network in the marine mollusk Tritonia diomedea,” *J. Neurosci. Off. J. Soc. Neurosci.*, vol. 22, no. 5, pp. 1985–1993, Mar. 2002.

[7] J. G. White, E. Southgate, J. N. Thomson, and S. Brenner, “The Structure of the Nervous System of the Nematode Caenorhabditis elegans,” *Philos. Trans. R. Soc. B Biol. Sci.*, vol. 314, no. 1165, pp. 1–340, Nov. 1986.

[8] T. Schrödel, R. Prevedel, K. Aumayr, M. Zimmer, and A. Vaziri, “Brain-wide 3D imaging of neuronal activity in Caenorhabditis elegans with sculpted light,” *Nat. Methods*, vol. 10, no. 10, pp. 1013–1020, Sep. 2013.

[9] C. I. Bargmann, “Neurobiology of the Caenorhabditis elegans Genome,” *Science*, vol. 282, no. 5396, pp. 2028–2033, Dec. 1998.

[10] Y. Iino and K. Yoshida, “Parallel Use of Two Behavioral Mechanisms for Chemotaxis in Caenorhabditis elegans,” *J. Neurosci.*, vol. 29, no. 17, pp. 5370–5380, Apr. 2009.

[11] C. H. Rankin, C. D. O. Beck, and C. M. Chiba, “Caenorhabditis elegans: A new model system for the study of learning and memory,” *Behav. Brain Res.*, vol. 37, no. 1, pp. 89–92, Feb. 1990.

[12] I. Torayama, T. Ishihara, and I. Katsura, “Caenorhabditis elegans Integrates the Signals of Butanone and Food to Enhance Chemotaxis to Butanone,” *J. Neurosci.*, vol. 27, no. 4, pp. 741–750, Jan. 2007.

[13] G. J. Stephens, B. Johnson-Kerner, W. Bialek, and W. S. Ryu, “Dimensionality and Dynamics in the Behavior of C. elegans,” *PLoS Comput. Biol.*, vol. 4, no. 4, p. e1000028, Apr. 2008.

[14] C. Fang-Yen, C. V. Gabel, A. D. T. Samuel, C. I. Bargmann, and L. Avery, “Laser Microsurgery in Caenorhabditis elegans,” in *Methods in Cell Biology*, vol. 107, Elsevier, 2012, pp. 177–206.

[15] E. Yemini, T. Jucikas, L. J. Grundy, A. E. X. Brown, and W. R. Schafer, “A database of Caenorhabditis elegans behavioral phenotypes,” *Nat. Methods*, vol. 10, no. 9, pp. 877–879, Jul. 2013.

[16] G. Nagel, M. Brauner, J. F. Liewald, N. Adeishvili, E. Bamberg, and A. Gottschalk, “Light Activation of Channelrhodopsin-2 in Excitable Cells of Caenorhabditis elegans Triggers Rapid Behavioral Responses,” *Curr. Biol.*, vol. 15, no. 24, pp. 2279–2284, Dec. 2005.

[17] A. M. Leifer, C. Fang-Yen, M. Gershow, M. J. Alkema, and A. D. T. Samuel, “Optogenetic manipulation of neural activity in freely moving Caenorhabditis elegans,” *Nat. Methods*, vol. 8, no. 2, pp. 147–152, Feb. 2011.

[18] F. B. Shipley, C. M. Clark, M. J. Alkema, and A. M. Leifer, “Simultaneous optogenetic manipulation and calcium imaging in freely moving C. elegans,” *Front. Neural Circuits*, vol. 8, Mar. 2014.
[19] N. Chronis, M. Zimmer, and C. I. Bargmann, “Microfluidics for in vivo imaging of neuronal and behavioral activity in Caenorhabditis elegans,” *Nat. Methods*, vol. 4, no. 9, pp. 727–731, Sep. 2007.
[20] M. Chalfie, J. E. Sulston, J. G. White, E. Southgate, J. N. Thomson, and S. Brenner, “The neural circuit for touch sensitivity in Caenorhabditis elegans,” *J. Neurosci. Off. J. Soc. Neurosci.*, vol. 5, no. 4, pp. 956–964, Apr. 1985.
[21] Y. Zheng, P. J. Brockie, J. E. Mellem, D. M. Madsen, and A. V. Maricq, “Neuronal control of locomotion in C. elegans is modified by a dominant mutation in the GLR-1 ionotropic glutamate receptor,” *Neuron*, vol. 24, no. 2, pp. 347–361, Oct. 1999.
[22] A. V. Maricq, E. Peckol, M. Driscoll, and C. I. Bargmann, “Mechanosensory signalling in C. elegans mediated by the GLR-1 glutamate receptor,” *Nature*, vol. 378, no. 6552, pp. 78–81, Nov. 1995.
[23] J. M. Gray, J. J. Hill, and C. I. Bargmann, “A circuit for navigation in Caenorhabditis elegans,” *Proc. Natl. Acad. Sci.*, vol. 102, no. 9, pp. 3184–3191, Mar. 2005.
[24] S. Kato *et al.*, “Global Brain Dynamics Embed the Motor Command Sequence of Caenorhabditis elegans,” *Cell*, vol. 163, no. 3, pp. 656–669, Oct. 2015.
[25] A. Gordus, N. Pokala, S. Levy, S. W. Flavell, and C. I. Bargmann, “Feedback from Network States Generates Variability in a Probabilistic Olfactory Circuit,” *Cell*, vol. 161, no. 2, pp. 215–227, Apr. 2015.
[26] E. M. Maynard *et al.*, “Neuronal interactions improve cortical population coding of movement direction,” *J. Neurosci. Off. J. Soc. Neurosci.*, vol. 19, no. 18, pp. 8083–8093, Sep. 1999.
[27] M. A. Long, D. Z. Jin, and M. S. Fee, “Support for a synaptic chain model of neuronal sequence generation,” *Nature*, vol. 468, no. 7322, pp. 394–399, Nov. 2010.
[28] T.-W. Chen *et al.*, “Ultrasensitive fluorescent proteins for imaging neuronal activity,” *Nature*, vol. 499, no. 7458, pp. 295–300, Jul. 2013.
[29] A. C. Kwan, “What Can Population Calcium Imaging Tell Us About Neural Circuits?,” *J. Neurophysiol.*, vol. 100, no. 6, pp. 2977–2980, Oct. 2008.
[30] F. Kubo, B. Hablitzel, M. Dal Maschio, W. Driever, H. Baier, and A. B. Arrenberg, “Functional Architecture of an Optic Flow-Responsive Area that Drives Horizontal Eye Movements in Zebrafish,” *Neuron*, vol. 81, no. 6, pp. 1344–1359, Mar. 2014.
[31] D. A. Dombeck, A. N. Khabbaz, F. Collman, T. L. Adelman, and D. W. Tank, “Imaging Large-Scale Neural Activity with Cellular Resolution in Awake, Mobile Mice,” *Neuron*, vol. 56, no. 1, pp. 43–57, Oct. 2007.
[32] B. A. Flusberg *et al.*, “High-speed, miniaturized fluorescence microscopy in freely moving mice,” *Nat. Methods*, vol. 5, no. 11, pp. 935–938, Nov. 2008.
[33] R. Prevedel *et al.*, “Simultaneous whole-animal 3D imaging of neuronal activity using light-field microscopy,” *Nat. Methods*, May 2014.
[34] N. A. Croll, “Behavioural Analysis of Nematode Movement,” in *Advances in Parasitology*, vol. 13, Elsevier, 1975, pp. 71–122.
[35] C. J. Cronin, Z. Feng, and W. R. Schafer, “Automated Imaging of *C. elegans* Behavior,” in *C. elegans*, vol. 351, New Jersey: Humana Press, 2006, pp. 241–252.
[36] J. Ben Arous, Y. Tanizawa, I. Rabinowitch, D. Chatenay, and W. R. Schafer, “Automated imaging of neuronal activity in freely behaving Caenorhabditis elegans,” *J. Neurosci. Methods*, vol. 187, no. 2, pp. 229–234, Mar. 2010.
[37] S. Faumont *et al.*, “An Image-Free Opto-Mechanical System for Creating Virtual Environments and Imaging Neuronal Activity in Freely Moving Caenorhabditis elegans,” *PLoS ONE*, vol. 6, no. 9, p. e24666, Sep. 2011.

[38] D. Ramot, B. E. Johnson, T. L. Berry, L. Carnell, and M. B. Goodman, “The Parallel Worm Tracker: A Platform for Measuring Average Speed and Drug-Induced Paralysis in Nematodes,” *PLoS ONE*, vol. 3, no. 5, p. e2208, May 2008.
[39] N. A. Swierczek, A. C. Giles, C. H. Rankin, and R. A. Kerr, “High-throughput behavioral analysis in C. elegans,” *Nat. Methods*, vol. 8, no. 7, pp. 592–598, Jun. 2011.
[40] A. E. X. Brown, E. I. Yemini, L. J. Grundy, T. Jucikas, and W. R. Schafer, “A dictionary of behavioral motifs reveals clusters of genes affecting Caenorhabditis elegans locomotion,” *Proc. Natl. Acad. Sci.*, vol. 110, no. 2, pp. 791–796, Jan. 2013.
[41] S. Faumont, “The Awake Behaving Worm: Simultaneous Imaging of Neuronal Activity and Behavior in Intact Animals at Millimeter Scale,” *J. Neurophysiol.*, vol. 95, no. 3, pp. 1976–1981, Mar. 2006.
[42] B. J. Piggott, J. Liu, Z. Feng, S. A. Wescott, and X. Z. S. Xu, “The Neural Circuits and Synaptic Mechanisms Underlying Motor Initiation in C. elegans,” *Cell*, vol. 147, no. 4, pp. 922–933, Nov. 2011.
[43] T. Kawano, M. D. Po, S. Gao, G. Leung, W. S. Ryu, and M. Zhen, “An Imbalancing Act: Gap Junctions Reduce the Backward Motor Circuit Activity to Bias C. elegans for Forward Locomotion,” *Neuron*, vol. 72, no. 4, pp. 572–586, Nov. 2011.
[44] J. Larsch, D. Ventimiglia, C. I. Bargmann, and D. R. Albrecht, “High-throughput imaging of neuronal activity in Caenorhabditis elegans,” *Proc. Natl. Acad. Sci.*, vol. 110, no. 45, pp. E4266–E4273, Nov. 2013.
[45] J. L. Donnelly *et al.*, “Monoaminergic Orchestration of Motor Programs in a Complex C. elegans Behavior,” *PLoS Biol.*, vol. 11, no. 4, p. e1001529, Apr. 2013.
[46] D. A. Clark, D. Biron, P. Sengupta, and A. D. T. Samuel, “The AFD Sensory Neurons Encode Multiple Functions Underlying Thermotactic Behavior in Caenorhabditis elegans,” *J. Neurosci.*, vol. 26, no. 28, pp. 7444–7451, Jul. 2006.
[47] S. H. Chalasani *et al.*, “Dissecting a circuit for olfactory behaviour in Caenorhabditis elegans,” *Nature*, vol. 450, no. 7166, pp. 63–70, Nov. 2007.
[48] Z. Li, J. Liu, M. Zheng, and X. Z. S. Xu, “Encoding of Both Analog- and Digital-like Behavioral Outputs by One C. elegans Interneuron,” *Cell*, vol. 159, no. 4, pp. 751–765, Nov. 2014.
[49] M. Hendricks, H. Ha, N. Maffey, and Y. Zhang, “Compartmentalized calcium dynamics in a C. elegans interneuron encode head movement,” *Nature*, May 2012.
[50] D. H. Hall and R. L. Russell, “The posterior nervous system of the nematode Caenorhabditis elegans: serial reconstruction of identified neurons and complete pattern of synaptic interactions,” *J. Neurosci. Off. J. Soc. Neurosci.*, vol. 11, no. 1, pp. 1–22, Jan. 1991.
[51] J. K. Pirri, A. D. McPherson, J. L. Donnelly, M. M. Francis, and M. J. Alkema, “A Tyramine-Gated Chloride Channel Coordinates Distinct Motor Programs of a Caenorhabditis elegans Escape Response,” *Neuron*, vol. 62, no. 4, pp. 526–538, May 2009.
[52] B. -m. Song and L. Avery, “Serotonin Activates Overall Feeding by Activating Two Separate Neural Pathways in Caenorhabditis elegans,” *J. Neurosci.*, vol. 32, no. 6, pp. 1920–1931, Feb. 2012.
[53] J. H. Thomas, “Genetic analysis of defecation in Caenorhabditis elegans,” *Genetics*, vol. 124, no. 4, pp. 855–872, Apr. 1990.
[54] N. Ringstad and H. R. Horvitz, “FMRFamide neuropeptides and acetylcholine synergistically inhibit egg-laying by C. elegans,” *Nat. Neurosci.*, vol. 11, no. 10, pp. 1168–1176, Oct. 2008.
[55] G. J. Berman, D. M. Choi, W. Bialek, and J. W. Shaevitz, “Mapping the stereotyped behaviour of freely moving fruit flies,” *J. R. Soc. Interface*, vol. 11, no. 99, pp. 20140672–20140672, Oct. 2014.

[56] T. Thestrup *et al.*, “Optimized ratiometric calcium sensors for functional in vivo imaging of neurons and T lymphocytes,” *Nat. Methods*, vol. 11, no. 2, pp. 175–182, Jan. 2014.
[57] D. R. Hochbaum *et al.*, “All-optical electrophysiology in mammalian neurons using engineered microbial rhodopsins,” *Nat. Methods*, vol. 11, no. 8, pp. 825–833, Jun. 2014.
[58] L. Jin, Z. Han, J. Platisa, J. R. A. Wooltorton, L. B. Cohen, and V. A. Pieribone, “Single Action Potentials and Subthreshold Electrical Events Imaged in Neurons with a Fluorescent Protein Voltage Probe,” *Neuron*, vol. 75, no. 5, pp. 779–785, Sep. 2012.
[59] Y. Gong, J. Z. Li, and M. J. Schnitzer, “Enhanced Archaerhodopsin Fluorescent Protein Voltage Indicators,” *PLoS ONE*, vol. 8, no. 6, p. e66959, Jun. 2013.
[60] E. Kim, L. Sun, C. V. Gabel, and C. Fang-Yen, “Long-Term Imaging of Caenorhabditis elegans Using Nanoparticle-Mediated Immobilization,” *PLoS ONE*, vol. 8, no. 1, p. e53419, Jan. 2013.
[61] B. Jian and B. C. Vemuri, “Robust Point Set Registration Using Gaussian Mixture Models,” *IEEE Trans. Pattern Anal. Mach. Intell.*, vol. 33, no. 8, pp. 1633–1645, Aug. 2011.
[62] Y. Deng, P. Coen, M. Sun, and J. W. Shaevitz, “Efficient Multiple Object Tracking Using Mutually Repulsive Active Membranes,” *PLoS ONE*, vol. 8, no. 6, p. e65769, Jun. 2013.
[63] J. H. Chou, C. I. Bargmann, and P. Sengupta, “The Caenorhabditis elegans odr-2 gene encodes a novel Ly-6-related protein required for olfaction,” *Genetics*, vol. 157, no. 1, pp. 211–224, Jan. 2001.
[64] H. Chui and A. Rangarajan, “A new point matching algorithm for non-rigid registration,” *Comput. Vis. Image Underst.*, vol. 89, no. 2–3, pp. 114–141, Feb. 2003.
[65] A. Myronenko and Xubo Song, “Point Set Registration: Coherent Point Drift,” *IEEE Trans. Pattern Anal. Mach. Intell.*, vol. 32, no. 12, pp. 2262–2275, Dec. 2010.
[66] Y. Tsin and T. Kanade, “A Correlation-Based Approach to Robust Point Set Registration,” in *Computer Vision - ECCV 2004*, vol. 3023, T. Pajdla and J. Matas, Eds. Berlin, Heidelberg: Springer Berlin Heidelberg, 2004, pp. 558–569.
[67] S. Kato, Y. Xu, C. E. Cho, L. F. Abbott, and C. I. Bargmann, “Temporal responses of C. elegans chemosensory neurons are preserved in behavioral dynamics,” *Neuron*, vol. 81, no. 3, pp. 616–628, Feb. 2014.
[68] M. A. Picardo *et al.*, “Population-Level Representation of a Temporal Sequence Underlying Song Production in the Zebra Finch,” *Neuron*, vol. 90, no. 4, pp. 866–876, May 2016.
[69] J. P. Rickgauer, K. Deisseroth, and D. W. Tank, “Simultaneous cellular-resolution optical perturbation and imaging of place cell firing fields,” *Nat. Neurosci.*, vol. 17, no. 12, pp. 1816–1824, Dec. 2014.
[70] J. P. Nguyen *et al.*, “Whole-brain calcium imaging with cellular resolution in freely behaving *Caenorhabditis elegans*,” *Proc. Natl. Acad. Sci.*, vol. 113, no. 8, pp. E1074–E1081, Feb. 2016.
[71] V. Venkatachalam *et al.*, “Pan-neuronal imaging in roaming *Caenorhabditis elegans*,” *Proc. Natl. Acad. Sci.*, vol. 113, no. 8, pp. E1082–E1088, Feb. 2016.
[72] Z. Bao, J. I. Murray, T. Boyle, S. L. Ooi, M. J. Sandel, and R. H. Waterston, “Automated cell lineage tracing in Caenorhabditis elegans,” *Proc. Natl. Acad. Sci. U. S. A.*, vol. 103, no. 8, pp. 2707–2712, Feb. 2006.
[73] R. P. Christensen *et al.*, “Untwisting the Caenorhabditis elegans embryo,” *eLife*, vol. 4, Dec. 2015.
[74] E. A. Mukamel, A. Nimmerjahn, and M. J. Schnitzer, “Automated analysis of cellular signals from large-scale calcium imaging data,” *Neuron*, vol. 63, no. 6, pp. 747–760, Sep. 2009.
[75] G. Lin, U. Adiga, K. Olson, J. F. Guzowski, C. A. Barnes, and B. Roysam, “A hybrid 3D watershed algorithm incorporating gradient cues and object models for automatic segmentation of nuclei in confocal image stacks,” *Cytom. Part J. Int. Soc. Anal. Cytol.*, vol. 56, no. 1, pp. 23–36, Nov. 2003.

[76] Y. Toyoshima *et al.*, “Accurate Automatic Detection of Densely Distributed Cell Nuclei in 3D Space,” *PLoS Comput. Biol.*, vol. 12, no. 6, p. e1004970, Jun. 2016.
[77] Y. Tanimoto *et al.*, “Calcium dynamics regulating the timing of decision-making in *C. elegans*,” *eLife*, vol. 6, May 2017.
[78] J. P. Nguyen, A. N. Linder, G. S. Plummer, J. W. Shaevitz, and A. M. Leifer, “Automatically tracking neurons in a moving and deforming brain,” *PLOS Comput. Biol.*, vol. 13, no. 5, p. e1005517, May 2017.